Title
MINICHANNEL-TUBE SOLAR THERMAL COLLECTORS FOR LOW TO MEDIUM TEMPERATURE APPLICATIONS

Author
Duong, Van Thuc

Publication Date
2015

Peer reviewed|Thesis/dissertation

UNIVERSITY OF CALIFORNIA, MERCED

MINICHANNEL-TUBE SOLAR THERMAL COLLECTORS FOR LOW TO MEDIUM TEMPERATURE APPLICATIONS

by

Van T. Duong

A thesis submitted in partial satisfaction of the
requirements for the degree of
Master of Science

in

Mechanical Engineering

Committee in charge:
Dr. Roland Winston, Chair
Dr. Gerardo C. Diaz, Advisor
Dr. Yanbao Ma

The thesis of Van T. Duong is approved:

Roland Winston, Chair	Date
Gerardo C. Diaz, Advisor	Date
Yanbao Ma	Date

University of California, Merced

Dedicated to my parents, family, Al, my friends and colleagues for their endless support.

ACKNOWLEDGEMENTS

"Whenever you see a successful person you only see the public glories, never the private sacrifices to reach them." –Vaibhav Shah

I believe when one goes pain and struggles, it builds their strength. This strength leads not only to success but shows their passion and perseverance. All I have to say is graduate school was difficult. These past couple of years has been a stressful and emotional roller-coaster. It tested my will and self-belief. Keeping my self-confident and motivated was difficult. However, having the people who I know care about me and their endless support has helped me push through the finish line.

I would like to express my most sincere appreciation and gratitude to my advisor Dr. Gerardo C. Diaz, who has not only the attitude and the substance of a genius, but also the patience to teach and guide anyone who is willing to learn. He continually conveys an excitement in teaching and research, and encourages to always keep learning. I am deeply grateful to have Dr. Diaz as an advisor; without his guidance and persistent help, completing my master's degree would not have been possible.

I would also like to express my gratitude to my colleagues, Dr. Neeraj Sharma and Andres Munoz-Hernandez for their expertise and support; Dr. Sharma for his willingness not only to help me whenever I need assistance and advice in a subject matter, but also those who asks for help. Special admiration and thanks to Andres for his support alongside struggling through classwork together.

I am very thankful for my parents. They believed in the American Dream and they believed that we can have a better life here. They raised me the way I am today: to never stop dreaming. They taught me through perseverance and hard-work, dreams can come true. Knowing that they believe in me and trust keeps the confidence and persistence from burning out. Now I probably to buy them a house to repay them.

I would like to express my deepest appreciation to Al. A small encouragement everyday can go a long way. Thank you for helping me through tough and stress times, and being there for me and keeping my head up at my lowest points.

I am thankful for my best friends from home (Ana, Jennifer, Michelle and Yvette) and my brother, Vincent. I can count on them to be there and being a phone call away when I needed them the most.

In addition, I cannot forget the UC Merced staff that aided in fabricating these two projects: Ed Silva for his near perfection work in the machine shop, and

Justin McConnell and Bryan Spielman for their highest quality and precision welds when ever it is needed. Additionally, Kevin Rico for putting literally all the parts of both the minichannel solar collectors together. I would also like to thank the current and past undergraduate students that dedicated their time to this project: Keith Saechao, Paulo Jeremias, Azucena Robles, Adam Martin, and Jose Guadarrama.

Furthermore and importantly, I would like to thank the California Energy Commission (CEC) for providing funding and making this project possible (Contract #POEF01-M04), and a collaboration of UC Solar and ARENA [grant 1-USO project on Micro Urban Solar Integrated Concentrators (MUSIC)] for partially funding me.

Lastly, a shout-out to anyone I missed. It was not intended to leave you out but this would go on for pages. To the rest of my family and friends from Merced, UC Merced, UC Santa Barbara, Alcoa and CUHK–thank you for believing and supporting in me. It truly means a lot knowing there are people who care.

CURRICULUM VITAE

Education

M.S. in Mechanical Engineering, University of California, Merced, 2015
B.S. in Mechanical Engineering, University of California, Merced, 2012.

Experience

Graduate Student Researcher in Diaz Research Group, University of California, Merced, 2013 – 2015.

Teaching Assistant for ENGR135: Heat Transfer (Fall 2013); ME170: Engineering Capstone (Spring 2014); ENG057: Statics and Dynamics (Spring 2015), ENGR151: Strength of Materials (Summer 2015) University of California, Merced, 2013 – 2015.

Junior Drafter at Deep Ocean Engineering, Inc. in San Jose, CA, 2013.

Mechanical Engineering Intern at Alcoa, Inc. in Alcoa, Tennessee, 2012.

Undergraduate Researcher in Harmon Research Group, Universisty of California, Merced, 2011.

Publications

V. Duong and G. Diaz (2015): "Performance of an aluminum-based minichannel solar collector for water heating applications ". In *California Energy Commission 40th Anniversary, San Francisco, CA.* **Showcased technology selected by the CEC.**

V. Duong and G. Diaz (2014): "Prediction of two-phase frictional pressure drop in copper minichannel solar water heater ". In *Poster at: UC Solar Symposium, San Francisco, CA.*

A. Robles, V. Duong, A. J. Martin, J. L. Guadarrama and G. Diaz (2014): "Aluminum minichannel solar water heater performance under year-round weather conditions". *Solar Energy.* 110, 356-364.

V. Duong and G. Diaz (2014): "Performance of an aluminum-based minichannel solar collector for water applications". *Proceedings of ASES Solar 2014.*1-6, San Francisco, CA.

V. Duong and G. Diaz (2014): "Carbon dioxide as working fluid for medium and high-temperature concentrated solar thermal systems ". *AIMS Energy Journal.* 2(1), 99-115.

TABLE OF CONTENTS

LIST OF FIGURES

LIST OF TABLES

ABSTRACT

Novel minichannel-tube solar thermal collectors for low to medium temperature applications are introduced. Two types of minichannel solar thermal collectors are analyzed experimentally: aluminum minichannel solar collector for low temperature applications, and copper minichannel solar collector for low to medium temperature applications.

The aluminum minichannel solar collector has been tested for over a year alongside a conventional copper flat-plate solar collector of similar dimensions as the aluminum minichannel solar collector to compare the performance of both system. Experimental results shows the aluminum minichannel solar collector is more efficient in water heating due to the aluminum minichannel tube design. Analysis of the thermal resistances, thermal inertia and a simulation comparing the speed of response of both collectors indicate that the aluminum minichannel solar collector is capable of heating the working fluid quicker than the conventional copper flat-plate collector.

Preliminary data show that the copper minichannel solar collector is capable of reaching temperatures above 100 °C for low grade steam generation. Using a steam heat exchanger, steam can be generated with the copper minichannel solar collector with steam temperatures over 100 °C.

Mathematical models are developed to use as predictive tools to simulate performances of the aluminum and copper minichannel solar collectors under various operating conditions. The mathematical model for single-phase flow simulating the performance of an aluminum minichannel solar collector has good agreement with experimental data from the same type collector.

Multiple two-phase pressure drop and heat transfer coefficient correlations are validated and compared to experimental data from the literature in order to select the best one to represent the copper minichannel solar collector. The pressure drop and heat transfer coefficient correlations are selected from Muller-Steinhagen and Heck [1] and Odeh et al. [2], respectively. The pressure drop and heat transfer coefficient correlations are coupled to solve the two-phase flow heat transfer problem. Although the two-phase mathematical model cannot be validated with experimental data at this time, simulations comparing the performance of the copper minichannel operating under single-phase and two-phase flow are presented. Results show that efficiency decreases as the operating temperature of the collector increases. Even

with the higher heat transfer coefficient during two-phase flow, the efficiency operating at temperature of the order of 100 to 110 °C in two-phase conditions are lower than operation in single-phase flow at temperatures between 50 and 90 °C. However, the difference of efficiency during single-phase flow with inlet temperature of 90 °C and during two-phase flow with inlet temperature of 100 °C is less significant, ranging from 3% to 10 %.

Economic analysis is provided showing that the market for solar thermal technology in the United States is slow due to the decreasing prices of natural gas. Although there are incentives and rebates across the nation for solar thermal technology, these rebates and incentives are not widely informed. More contributions in both the government and business sectors are required in promoting awareness of solar thermal technology.

Market potential of the minichannel solar collectors are analyzed. Analysis shows that the aluminum minichannel solar collector can replace the existing low-temperature, conventional copper flat-plate solar collector due to the experimental data showing the aluminum minichannel solar collector being more effective than the copper flat-plate collector. In addition, prices for aluminum are significantly cheaper than copper. Depending on the costs of extrusion process of aluminum minichannel tubes, and the labor and manufacturing costs to fabricate aluminum minichannel solar collectors, the costs of aluminum minichannel solar collector per square meter can be lower than conventional solar thermal collectors.

Chapter 1

INTRODUCTION

In the United States, water heating accounts for a significant amount of energy consumption in the residential and non-residential sectors. According to *U.S. Energy Information Adminstration (EIA)*, water heating accounted for about 20% of an average household energy consumption in residential sectors in 2009 [3]. There are many different water heating systems available in the market that vary by configurations and energy source utilized. According to McGuire, most common water heating systems use natural gas and electricity [4], with approximately 53% of the households in the United States utilizing natural gas, about 40% electricity, and the remaining using other energy sources such as wood, oil, propane, or solar. In a technical report by Newport Partners, the highest energy cost comes from standard electrical resistance water storage tanks [5]. The other common water heating configurations have a lower operating costs but require fuels such as natural gas or propane.

The idea of using solar as an energy source to heat up water has been around since the 17th-century. One of the first solar water heaters was invented by Clarence M. Kemp, patented in 1891 calling it the Climax-Solar Water Heat, an "apparatus for utilizing the sun's rays for heating water" [6]. The attractiveness of solar thermal systems such as solar water heaters are due to the capability of generating low to medium temperature heat in a sustainable way requiring no to very little external power. With different types of collector configuration, there is a variety of applications ranging from space heating and cooling to pool heating. As efficiency continues to improve, solar thermal applications are increasing in popularity especially outside of the United States.

1.1 Current solar thermal technologies: flat-plate, evacuated tube

Solar collectors are defined as energy exchanger that convert solar energy to either thermal energy or electric energy. Applications that utilize solar collectors to convert solar energy to thermal energy of a working fluid are called solar thermal. In solar thermal applications, the solar irradiance is absorbed by the solar collector transferring heat to a working fluid, usually a type of oil, gas, water or air. The heated working fluid can be used immediately in domestic water heating or stored in a tank to be used later in the day or night [7].

The most popular configurations of solar thermal collectors available are usually classified into two categories: 1. concentrating collectors for applications requiring medium-temperatures, and 2. non-concentrating collectors for applications requiring low-temperatures. Concentrating collectors may or may not require tracking depending on the efficiency and duration needed for the application. They are generally designed with a concave reflecting surface to intercept and focus the solar irradiation to a smaller absorber area in order to achieve a higher heat flux and higher temperatures. Non-concentrating solar collectors, on the other hand, are generally flat and the solar irradiance is not obstructed to a focused absorber area.

Since the first solar water heater patented by C. M. Kemp, numerous solar collector designs have been proposed and developed. The most popular designs available in the market include flat-plate, evacuated tube, and units requiring a compound parabolic concentration [8–10]. Solar water heaters, in general, are known to be "passive", meaning external or input of power is not required to operate the system. If "active," the system requires an external source of electric energy to operate. There are two different characteristics of solar water heaters: (1) open-system where water for consumption flows directly through the collectors, or (2) closed-system where a working fluid flows through the collectors and exchanges energy with water by means of a heat exchanger, usually located in a water storage tank. A review of recent developments in solar water heating systems can be found in Shukla et al. [11].

One of most important issues that remains in research is the effectiveness of transferring the energy from the sun to the working fluid. Increase in efficiency of solar water heaters can potentially and substantially impact the consumption of natural gas in the residential and commercial sector. Currently in the residential sector and market, two configurations of solar water heaters that are most popular and installed are the flat-plate collectors and the evacuated-tube collectors.

As shown in Figure 1.1, in a flat-plate solar collector design, small pipes are evenly distributed and attached to a thin absorber plate, usually by ultrasonic welding. The pipes and the thin plate are commonly made out of copper. The thin plate is sprayed with a selective coating to increase absorption. Solar energy is absorbed at the plate and transferred by heat conduction to the pipe carrying the working fluid. The small thickness of the plate generates a high thermal resistance, lowering the potential to transfer heat efficiently. In general, only a small section of the pipe is in good contact with the thin plate through the weld. The flat-plate collector is enclosed in protective framing or box with a glass cover to reduce heat losses from the absorber plate, as well as, to protect the collector from dust, moisture and weathering. The bottom of the box and underneath where the collector is placed is also layered with insulation to retain as much energy as possible at the collector. Jafarkazemi and Ahmadifard have extensively studied the design of flat-plate solar collectors and concluded that the performance of this flat-plate collectors are highly

dependent on the design parameters [12].

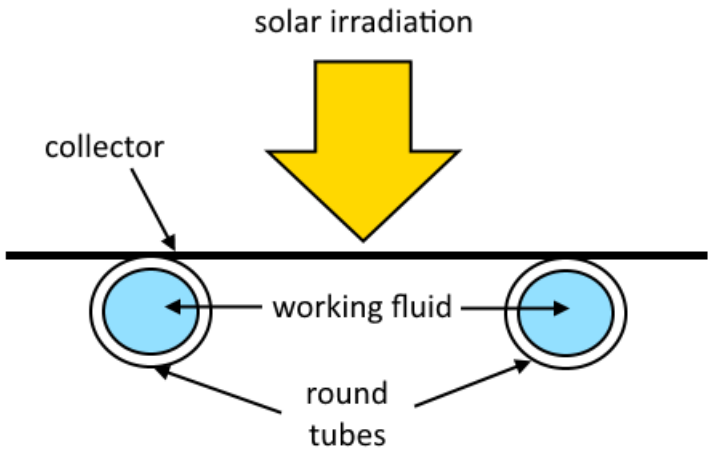

Figure 1.1: Heat transfer in a flat-plate solar collector.

Recent studies have been done to find alternatives to using metal absorbers due to the proneness to corrode. A goal of an absorber is to withstand any possible internal or external corrosion and to increase its longevity. To overcome this barrier, in Europe, new polymer flat-plate collectors have been proposed and introduced. The benefits of using polymer collectors are that they do not corrode, they have the ability to endure expansion especially in freezing conditions, they can directly use water instead of a low freezing point working fluids, and they lower material and manufacturing costs [11]. From a case study done by Liu et al., it was shown that the costs of a nylon polymer flat-plate collector was 20% less than a the cost of a copper flat-plate collector of a similar design [13]. However, some of the downfalls of a polymer-based flat-plate collector are the low thermal conductivity and its ability to only work at low temperatures.

The second popular solar thermal collector configuration is the evacuated-tube solar collector. Although evacuated-tube collectors are not as competitive in comparison with flat-plate collectors due to their higher costs, they can however operate at higher temperatures [11]. In the basic configuration shown in Figure 1.2, this figure demonstrates the incoming solar irradiation reflecting off the parabolic trough collector onto the absorber. The absorber is usually a selective coating layer that covers a copper heat pipe. The absorber is enclosed by a glass envelope and sealed in a vacuum to reduce heat losses. This configuration generally consists of a heat-pipe welded to an absorber fin. The working fluid is moved by thermosyphon phenomena and the energy that is absorbed by the heat-pipe is transferred to the condensing section to exchange heat from the working fluid to water inside a storage tank. One main issue in this particular design is the relative small condenser size.

The condenser size limits the rate of heat transfer to the water [14]. Another issue is maintaining the evacuated-tube to be vacuum sealed; over time the evacuated-tubes lose the vacuum causing higher heat loss by convective effects [15].

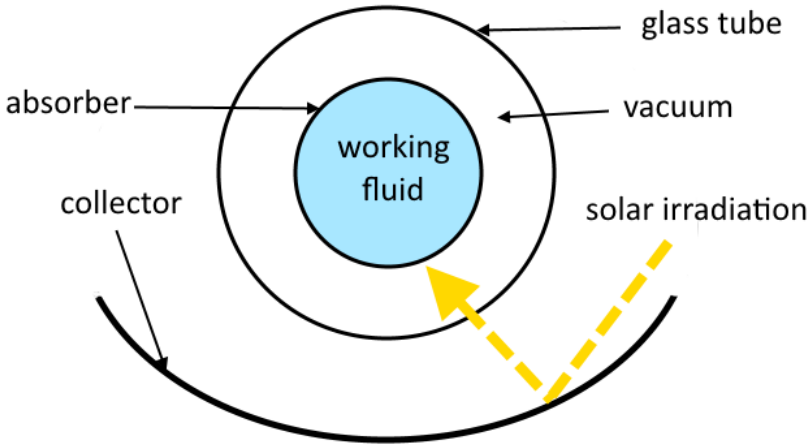

Figure 1.2: Heat transfer in a evacuated-tube with a parabolic trough collector.

Recent research has tried altering the evacuated-tube collector design to increase efficiency. Such designs studied different shapes of fins: finned attached to the absorber tube, U-tube shaped welded in the interior circular fin, U-tube shaped welded in the interior of a rectangular duct fin, and U-tube welded on a copper flat plate [16]. Others looked at different configurations such as the design by Shah and Furbo [17], who studied evacuated-tube collectors that feature a concentric double glass with vacuum in the inner gap. The interior glass tube acts as an absorber due to the application of a selective coating. The working fluid flows between the interior glass tube and another tube acting as a spacer to reduce the amount of fluid volume being heated. They found that this design can absorb solar irradiation from all directions [17]. For more information about recent developments in solar thermal technology, extensive and comprehensive summaries can be found in [7, 11, 18, 19]

1.2 Minichannel tube collectors: aluminum, copper

In 2008, Diaz proposed a design utilizing minichannel tubes in evacuated-tube solar collectors to improve the effectiveness of heat transfer to the working fluid [20,21]. Sharma and Diaz numerically analyzed the performance of a evacuated-tube solar collector with a U-shaped minichannel tube as the absorber. Their results showed an increased of thermal efficiency in the evacuated-tube minichannel collector compared to the experimental data from a conventional evacuated-tube solar collector [22]. Recently, Mansour tested a similar concept of using minichannels as a new configuration in solar thermal design. Mansour tested a 0.6 squared meter

copper minichannel flat-plate solar thermal collector as well as developed a mathematical model to study the performance [23]. His results showed that his proposed minichannel solar flat-plate collector had a lower overall heat loss and a heat removal factor, a convenient parameter to compare performance, of 16.1% higher in comparison with a conventional copper flat-plate solar collector.

Minichannel heat exchanger, also called microchannel heat exchangers, are well-known in the automotive, electronics cooling, and heating, ventilation and air-conditioning (HVAC) industry for their improved performance of heat transfer and cooling and admirable compact size compared to round-tube plate-fin heat exchangers [24–26]. In the solar thermal industry, minichannels are gradually being introduced. Companies such as Chengyi from China and Savo Solar from Finland are manufacturing solar water heaters using minichannel tubes in a flat-plate like array arrangement. There were no long-term performance data about minichannel solar water heaters until recently by Robles et al. [27].

An example schematic of a minichannel tube used as a solar absorber is shown in Figure 1.3. As seen in the figure, the solar irradiation hits the surface of the minichannel tube, which is usually sprayed with a selective coating, and the energy is transferred directly to the working fluid. The working fluid is flowing parallel to the channels and generally pushed through the collector and system with a external pump.

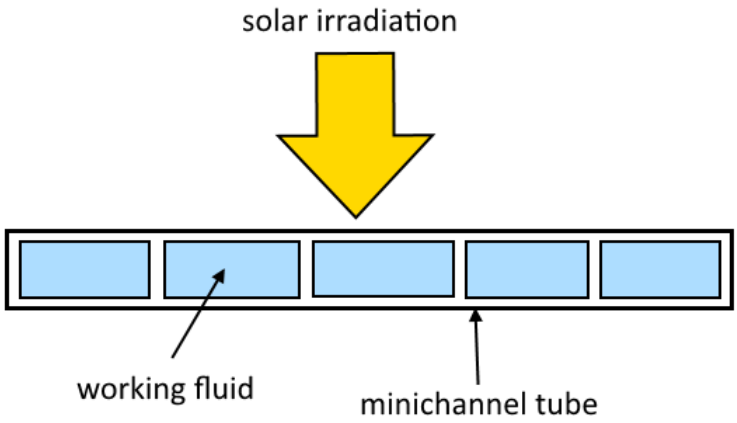

Figure 1.3: Heat transfer in minichannel tube solar collector.

Diaz Research Group at the University of California in Merced have recently built two minichannel collectors. Two materials of minichannel solar collectors have been investigated: aluminum and copper. Aluminum is used for low-temperatures, and copper is tested for operating at medium temperatures where steam generation can exist. The aluminum minichannel solar water heater has operated a little over

a year and produced good results when comparing to conventional flat-plate collectors. On the other hand, although less data were collected, the copper minichannel solar collector showed promising results such as steam generation in the collectors. This thesis is based on the research and studies of these two minichannel solar collectors. Details about the minichannel solar collectors, such as design, manufacturing, experimental results, single- and two-phase mathematical models developed tools, and economic and market analysis, will be presented in the following chapters.

1.3 Motivation and research objective

As many of Earth's natural resources are limited and finite, important resources such as oil and coal used for energy cannot be relied on indefinitely. However, solar thermal energy is renewable and clearly abundant. Thirugnanasambandam et al. [18] has shared the following calculations and facts to show the abundance and potential of harnessing solar energy: it has been studied that the Sun emits energy at a rate of 3.8×10^{23} kilowatts. Of that amount and noting that the distance between Sun and Earth is approximately 1.5×10^{8} kilometers apart, about 1.8×10^{14} kilowatts reaches Earth. However, only 60% of this energy reaches the Earth's surface, or 1.08×10^{14} kilowatts. The other 40% is reflected back and absorbed by the atmosphere. Considering a fraction of the solar energy absorbed by Earth, say 0.1% of the 1.08×10^{14} kilowatts, and a low efficiency of 10% when converting to usable energy like thermal or electric, just by using solar energy this can generate 3000 gigawatts or four times world's total generating capacity. In addition, Thirugnanasambandam has noted that the total amount of solar irradiation absorbed by the Earth's surface is more than 7500 times the world's total energy consumption annually of 450 EJ (exajoule, 450×10^{18}, or 450 quintillion joules) [18].

Sustainable and renewable technology is gradually growing in popularity and attractiveness. However, 80% of the energy consumed in the world still relies on fossil fuels. The consequences of relying on fossil fuels includes the fact that they are finite and limited. Consumption and burning of fossil fuels have evidently shown to decrease air quality, affecting living quality locally and globally, unfavorable weather conditions and climate change as greenhouse gas emissions are released into the atmosphere and environment. As oil and natural gas consumption and production are expected to increase in the next twenty years, international affairs and economics can be agitated causing conflicts when shortages of oil and gas becomes a reality [18].

As mentioned, solar thermal technology has been around since the 17th-century and through the years, different configurations have been tested to increase efficiency. Chow [19] mentions that the issues of commercialization and marketability of solar collectors are mainly the lack of public awareness and economic viability. Not having a product standardization, not offering warranties and performance certifications, and lack of experience and not creating new skill sets and proper training for installation also comes into play in hindering commercialization [19]. An ideal

solar thermal collector will have significant improvement in efficiency, as well as, cost-effectiveness in mass production and ability to be marketable. Extensive promotions and advertisements will be needed both in the commercial and government sector to raise public awareness.

The objective of the research is to study a novel solar collector configuration that potentially be more efficient and cost-effective than conventional solar water heaters. The research objective is to understand the heat transfer phenomena and performance of an aluminum-based minichannel solar water heater. The study will also perform a comparison with a conventional copper flat-plate solar water heater. Using the same design concept except utilizing copper minichannel tubes, steam generation two-phase flow and performance of a copper-based minichannel tube solar thermal collector is also examined.

1.4 Structure of the thesis

In this thesis, the design, experimental testing and numerical simulation of a non-evacuated aluminum- and copper-based minichannel-tube solar collectors will be fully described. Chapter 2: *Minichannel Solar Collector Designs* focuses on the design of the experiment of both the aluminum and copper minichannel solar collectors. A detailed description of the collectors is given, indicating the manufacturing process, as well as, the building and assembly process. In addition, how the minichannel solar water heating system works and operates is thoroughly explained. The components, such as the controls, data acquisition, water storage tank, and pump of the experimental design are fully described.

Chapter 3: *Single-Phase Flow Mathematical Model* and Chapter 4: *Two-Phase Flow Mathematical Model* deals with the mathematical formulations that were developed to simulate the minichannel solar collectors in order to predict its performance for different parameters. Chapter 3: *Single-Phase Flow Mathematical Models*, simulates the minichannel solar collectors operating in single phase, based on the mathematical model of the minichannel solar collector for the one-dimensional energy balance equations. The single-phase mathematical model is validated against the experimental results of the aluminum minichannel solar collector. Chapter 4: *Two-Phase Flow Mathematical Model*, focuses on developing a prediction tool to model the copper minichannel solar collector under two-phase and boiling conditions for steam generation. Correlations of heat transfer coefficient and pressure drop during two-phase flow are implemented to solve the coupled mathematical heat transfer problem. Different correlations of pressure drop and convection heat transfer coefficient are analyzed to determine the variability of results as a function of the correlation used. The correlations are validated against experimental data from the literature, and the best correlation for pressure drop and heat transfer coefficient are chosen to represent the copper minichannel solar collector during steam generation. Simulated performance results with the mathematical models

during two-phase versus single-phase flow in the copper minichannel solar collector are compared.

In Chapter 5: *Experimental Analysis*, experimental results are given for both, the aluminum and copper minichannel solar thermal collectors. The first section, 5.1: *Low temperature: aluminum minichannel and copper flat-plate solar water heaters*, displays the results of the aluminum minichannel under year-long and seasonal conditions. The performance of the aluminum minichannel channel solar collector is compared with copper flat-plate solar collector that replicates conventional and existing designs. Section 5.2 *Medium temperature: copper minichannel solar collector* presents the experimental results of the copper minichannel collector for the steam generation operating conditions. First modifications and adjustments to the copper minichannel solar collector are discussed in Section 5.2.1, and then analysis of performance of the copper minichannel solar collector are given in Section 5.2.2. Section 5.2.3: *Steam generation* discusses the steam generation produced through the steam heat exchanger attached to the outlet of the copper minichannel solar collector. Section 5.2.4: *Stagnation Temperatures and Thermosyphon Effects* examines the copper minichannel solar collector during stagnation, as well as, thermosyphon effects that occurs in the system.

Chapter 6: *Economic and Market Analysis*, describes the current outlook of solar thermal technology in the market in the United States and California. Section 6.1 considers the overlook of popularity and usage of solar thermal technologies. Data analyzed include annual of installations in residential and non-residential sectors. Impacts that are hindering installations and popularity are also discussed. Section 6.2.1 displays current approximated costs of conventional solar thermal systems in the residential and commercial sectors in California and the United States. Rebates and savings are introduced, and the benefits in certain states are discussed. Section 6.2.2, covers the breakdown costs of the aluminum minichannel solar collector prototype and compares to costs of conventional collectors. The last section of Chapter 6 provides an approximation of material costs and supplies needed for aluminum and copper minichannel collectors for mass production. These numbers are compared with the material costs for a conventional flat-plate collector.

Lastly, Chapter 7: *Conclusions and Future Work* summarizes the findings, results and analysis of these novel aluminum and copper minichannel solar collector designs, and provides some aspects and tasks that could not be accomplished during this thesis due to time constraints.

Chapter 2

MINICHANNEL SOLAR COLLECTOR DESIGNS

Minichannel heat exchangers, also known as microchannels heat exchangers, are commonly utilized in the automotive, air conditioning, and electronics cooling industry due to their improved performance and efficient compact size compared to round-tube plate-fin heat exchangers [24–26]. Although, minichannel heat exchangers are not common in the solar thermal industry, they are however gradually being introduced. There are a few companies that are currently manufacturing and supplying flat-solar collector designs utilizing minichannel tubes such as Chengyi from China and Savo Solar from Finland. However, studies of long-term performance and data of minichannel solar collectors are not widely available in literature. An aluminum minichannel solar water heater was designed, built and tested from June 2011 to June 2014 at the Castle facilities of University of California-Merced. Before discussing the results of the experiments and in order to understand how the experiments and testing were conducted with the minichannel solar water heaters, the following chapter is provided to describe the design, manufacturing and operation of an aluminum and a copper minichannel solar water heater prototypes. A brief description of the copper flat-plate collector used to compare performance with the aluminum minichannel solar collector is also presented.

2.1 Aluminum Minichannel Solar Collector Design

A typical solar collector is comprised of four components: (1) the absorber that captures the solar irradiation, (2) a metal frame to protect the absorber from the environment, weathering, and also reduce heat losses, (3) the working fluid where the absorber exchanges energy in form of heat, and (4) insulation to prevent heat loss from the absorber.

Most minichannel tube designs are produced through a metallurgy technique called extrusion. Extrusion is basically passing a metal at a high temperature and soften state through a die to create a shape of a choice with a fixed cross-section design. Aluminum minichannel tubes usually come in a rectangular shape with rounded edges and either with rectangular or circular ports inside. The ports are referred to the “channels”.

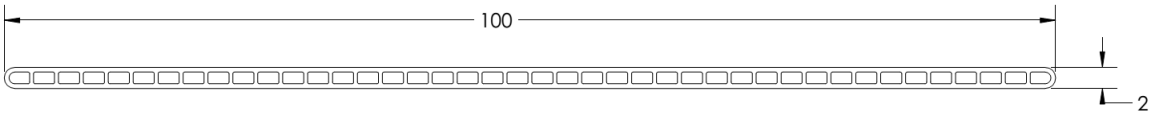

Figure 2.1: Example of a cross-section of an aluminum minichannel tube for a solar collector.

The minichannel tubes used to manufacture the aluminum minichannel solar absorber were produced by Hydro[1]. Hydro offered a readily available minichannel tube design which consisted of 100 mm × 2 mm MPE (multi-port extrusion) tube profile, as shown in Figure 2.1. In total, eleven aluminum minichannel tubes of 2.912 m in length were used for the absorber. The ends of each tube were inserted into the parallel slots of the headers and TIG welded to form the absorber. TIG welding, also known as tungsten inert gas welding, uses a tungsten electrode to produce the arc used for welding. TIG welding is usually utilized for small welds where precision and quality are needed. The headers were two Schedule 40 aluminum pipes of 1524 mm length with an internal diameter of 25.4 mm and eleven machined parallel slots. Each parallel slot were approximately 5 mm apart. Figure 2.2 shows a sketch of the overall minichannel solar absorber design with the tubes and headers.

The aluminum minichannel solar water heater prototype was built to analyze the performance and determine manufacturing techniques. The spacing between the minichannel tubes was not optimized for mass manufacturing. The spacing between the tubes was restricted by the size of the TIG welding nozzle used to join the tubes to the headers. A photo of the aluminum minichannel absorber before application of selective coating is shown in Figure 2.3.

After having the tubes TIG welded to the headers, Black Chrome (EC-Series) selective coating was applied to the absorber. The Black Chrome has a maximum absorptivity of 95% and emissivity of 12%. The novel minichannel design uses the tube as the actual absorber, eliminating the need for an absorber fin attached to the tubes. This gives a significant advantage because the working fluid is directly in contact with the tube walls that receive the solar irradiation. Thus, this effect reduces the overall thermal resistance as shown in Figures 1.1 and 1.3. In addition, plots of temperature distributions on the surface of the absorber of the flat-plate and minichannel absorbers are shown in Figure 2.4. The calculations of the temperature distribution in a round-tube flat-plate were obtained from *Chapter 6.3: Temperature Distributions in Flat-Plate Collectors* by Duffie et al. [8]. The calculations of the temperature distribution of the minichannel tube used the method of heat transfer from extended surfaces by Incropera et al. [28].

[1]http://www.hydro.com/

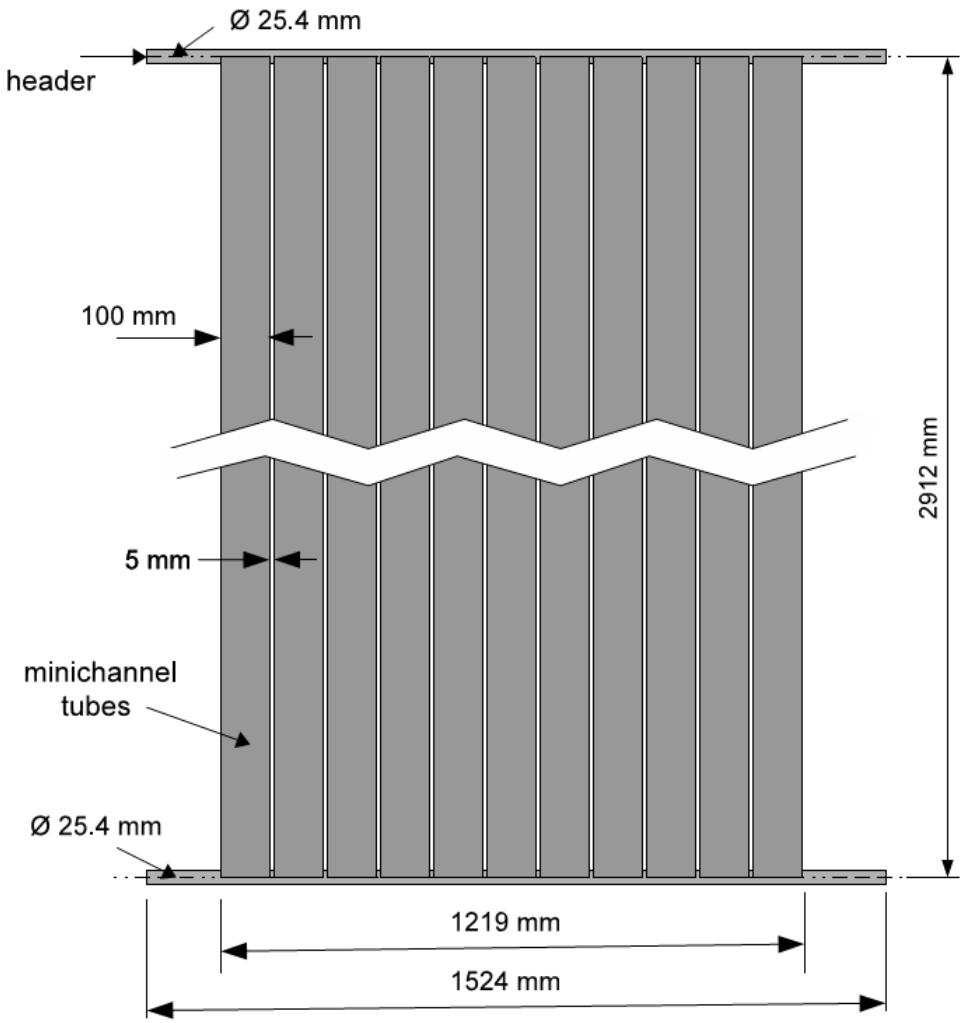

Figure 2.2: Dimensions of the aluminum-based minichannel tube solar collector.

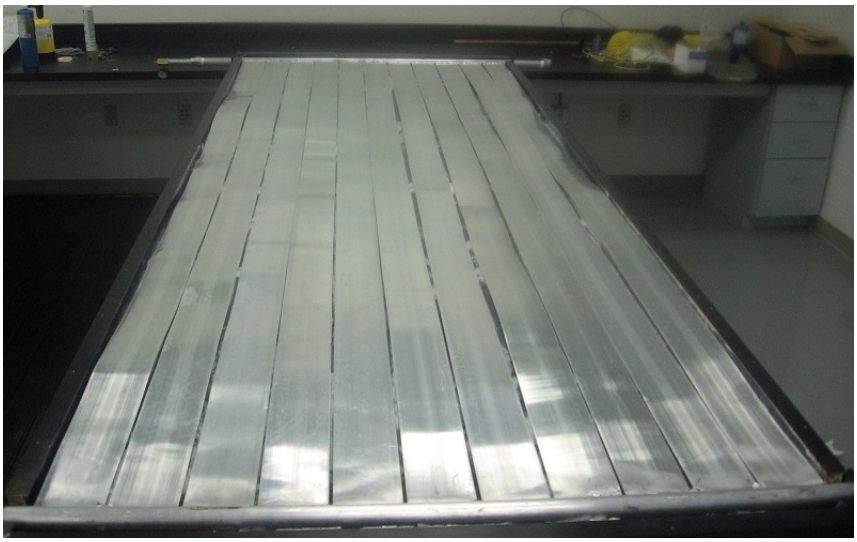

Figure 2.3: Minichannel tube solar water heater before application of selective coating.

Finally, after applying the selective coating, the aluminum minichannel absorber was placed inside a commercial metal frame. This metal frame was specifically made for conventional flat-plate collectors. The metal frame included insulation underneath the absorber which was a layer low-binder fiberglass on top of a layer of rigid foam underneath. The frame was covered with an extra clear patterned glass from Solite that has a transmissivity of 0.909. This kept the absorber clean from dust and weathering, and also reduced heat losses by convection from the absorber to the environment. The metal frame is approximately 1220 mm wide and 3050 mm long.

2.1.1 Copper Flat-Plate Collector

In order to compare the performance of the aluminum minichannel solar collector, a conventional copper flat-plate collector was built and tested alongside the aluminum minichannel collector. The copper flat-plate collector was built using similar manufacturing techniques as conventional and commercially available copper flat-plate collectors. Conventional flat-plate collectors generally have the round tubes welded to the copper plate-fin at one contact point, however, this limits the heat transfer to the working fluid due to their small contact point. The copper flat-plate collector built at our facility had the plate-fin wrapped around the tube slightly increasing the surface area of the absorber.

The copper flat-plate absorber consisted of a plate of thickness 0.2032 mm (0.008 inches) and ten round tubes of approximately 12.7 mm in diameter equally

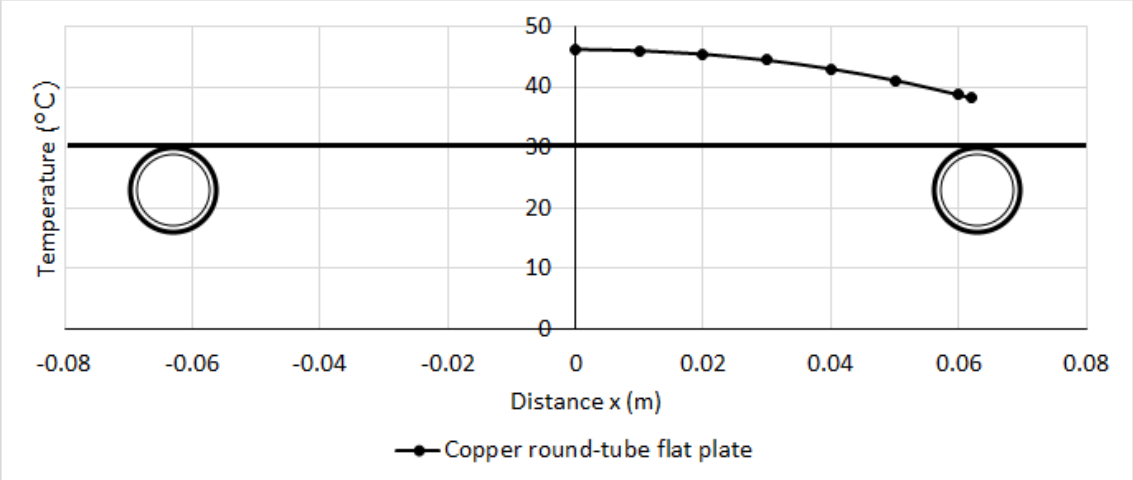

(a) Round-tube flat-plate

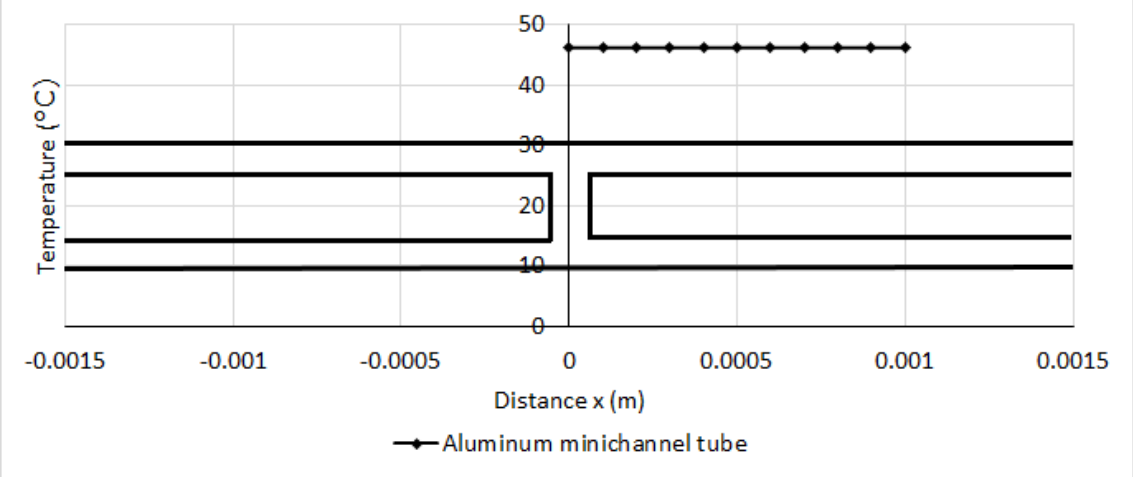

(b) Minichannel tube

Figure 2.4: Temperature distribution along the cross section of (a) round-tube flat-plate, and (b) minichannel tube absorber.

spaced and soldered underneath the copper flat-plate. The top surface of the flat-plate was also sprayed with Black Chrome selective coating. The collector was placed in an identical model and size metal frame with insulation underneath the absorber and covered with an extra clear patterned glass from Solite.

Although the size of the collectors was identical, there were slight differences between the aluminum minichannel and copper flat-plate solar collectors. The copper flat-plate collector had a higher absorber surface area of 3.68 m^2 versus 3.20 m^2 of the aluminum minichannel design due to the voids in between the minichannel tubes. The copper flat-plate collector also had a higher hydraulic diameter in each tube. In total, considering all the ports in one minichannel tube, each minichannel tube had a hydraulic diameter of 1.42 mm; on the other hand, the round copper tubes used in the flat-plate collector had a hydraulic diameter of 12.7 mm which is the diameter of the round tube itself. However, the copper flat-plate only had ten round tubes in comparison to the eleven minichannel tubes. The aluminum minichannel collector had a free flow area of 1015.5 mm^2 which included all the eleven minichannel tubes in the collector. The free flow area of the copper flat-plate was 1026.1 mm^2. A summary of parameters comparing both collectors is given in Table 2.1. The aluminum minichannel and copper flat-plate solar water heaters were both mounted side-by-side on the roof of Castle facilities at University of California-Merced in Atwater, California, and operated from February 2013 to May 2014.

Table 2.1: Dimension comparison of aluminum minichannel and flat-plate solar collectors.

	Aluminum Minichannel	Copper Flat-Plate
Dimensions of Collector		
Frame length	3048 mm	3048 mm
Frame width	1219 mm	1219 mm
Absorber area	3.20 m^2	3.68 m^2
Total free flow area	1015.5 mm^2	1026.1 mm^2
Dimensions of Tube		
Hydraulic diameter of each tube	1.42 mm	12.7 mm
Width (major)	100 mm	—
Height (minor)	2 mm	—
Length	2912 mm	2912 mm
Number of tubes	11	10

2.1.2 Aluminum Minichannel and Copper Flat-Plate Components and System Design

Since the copper flat-plate was designed to compare the performance of the aluminum minichannel solar water heater, their systems components were identical.

A schematic of the experimental design and set-up is shown in Figure 2.5. The main components of the solar water heating systems were the solar collector, water storage tank, pump, control logic and data acquisition system, and sensors. Both solar collectors were mounted on top of Castle facilities building at the University of California at Merced (+37°22'28.59", -120°34'38.10") with an angle of 18° with respect to the ground. The collectors were slightly inclined towards west and the flow of the working fluid was in the north and south direction.

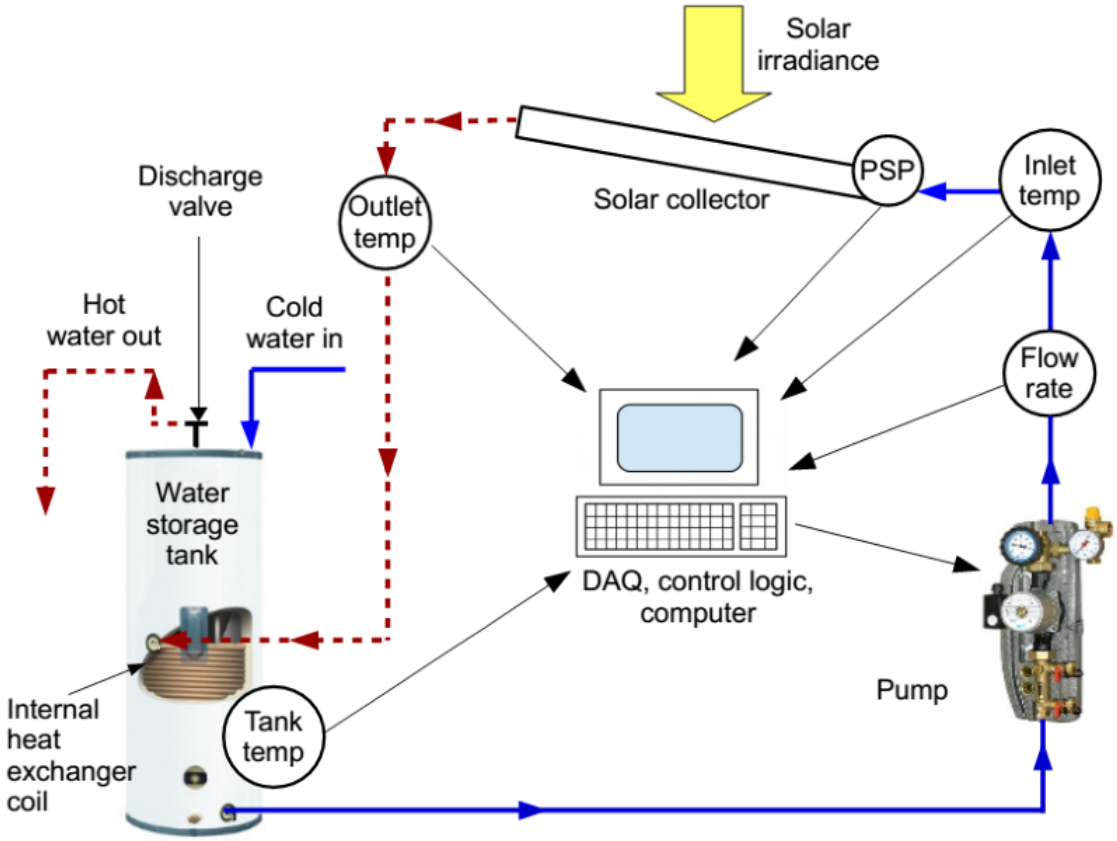

Figure 2.5: A schematic diagram of the aluminum minichannel and copper flat-plate solar water heater experimental set-up.

The aluminum minichannel and copper flat-plate solar water heaters consisted of a closed loop configuration that utilized a mixture of 50-50 propylene-glycol and water by volume as the working fluid. Although the thermophysical properties of the glycol-water mixture are less favorable than water itself, the advantage of this mixture is that the system can operate at below-freezing ambient temperatures. This helped reduced the chance of bursting tubes if ice formation were to occur inside the collectors. In each individual system, the solar collector absorbs the heat

and transfers the energy to the glycol-water mixture which is moving through the system by a pump. The heated working fluid enters the water storage tank and exchanges energy with the water stored inside the tank by means of an internal coil heat exchanger. The water storage tank is a standard commercial, 80-gallon (302.8 liters) water tank from SunEarth, Inc[2]. The working fluid exits the water storage tank and the 1/4 HP Grundfos pump recirculates the working fluid through the closed-loop system.

Sensors, such as thermocouples, flow meter and a solar irradiance sensor, were placed throughout the system and connected to a data acquisition system. Data was collected with a National Instruments (NI) CompactDAQ data acquisition hardware connected to LabView. Type K thermocouples by Omega with a range between -200 °C and 1250 °C with standard error of 1.1 °C over the entire scale were placed at the inlet and outlet of the collector and in the water storage tank. The volumetric flow rate circulating through the solar water heater system was measured using a Grundfos VFS 1-20 low-flow sensor. This flow sensor had an accuracy of ±1.5% of the full scale. The solar irradiance was measured using a Precision Spectral Pyranometer (PSP) from Eppley installed parallel to the collectors plane.

2.1.3 LabView and Control Logic

All measurements from the sensors such as the thermocouples, flow meters and the PSP were recorded using LabView by National Instruments. LabView is a measurement and control software that accompanies the NI CompactDAQ data acquisition hardware. LabView was programmed to record data from both the aluminum minichannel and copper flat-plate solar collectors every minute. Data that were logged were the collectors' inlet and outlet temperatures, storage tanks temperatures, temperatures at the flow meters, flow rates, and the solar irradiance. A screen shot of the custom programmed LabView interface is shown in Figure 2.6.

In Figure 2.6, a couple of manual switches, an indicator, and customizable features can be seen on the interface. The "Save" switch toggles automatic or manual data recording, and the "Saving" indicator shows when data is being saved. The two "Pumps" switches side-by-side allows the pumps to be controlled manually or automatically by the control logic. Also, the rate and number of samples that LabView logs data can be customized. When data are being logged, the data are tabulated in the table seen on the interface as well as recorded in a comma-separated values (CSV) file.

In addition to storing data, LabView was used to signal a programmed control logic. When LabView reads the PSP was greater than 150 W m^{-2}, it would signal the control logic to turn on the pump, activating the solar water heating system. Also, the control logic was programmed such that when LabView reads the temperature

[2]http://www.sunearthinc.com/

of 55 °C or above in the water in the storage tank, the discharge valve would open to drain the hot water as cooler water from the water supply would fill the storage tank. The discharge valve remained opened until LabView detected the water storage tank falling to 30 °C or below. This helped control the water storage tank temperature for safety purposes.

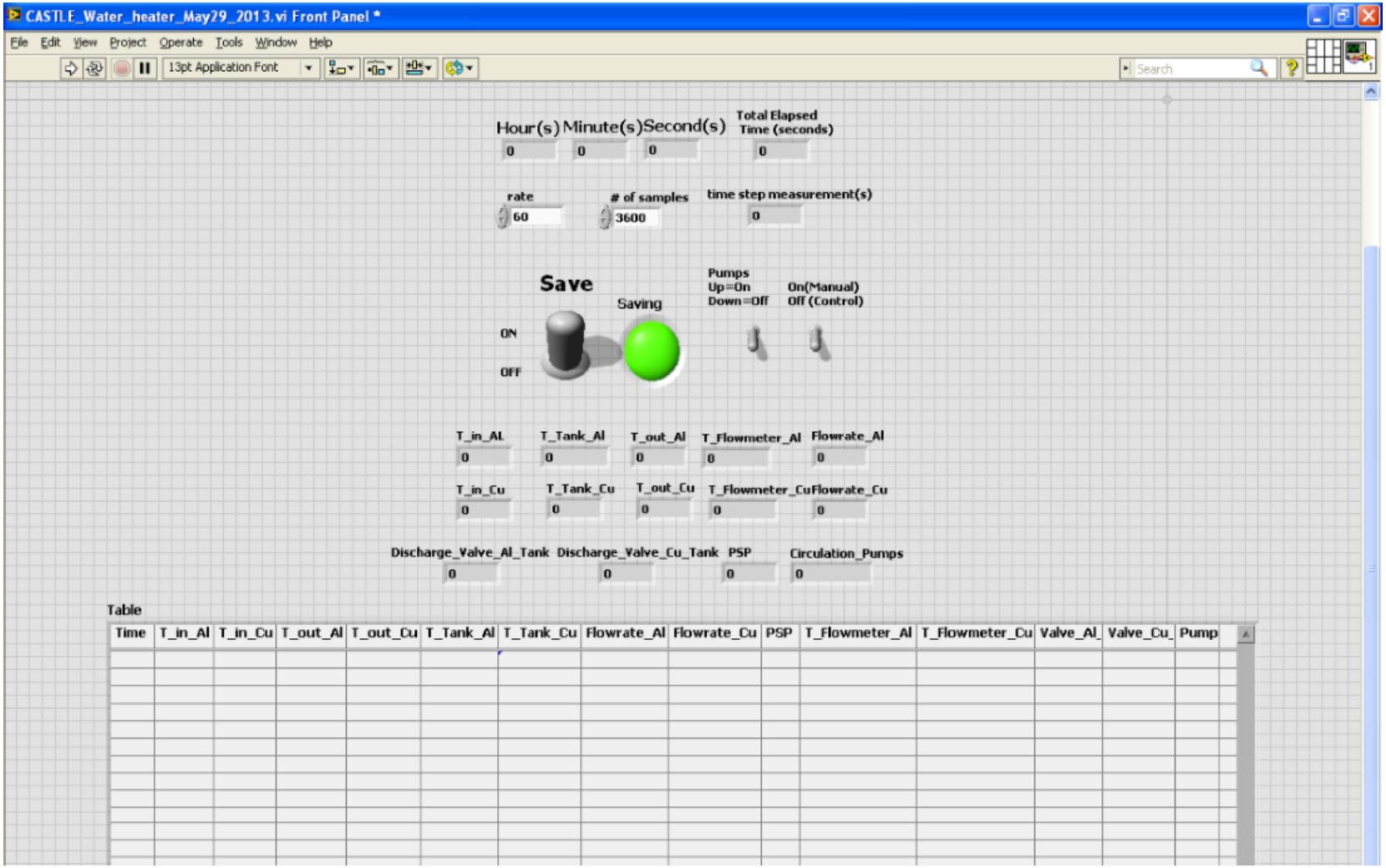

Figure 2.6: Screenshot of the LabView interface used to record data from the aluminum minichannel and copper flat-plate solar collectors.

2.2 Copper Minichanel Solar Collector Design

After gathering over a year worth of data with the aluminum minichannel solar water heater experiment, the second phase of the project was to produce a copper minichannel solar water heater that can operate at higher temperatures and have the ability to generate steam. The testing of the copper minichannel solar water heater is currently in progress since March 2015. The copper minichannel collector design is similar to the aluminum minichannel solar water heater. The main difference was related to the objective; the copper minichannel solar collector's goal is to operate at medium temperature and potentially generate steam. In addition, other differences relate to the size of the collector, the test stand, and size of the system components.

The copper minichannel tubes were designed and manufactured by Dr. Frank Kraft at Ohio University who has the patent invention of extruding copper micro-channels [29]. Extrusion of copper micro-channels is not common due to copper's material properties. It is difficult to extrude copper on account of the high working temperature required. Appendix A: *Copper minichannel tube manufacturing* summarizes the manufacturing process. With only one group in the United States able to extrude copper into minichannel tubes, the design of the copper minichannel tube had its limitations. The design of the copper minichannel tubes was constrained with respect to the width.

The first design took in consideration the size of the ports, free flow area and how they affect the pressure drop. The first design of the copper minichannel tube considered is shown in Figure 2.7. However, due to the restriction with respect to the width of the design, two other designs were suggested by Dr. Kraft. Design number two and three are shown in Figures 2.8 and 2.9, respectively. Design #2 had a smaller minor, or height of the minichannel tube, whereas design #3 essentially had the same minor as design #1 but smaller major (i.e width of the minichannel tube).

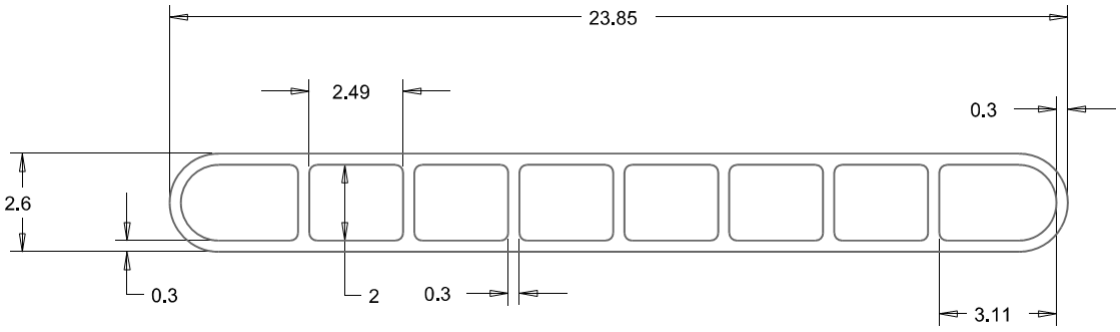

Figure 2.7: Copper minichannel tube design #1. Dimensions in millimeters.

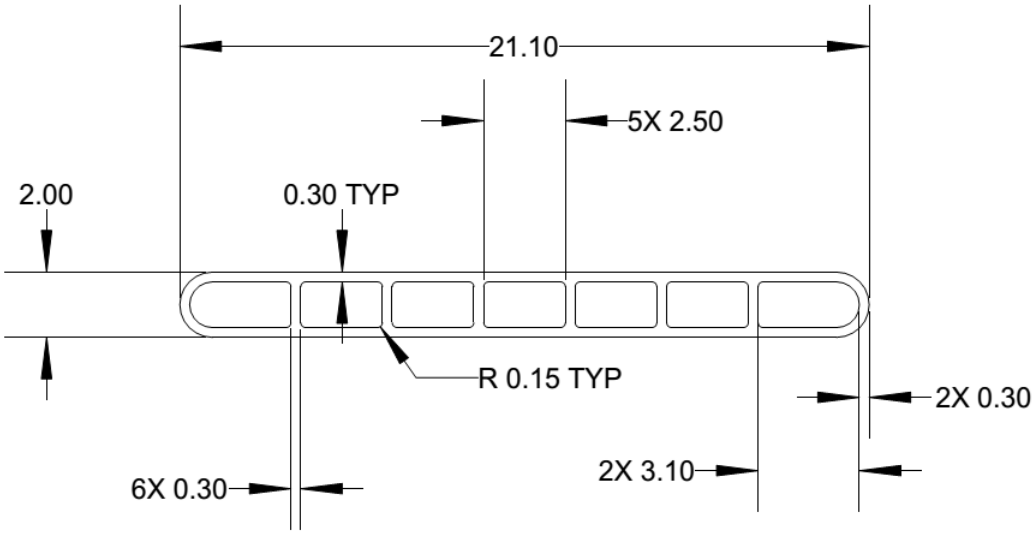

Figure 2.8: Copper minichannel tube design #2. Dimensions in millimeters.

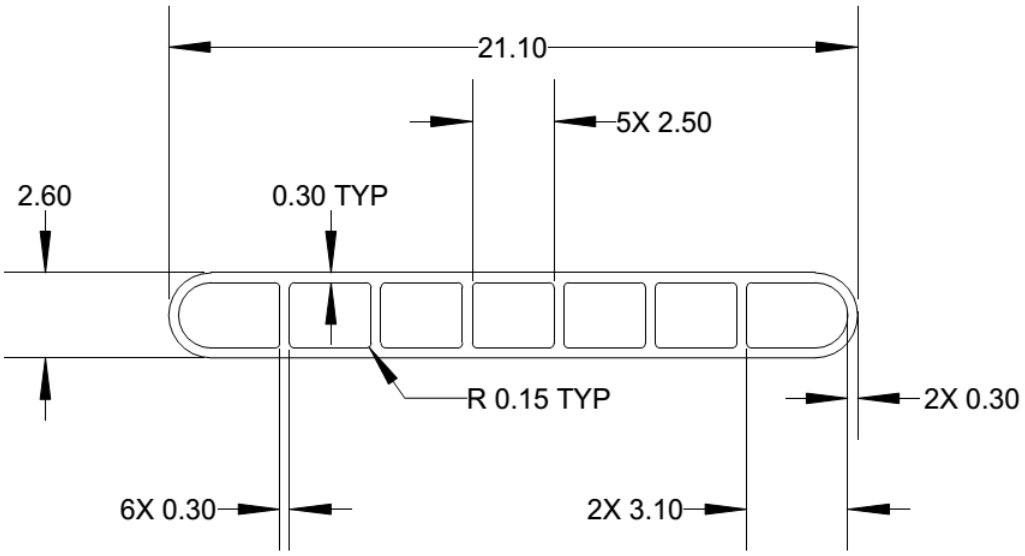

Figure 2.9: Copper minichannel tube design #3. Dimensions in millimeters.

Using the mathematical model described in Chapter 3 and creating a computational model in EES, the three designs were simulated to compare tube performance [30]. Comparisons narrowed down a final design used to fabricate the copper minichannel tubes to Design #3. Results used for comparison of tube performance are shown in Figures 2.10 to 2.12.

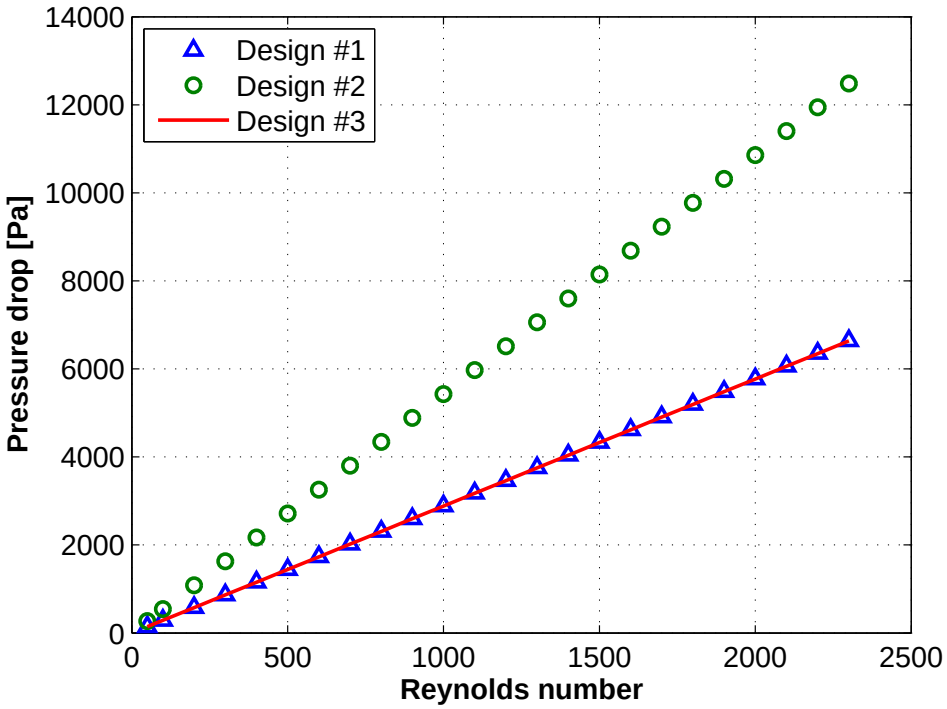

Figure 2.10: Pressure drop versus Reynolds number comparison of the three copper minichannel tube designs.

Figure 2.10 compares Reynolds number and pressure drop for the three copper minichannel tube designs. Reynolds number is a dimensionless way of looking at flow rate and it characterize whethers a flow is in laminar (Re $<$ 2100) or turbulent regime. Pressure drop was calculated by computing the difference between the inlet and outlet pressure of a minichannel tube. The formula used to calculate pressure drop of single-phase flow in a minichannel tube is given as

$$\Delta P = f \cdot \frac{L_{tube}}{D_h} \cdot \frac{\rho_{fluid} v_{mean}^2}{2} \tag{2.1}$$

where f is Darcy friction factor, L_{tube} is the length of the minichannel tube, ρ_{fluid} is the density of the working fluid, v_{mean} is the mean flow velocity of the working

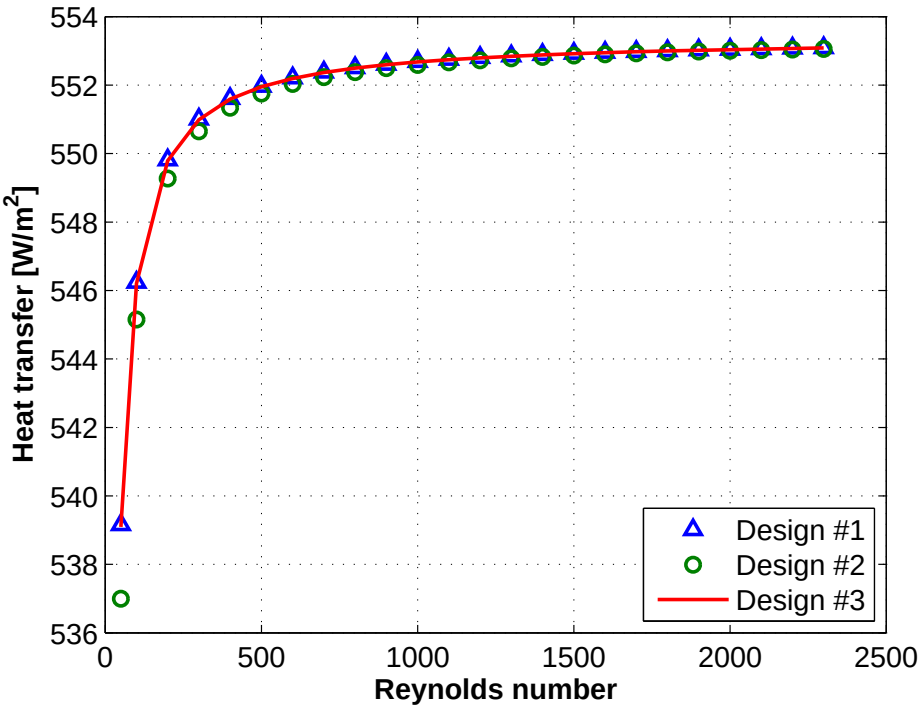

Figure 2.11: Heat transfer versus Reynolds number comparison of the three copper minichannel tube designs.

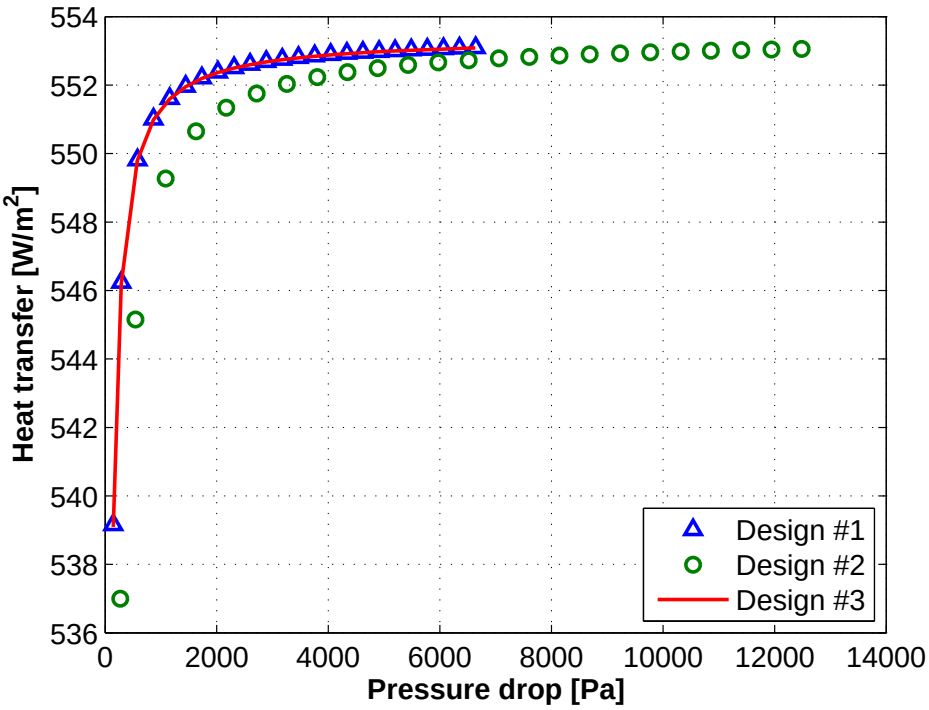

Figure 2.12: Heat transfer versus pressure drop comparison of the three copper minichannel tube designs.

fluid, and D_h is the hydraulic diameter of a minichannel tube. For laminar flow, Darcy friction factor is given as

$$f = \frac{64}{Re_{D_h}} \tag{2.2}$$

where Re_{D_h} is Reynolds number of the working fluid in the minichannel tube. Reynolds number is given by

$$Re_{D_h} = \frac{\dot{m} D_h}{A_{free} \mu_{fluid}} \tag{2.3}$$

where $\dot{m}$ is the mass flow rate of the working fluid, A_{free} is the free flow area of the minichannel tube, and μ_{fluid} is the dynamic viscosity of the working fluid. D_h is the hydraulic diameter of a minichannel tube given as

$$D_h = \frac{4 A_{free}}{P_w} \tag{2.4}$$

where P_w is the wetted perimeter of a minichannel tube. Lastly, v_{mean} is calculated by

$$v_{mean} = \frac{Re_{D_h} \mu_{fluid}}{\rho_{fluid} D_h} \tag{2.5}$$

where μ_{fluid} is the dynamic viscosity of the working fluid. A higher pressure drop indicates that more external power is needed to circulate the working fluid through the collectors. In Figure 2.10, Design #2 shows higher pressure drop compared to Designs #1 and #3 as Reynolds number is increased

Figure 2.11 compared heat transfer as a function of Reynolds number for the three designs. The heat transfer describes the rate that minichannel tubes, acting as an absorber, collect solar energy and transfer it to the working fluid. From the heat transfer versus Reynolds number plot, all three designs exhibits similar performance. Design #2 shows smaller heat rate in the lower range of Reynolds number compared to Designs #1 and #3.

Lastly, Figure 2.12 combines the previous two plots together. It can be seen that while Designs #1 and #3 show similar performance and higher heat transfer rates at the lower pressure drop range, Design #2 has lower heat transfer rate. Thus, Designs #1 and #3 would require less external power (i.e., pump) to achieve higher heat transfer rates compared to Design #2.

From these results and since Design #1 cannot be used due to the width restriction during the extrusion process, the final design chosen to construct the copper minichannel solar collector was Design #3. Twenty copper minichannel tubes were manufactured by Dr. Kraft and used in the minichannel solar collector. The copper minichannel tube was much smaller compared to the aluminum minichannel tubes. The custom made copper minichannel tubes were 21.10 mm by 2.60 mm

in major and minor, respectively, and 1819 mm in length. Table 2.2 shows an overview of the dimensions of the copper minichannel tube and copper minichannel solar collector.

Table 2.2: Dimensions of copper minichannel solar collector.

	Value	Unit
Dimensions of Collector		
Frame length	1935.5	mm
Frame width	1021.1	mm
Absorber area	.756	m^2
Total free flow area	731.7	mm^2
Dimensions of Tube		
Hydraulic diameter of each tube	2.2	mm
Width (major)	21.10	mm
Height (minor)	2.60	mm
Length	1819	mm
Number of tubes	20	–
Port width	2.50	mm
Port height	2.0	mm
Wall thicknesses	0.30	mm
Number of ports	7	–

The copper minichannel absorber was smaller in comparison to the aluminum minichannel absorber. Overall, the copper minichannel absorber was 1819 mm by 1322 mm including the headers, with 0.756 m^2 of absorber area or less than 25% the amount compared to the aluminum minichannel absorber. The headers were made of Type L one-inch copper tubing. Like the aluminum minichannel absorber, each headers were machined with slots 2 mm apart to fit the copper minichannel tubes at each ends. Instead of TIG welding, the copper minichannel tubes were torch brazed to the headers. Torch brazing joins two metals together by heating a filler metal above melting temperature and distributing it between the two metals by capillary action. Torch brazing allows two metals to join in extremely small areas especially when precision is needed. Precision was required for this project due to the fact that the walls of the copper minichannel tubes are so thin that they are easy to melt. In addition, the torched brazed joints can be operated at higher temperatures and pressure than ordinary soldering joints. Torch brazing may sound similar to soldering, however, the difference is the temperature of the heating process and the filler metal used. Soldering would use filler metals that require lower melting temperatures, whereas brazing would use filler metals that require higher melting temperatures. Figure 2.13 shows the overall dimensions of the copper minichannel tube solar absorber including the headers.

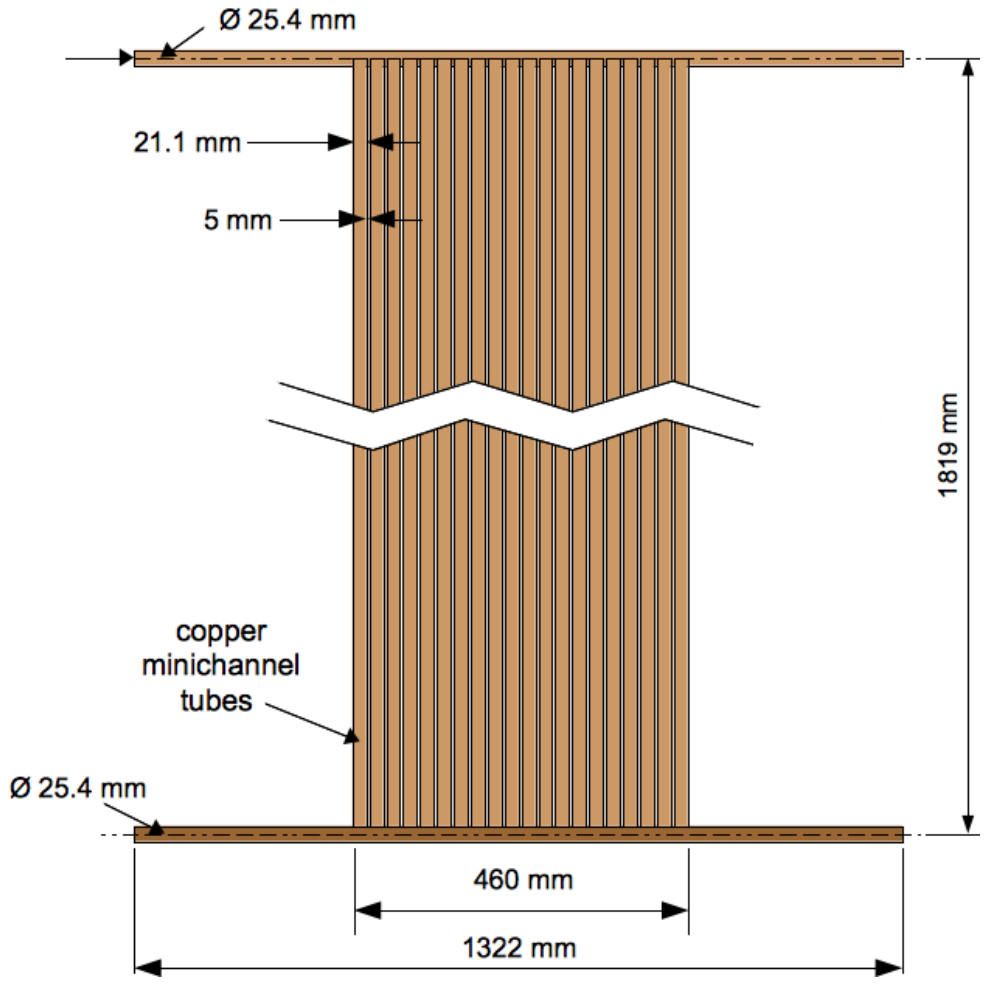

Figure 2.13: Dimensions of the copper-based minichannel tube solar collector.

After the copper minichannels were torched brazed to the headers to form a solar absorber, the absorber was cleaned and selective coating was applied. The selective coating used was the same type that was applied to the aluminum minichannel collector: Black Chrome selective coating tested maximum absorptivity of 95% and emissivity of 12%. Photos of the copper minichannel absorber before and after the selective coating are shown in Figure 2.14.

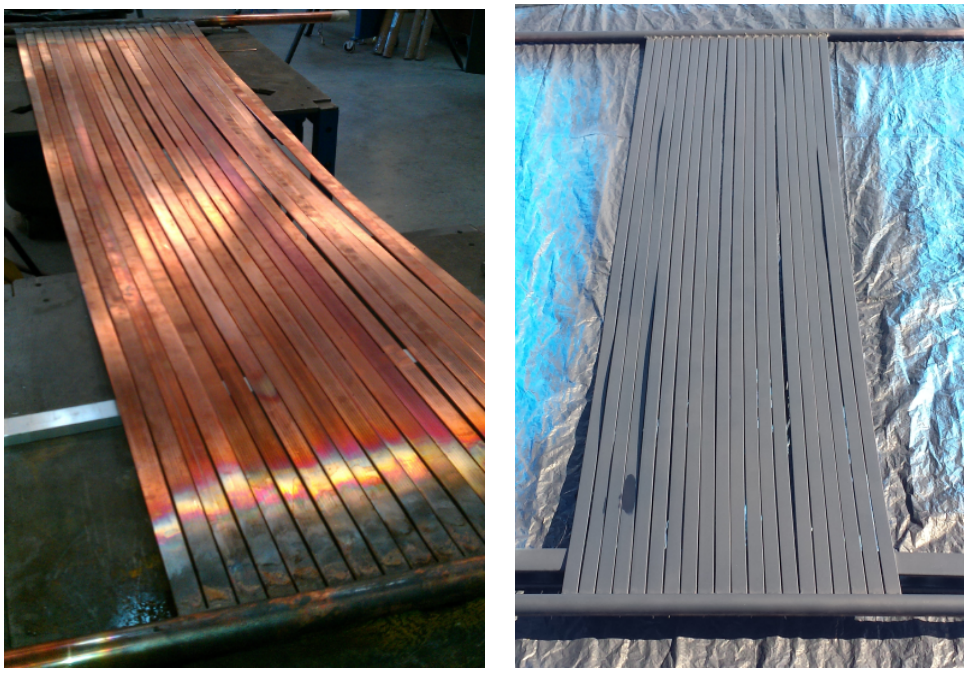

(a) (b)

Figure 2.14: Copper minichannel absorber (a) before selective coating, and (b) after selective coating.

Once the selective coating was applied and allowed to dry, the copper minichannel absorber was placed in a commercial metal frame. The frame dimensions were 1021.1 mm by 1935.5 mm and it was also covered with an extra clear patterned glass from Solite. A picture of the complete copper minichannel collector is shown in Figure 2.15 and dimensions of the overall collector are presented in Table 2.2.

One of the main differences between the copper minichannel and aluminum minichannel solar water heaters was the experimental procedure. The objectives of the copper minichannel solar collector were to handle higher temperatures in addition to generating steam. In order to gain more control of the experiment and the steam generation apparatus, the copper minichannel solar collector was placed on a portable test stand as opposed to the aluminum minichannel collector that was installed stationary on a roof. This allowed components of the copper minichannel

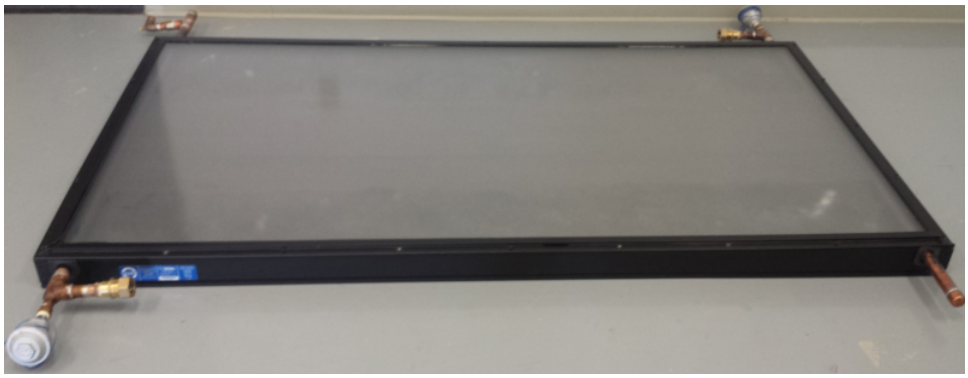

Figure 2.15: The copper minichannel absorber placed inside a commerical metal frame (1021.1 mm by 1935.5 mm) made for conventional solar flat-plate collectors.

solar collector to be accessible if changes or maintenance was needed. The steam generation apparatus, or steam generator for short, will be discussed in the following section.

The test stand was built using aluminum T-slotted framing by 80/20[3]. The framing is composed of basically structural aluminum bars with identical cross-sectional profile ("T-slotted") that allows easy fabrication, i.e., easy assembly. The decision to use T-slotted framing was due to its lightweight and straightforward assembly using fasteners and simple tools that make them easy to machine if needed, and it did not require any welding. The test stand was also designed and built to allow modification of the solar collector inclination, or tilt angle, and installed with appropriate wheels for portability. A photo of the test stand is shown in Figure 2.16. The copper minichannel solar water heater experimental unit is currently being tested in the Castle facilities at the University of California-Merced.

2.2.1 Copper Minichanel Solar Collector Components and System Design

The aluminum minichannel and copper flat-plate solar water heaters used identical components such as the collector metal frame, data acquisition system, water storage tank, sensors and pump. On the other hand, the system components for the copper minichannel solar collector were smaller due to the decreased size of the copper minichannel solar collector. There were also a few components that were added to the copper minichannel solar collector system such as the steam generator apparatus, a cooling tank and a few bypass valves. Table 2.3 shows some material and properties of the components used in the two minichannel solar water heating systems.

[3]http://www.8020.net/T-Slot-1.asp

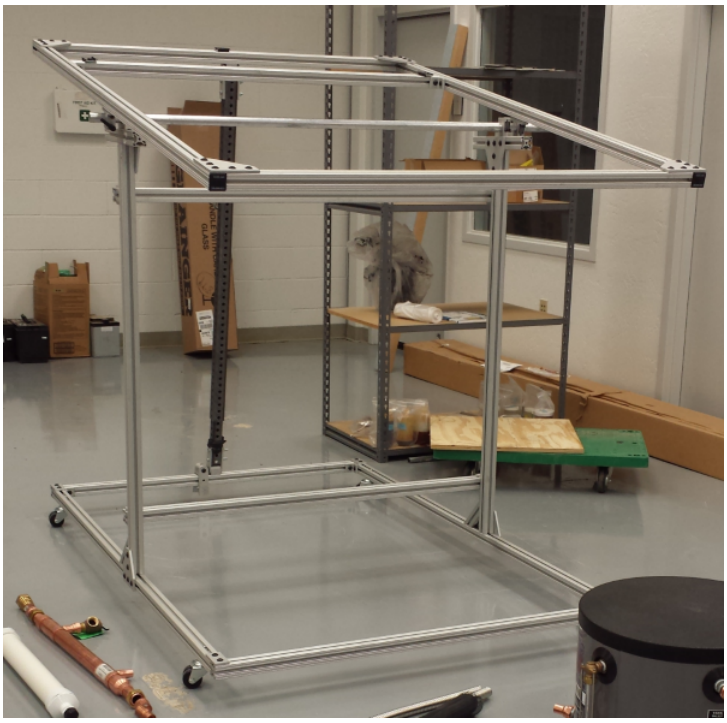

Figure 2.16: Portable test stand used for the copper minichannel solar collector.

Table 2.3: Property of the collector in both the copper and aluminum minichannel

Property	Value
Glass cover	
Material	Solite extra clear glass
Emissivity, ϵ_g	0.84
Reflectivity, ρ_g	0.08
Transmissivity, τ_g	0.909
Thermal conductivity, k_g	1.0 [$Wm^{-1}K^{-1}$]
Absorber selective coating	
Material	Black Chrome
Absorptivity, α_{abs}	0.95
Emissivity, ϵ_{abs}	0.12
Thermal conductivity, k_{abs}	11 [$Wm^{-1}K^{-1}$]
Aluminum Minichannel Tubes	
Thermal conductivity, k_{Al}	237 [$Wm^{-1}K^{-1}$]
Copper Flat-Plate/Minichannel Tubes	
Thermal conductivity, k_{Cu}	401 [$Wm^{-1}K^{-1}$]

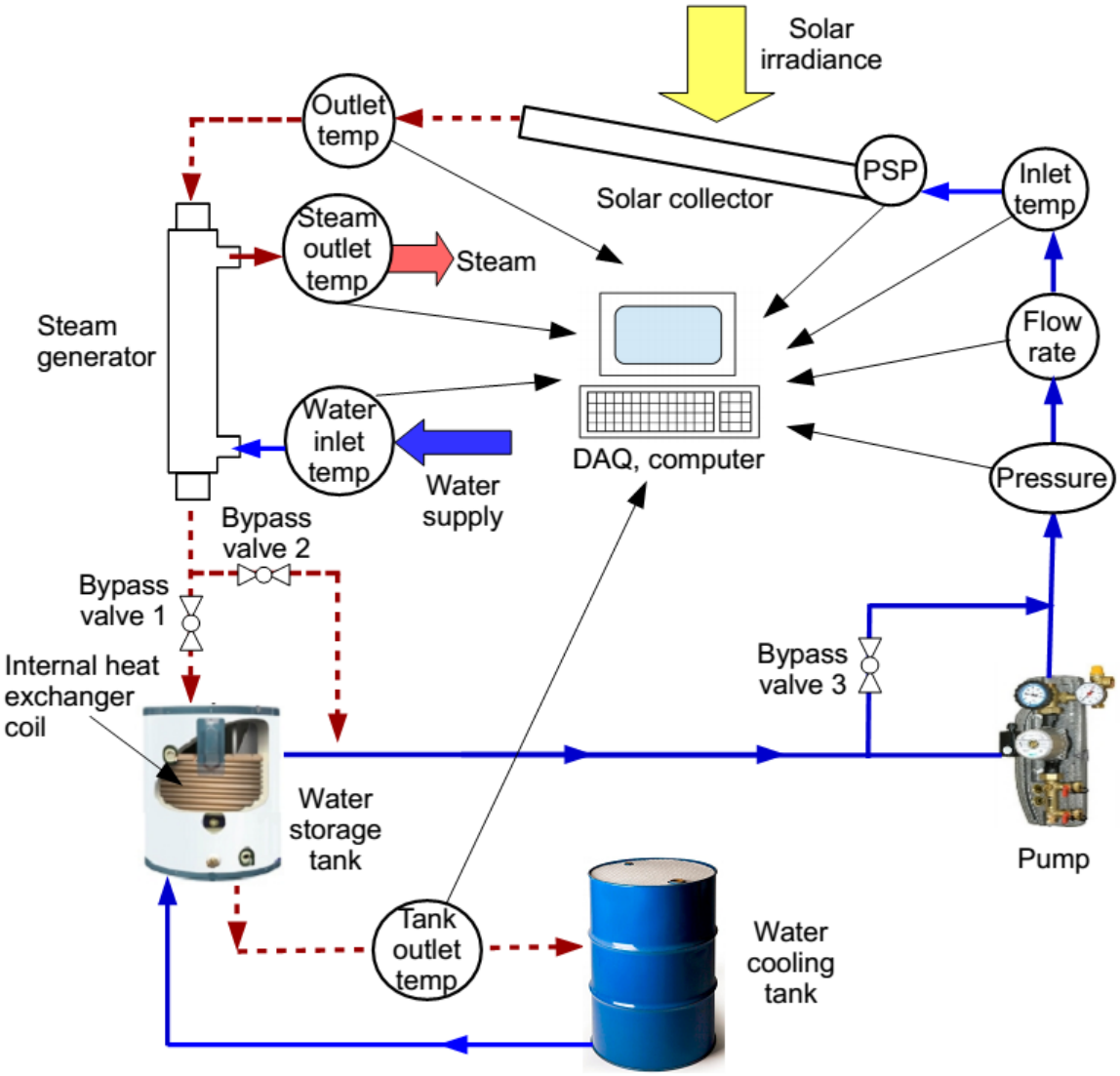

Figure 2.17: Copper minichannel-tube solar collector system diagram.

A diagram showing all the components in the copper minichannel solar collector system is shown in Figure 2.17. The copper minichannel solar collector has the following main components: solar collector, pump, water storage tank, steam generator apparatus, cooling tank, bypass valves and data acquisition system as seen in Figure 2.17. The following sensors were used: Type T thermocouples of range -200 °C to 350 °C (with standard error of 0.5 °C over the entire scale) manufactured by Omega to measure temperatures at the inlet, outlet of the collector, storage tank outlet, and steam inlet and outlet; TD1000 pressure sensor of range 0 to 100 PSI from Transducer Direct (with an accuracy of ±0.25% of the scale) to measure the pressure of the system; VFS 1-20 flow sensor from Grundfos of range 1.3 to 20 L/min (with an accuracy of ±1.5% of the full scale) to measure the volumetric flow rate of the working fluid cycled in the system; and an Eppley precision spectral pyranometer (PSP) to measure the solar irradiance. The sensors were all connected to a NI CompactDAQ data acquisition hardware. The DAQ hardware was connected to LabView to record and store data with samples taken between 15 seconds to one minute.

Water was used as the working fluid in the copper minichannel solar collector system, and it was passed through a portable water softener by WaterSticks[4]. The water softener assisted in filtering salts and minerals in the domestic water supply and helped prevent possible fouling especially inside the minichannel tubes that could clog passage ways. The working fluid circulates from the water storage tank to the solar collector by an externally powered 1/25 HP Grundfos pump. The working fluid absorbs the energy collected by the copper minichannel solar collector, and then it enters the steam generator. The steam generator is a simple counter-flow shell-and-tube heat exchanger where the working fluid is flowing through the internal tube while the fluid in the concentric ("shell") external tube is heated up to boiling conditions. The fluid in the external tube is also filtered by the water softener. As the working fluid in the internal tube exits the steam generator, it continues to circulate through the the water storage tank and through the whole system again. The water storage tank acts as a temperature control for the working fluid as well as a pressure control for the system. If the working fluid temperature increases above a certain limit, the cooling tank would supply cool water to reduce the temperature and pressure of the working fluid.

Lastly, three bypass valves were installed in the copper minichannel solar collector system. Bypass valves number one and two are located before the water storage tank. Bypass valve number one averted the working fluid from entering the water storage tank. This allowed the working fluid to avoid losing any heat from the internal heat exchanger coil that has a surface area of 10 ft^2 (0.92 m^2). Bypass valve number two altered the flow rate of the working fluid. Bypass valve number three is

[4]http://www.watersticks.com/

located near the pump. This bypass valve allowed the working fluid to divert from the pump, consequently also altering the flow rate of the system. All three bypass valves can be operated simultaneously or individually. Using bypass valves number two and three simultaneously can significantly increase or decrease the flow rate of the working fluid through the system.

Chapter 3

SINGLE-PHASE FLOW MATHEMATICAL MODEL

This chapter presents the mathematical formulation developed to predict the performance of aluminum and copper minichannel solar collectors operating at single-phase flow. The mathematical model is based on the one-dimensional energy balance equations. The single-phase mathematical model is compared and validated against the experimental results of the aluminum minichannnel solar collector.

3.1 Single Phase Flow

In single-phase, where the working fluid is considered to be a liquid at all times, the mathematical model is based on an energy balance of the minichannel solar thermal collector, developed as an adaption from the heat transfer analysis from Fonseca [31] and Duffie and Beckman [8]. The mathematical model includes the following assumptions: (1) steady-state conditions; (2) uniform surface temperature; and (3) all the ports in the minichannel tubes have the same dimensions.

3.1.1 Glass Cover

An energy balance is applied at the glass cover as seen in Figure 3.1. The energy balance includes the solar irradiance, radiation heat transfer exchange between the absorber and the glass, convection heat transfer between the absorber and the glass, and the losses due to the convection to the ambient air, radiation to the sky, and glass transmissivity:

$$q_{in} + q_{rad,air-g} + q_{conv,g-air} = q_{conv,g-sky} + q_{rad,g-sky} + q_{absorbed}$$

or writing out the heat fluxes in the respectiveful order,

$$\begin{aligned} G_s + \left(\frac{1}{\frac{1}{\epsilon_g} + \frac{1}{\epsilon_{abs}} - 1}\right) \sigma \left(T_{abs}^4 - T_g^4\right) + h_{air} \left(T_{air} - T_g\right) \\ = h_{g,air} \left(T_g - T_\infty\right) + \epsilon_g \sigma \left(T_g^4 - T_{sky}^4\right) + \left(\frac{\alpha_{abs} \tau_g}{1 - \left(1 - \alpha_{abs}\right) \rho_g}\right) G_s \end{aligned} \tag{3.1}$$

On the left-handside of Eq. 3.1, G_s is the total solar incident radiation, ϵ_g is the emissivity of the glass cover, ϵ_{abs} is the emissivity of the absorber, σ is Stefan-Boltzmann constant, T_{abs} is the temperature at the absorber, T_g is the temperature

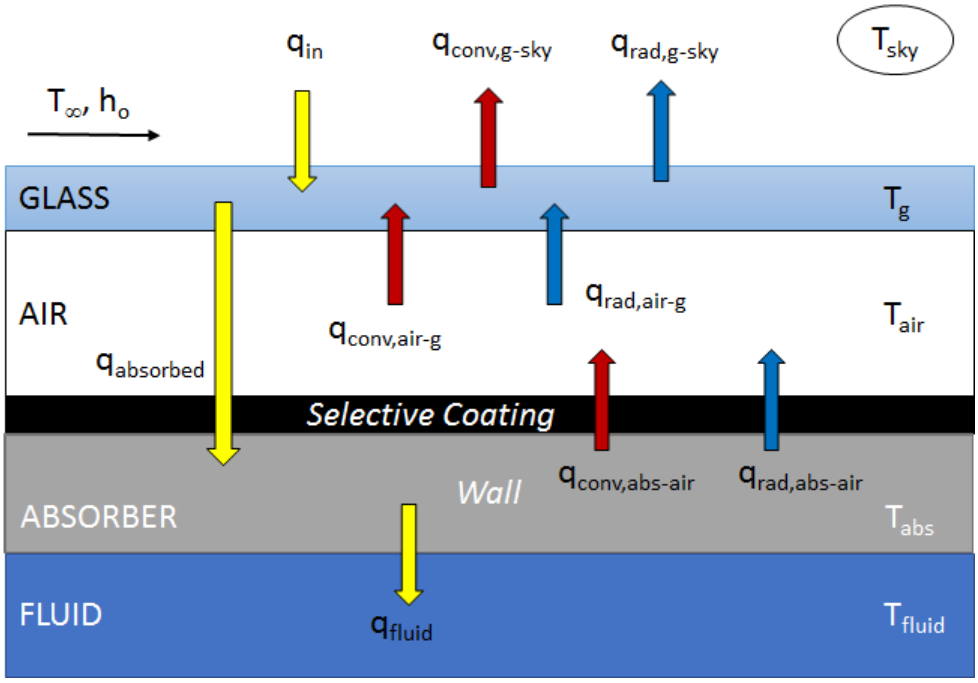

Figure 3.1: Energy balance of a minichannel tubes solar collector.

at the glass, h_{air} is the convection heat transfer coefficient of the air between the glass and absorber, and T_{air} is the temperature of the air between the glass and absorber. On the right-hand side, T_∞ is the temperature of the ambient air, α_{abs} is the absorption coefficient of the absorber, τ_g is the transmissivity of the glass, and ρ_g is the reflectivity of the glass. $h_{g,air}$ represents the convection heat transfer coefficient between the glass cover and the ambient air given as an empirical expression from Fonseca and Khoukhi and Maruyama [31, 32]:

$$h_{g,air} = 2.8 + 3v_{wind}$$

where v_{wind} is the velocity of the ambient air in (m/s). T_{sky} represents the sky temperature in relationship with the ambient temperature, T_∞, and is also an empircial equation given by Khoukhi and Maruyama [32]:

$$T_{sky} = 0.552T_\infty^{1.5}, \qquad \text{(K)}$$

3.1.2 Absorber-Cover Gap

For the gap between the absorber and glass cover, the Nusselt number due to natural convection is obtained by the following expressions given by Hollands et

al. [33]:

$$\begin{aligned}\mathrm{Nu} = 1 + 1.44\left[1 - \frac{1708\left(\sin 1.8\beta\right)^{1.6}}{\mathrm{Ra}\cos\beta}\right]\left[1 - \frac{1708}{\mathrm{Ra}\cos\beta}\right]^{+} \\ + \left[\left(\frac{\mathrm{Ra}\cos\beta}{5830}\right)^{1/3} - 1\right]^{+}\end{aligned} \tag{3.2}$$

where Ra is the Rayleigh number, β is the tilt angle of the collector, and the $+$ exponent means that the term in the brackets is used if the term is positive.

3.1.3 Absorber

An energy balance is also applied at the absorber where the incident radiation hitting the glass and the effect of the glass transmissivity is balanced by the losses of convection in the air gap between the absorber and the glass cover, the radiation between the absorber and glass cover, and conduction through the tube wall. The energy is then transferred to the working fluid:

$$q_{absorbed} = q_{conv,abs-air} + q_{rad,abs-g} + q_{fluid}$$

or with the heat fluxes defined respectively as,

$$\begin{aligned}\left(\frac{\alpha_{abs}\tau_g}{1-(1-\alpha_{abs})\,\rho_g}\right)G_s = h_{air}\left(T_{abs} - T_{air}\right) + \epsilon_{abs}\sigma\left(T_{abs}^4 - T_g^4\right) \\ + \left(\frac{T_{abs} - T_{fluid}}{R_{mc}L_{tube}a}\right)\end{aligned} \tag{3.3}$$

T_{fluid} is the temperature of the working fluid, L_{tube} is the length of the minichannel tubes, and a is the minichannel tube width. R_{mc} is the total resistance at the minichannel tubes between the absorber and the working fluid as shown in Figure 3.2. R_{mc} is also written out as,

$$\begin{aligned}R_{mc} &= R_{abs} + R_{wall} + R_{fluid} \\ &= \left(\frac{t_{abs}}{k_{abs}(L_{tube}a)}\right) + \left(\frac{t_{wall}}{k_{wall}(L_{tube}a)}\right) + \left(\frac{1}{\eta_o h_{fluid} A_{tube}}\right)\end{aligned} \tag{3.4}$$

where t_{abs} is the thickness of the absorber selective coating, k_{abs} is the thermal conductivity of the absorber selective coating, t_{wall} is the thickness of the minichannel tube wall, k_{wall} is the thermal conductivity of the material of minichannel tubes, and A_{tube} is the total surface area of one minichannel tube. t_{wall} and k_{wall} will depend on whether aluminum (t_{Al} and k_{Al}) or copper (t_{Cu} and k_{Cu}) minichannel tube collector is considered. h_{fluid} is the single-phase heat transfer coefficient of the working fluid and is given as,

$$h_{fluid} = \frac{k_l Nu_{UD}}{D_h} \tag{3.5}$$

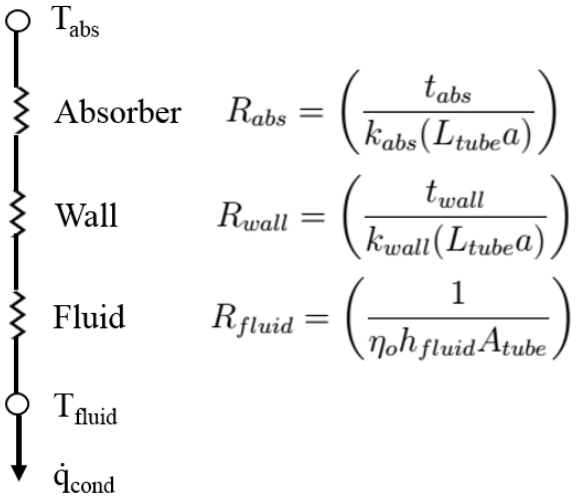

Figure 3.2: Resistances at the absorber.

where k_l is the thermal conductivity of the fluid, D_h is the hydraulic diameter and Nu_{UD} is the Nusselt number depending on the dimensions of the minichannel tube and based on Incropera et al. [28]. η_o is the overall fin efficiency and is calculated by,

$$\eta_o = 1 - \frac{N_{fin}A_{fin}}{A_{tube}}(1 - \eta_{fin}) \tag{3.6}$$

The efficiency of the fin, η_{fin} is described as

$$\eta_{fin} = \frac{\tanh(mL_{fin})}{mL_{fin}} \tag{3.7}$$

where $m = \sqrt{\frac{2h_{fluid}(t_{web}+L_{tube})}{k_{wall}t_{web}L_{tube}}}$, N_{fin} is the number of fins in one minichannel tube, A_{fin} is the surface area of one fin, L_{fin} is the fin length, and t_{web} is the web thickness.

3.1.4 Working Fluid

The heat flux transferred to the working fluid can be expressed by

$$q_{fluid} = \frac{\dot{m}C_p\Delta T}{L_{tube}W_{major}} \tag{3.8}$$

where $\dot{m}$ is the mass flow rate of the working fluid, C_p is the specific heat of the working fluid, ΔT is the difference of the outlet and inlet temperature $\Delta T = T_{out} - T_{in}$, and W_{major} is the major or width of one minichannel tube.

3.1.5 Model Validation

By using Engineering Equation Solver (EES), the mathematical model was solved using the Newton-Raphson iterative scheme to solve the system of nonlinear equations [30]. The mathematical model allowed us to simulate the performance of the minichannel solar collector for aluminum and copper configurations. For model validations, the experimental data was compared to the results obtained with the experimental set-up. Five input variables are required to run the simulations that were taken directly from the experimental data: inlet temperature T_{in}, solar irradiance G_s, volumetric flow rate $\dot{V}$, ambient temperature T_∞, and ambient air velocity v. Figure 3.3 shows the model validation comparing the thermal efficiency between the experimental test data and numerical mathematical model of the aluminum minichannel solar collector for Spring operating conditions. The efficiency is plotted against a common parameter used in solar energy research, $(T_{inlet} - T_\infty)/G_s$. Figure 3.3 shows good agreement is obtained between the experiment data and simulation results.

Figure 3.4 shows the same Spring operating conditions for model validation except the efficiency is plotted against the time of day. The mathematical model is steady-state and this can be seen in the figure. The mathematical model does not capture the transient and thermal inertia effects seen at the beginning and at the end of the day.

The model can be used to analyze the effect the material used for the minichannel tubes, for example, aluminum or copper. When aluminum properties were used for the minichannel tube, results of the model show that the last term of Equation 3.4 *(repoduced below)* which represents the overall thermal resistance to the working fluid is two orders of magnitude larger than the other two thermal resistances in that equation:

$$\begin{aligned} R_{mc} &= R_{abs} + R_{wall} + R_{fluid} \\ &= \left(\frac{t_{abs}}{k_{abs}(L_{tube}a)}\right) + \left(\frac{t_{wall}}{k_{wall}(L_{tube}a)}\right) + \left(\frac{1}{\eta_o h_{fluid} A_{tube}}\right) \end{aligned} \tag{3.4}$$

Furthermore, the resistance due to convection does not depend on the minichannel tube material. Therefore if operating within the typical temperature range of solar water heaters, there is no major loss of performance when using aluminum as the material for the minichannel tube instead of copper. In addition, the lower cost of aluminum in comparison to copper makes aluminum minichannel solar water heater an attractive alternative to the more conventional copper flat-plate solar water heater designs. More information about cost analysis of the aluminum minichannnel is discussed in Chapter 6. Due to the loss of mechanical properties when aluminum is exposed to higher temperatures, copper or other materials is recommended as mininichannel tube material for solar collector designs operating at a medium to high temperatures.

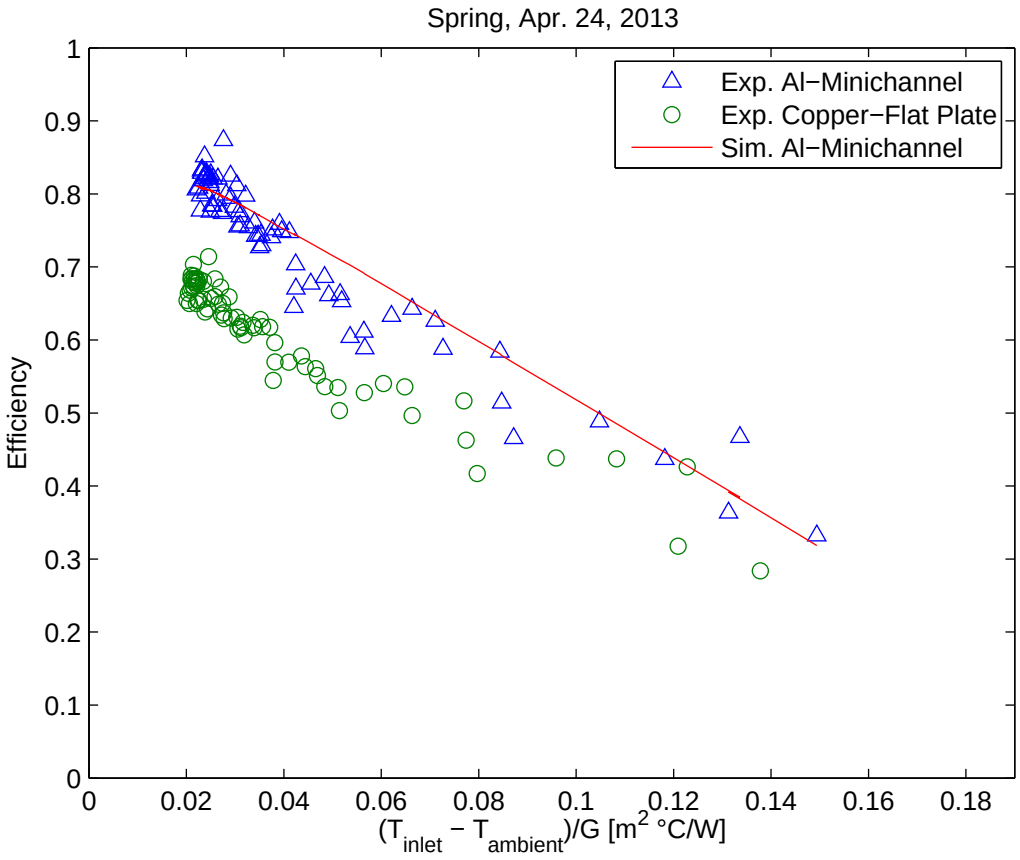

Figure 3.3: Thermal efficiency comparison of experimental aluminum minichannel and copper flat-plate solar collectors, and mathematical model of aluminium minichannel solar collector in terms of $(T_{inlet} - T_{\infty})/G_s$ in Spring, April 24, 2013.

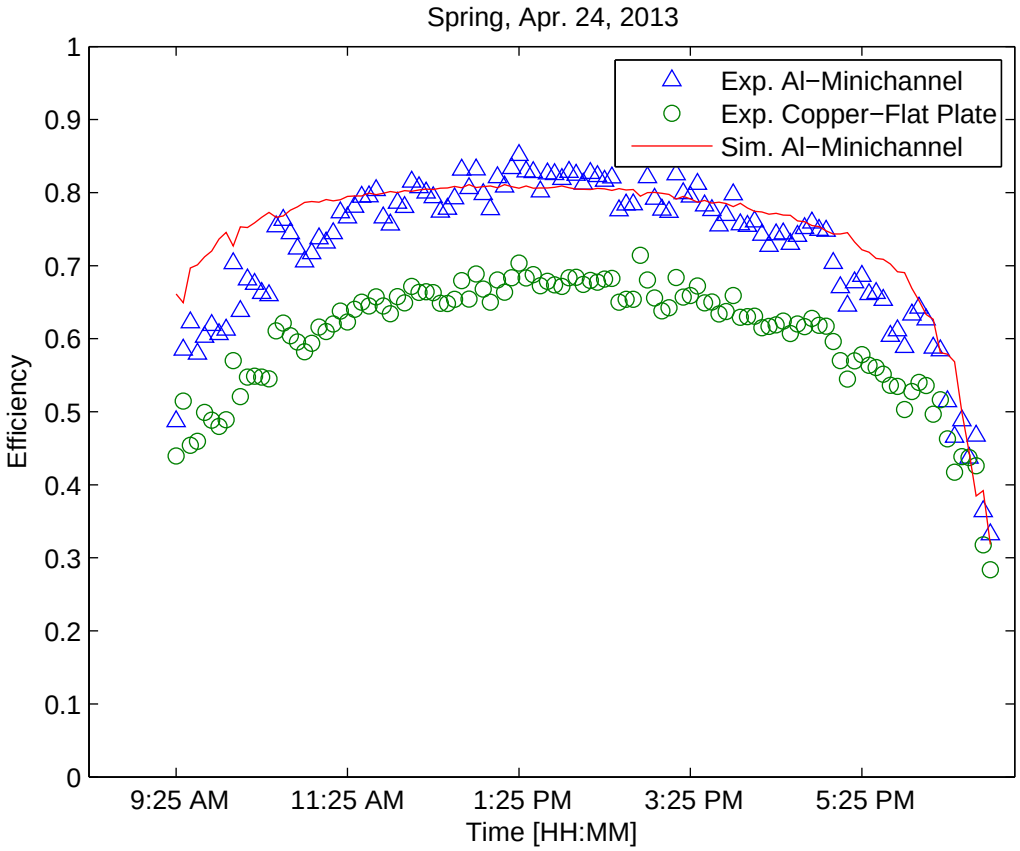

Figure 3.4: Thermal efficiency comparison of experimental aluminum minichannel and copper flat-plate solar collectors, and mathematical model of aluminium minichannel solar collector in terms of time of day in Spring, April 24, 2013.

Chapter 4

TWO-PHASE FLOW MATHEMATICAL MODEL

Two-phase flow occur in fluid mechanics where two different phases flow simultaneously. Phases are a state of matter, such as vapor, liquid or solid. Two-phase is a common type of multiphase flow when two of the three phases exist simultaneously in a flow system. The two-phase flow can exists as vapor-liquid, vapor-solid, or liquid-solid. The combination of states can be from a single fluid like steam-water, or a mixture of two fluids such as air-water [34]. Vapor-liquid is the most discussed and studied two-phase flow combination. Since the copper minichannel collector operates in a vapor-liquid two-phase flow, the term two-phase flow in this study refers to the vapor-liquid flow states.

Two-phase flow is widely used in the modern industry especially in refrigeration, air conditioning, food processing, automotive and electronics cooling. Two-phase flow applications are used to optimize system performance and efficiency. There are two design specifications that are important in two-phase flow systems: pressure drop and heat transfer coefficient. Pressure drop of a two-phase system is due to frictional, accelerational and gravitational effects. Calculating pressure drop determines the pumping power input that is used to circulate the working fluid through the system at a fixed flow rate. Being able to predict the pressure drop helps with determining the appropriate flow rate that will minimize power input and maximize energy output. Heat transfer coefficient, also known as convection coefficient, is a parameter that quantifies the convective heat transfer between the working fluid and its surrounding, such as, the surface in contact with the working fluid. Calculating the heat transfer coefficient measures the working fluid rate of heat transfer capability. In a heat exchanger, a high heat transfer coefficient allows to reduce the size of the heat transfer area.

In an attempt to accurately model the performance of the copper minichannel solar collector under two-phase flow operating conditions, both a frictional pressure drop correlation to calculate total two-phase pressure drop and a heat transfer coefficient correlation are needed to obtain the overall performance in the copper minichannel solar collector. The mathematical model of the copper minichannel solar collector performance under two-phase flow operating conditions is similar to single-phase conditions except for a couple major changes. First major change, referring back to Section 3.1.3, reflect the energy balance at the absorber. The last

term, q_{cond}, of Eq. 3.3 changes due to the presence of two-phase flow; the heat transfer coefficient, h_{fluid}, in R_{fluid} term of R_{mc} in Eq. 3.4 is no longer a single-phase working fluid. A corresponding two-phase heat transfer coefficient from an appropriate correlation is needed to replace this term.

Another major change is q_{fluid} seen in section 3.1.4; q_{fluid} needs to reflect the phase changes of the working fluid. In terms of power and in the units of $[W]$, $\dot{Q}_{fluid}$ is replaced and given as:

$$\dot{Q}_{fluid} = \dot{m}\Delta i \tag{4.1}$$

where $\dot{m}$ is the total mass flow rate of the fluid and Δi is the change of specific enthalpy at the inlet and outlet of the collector ($\Delta i = i_{out} - i_{in}$). The inlet and outlet specific enthalpy can be determined by the saturated values and the quality, as in

$$i = i_v + x(i_v - i_l)$$

where i_v and i_l are the specific enthalpies at the saturated vapor and saturated liquid states, respectively, of the working fluid. In the two-phase flow mathematical model developed for the copper minichannel solar collector, the inlet conditions, such as temperature, pressure and vapor quality of the working fluid are given; with this information, the inlet specific enthalpy of the working fluid can be determined. By using a frictional pressure drop correlation in order to calculate total two-phase pressure drop in the collector, the pressure at the outlet of the collector can be determined. The two-phase pressure drop and heat transfer rate are coupled in two-phase flow calculations. The heat transfer analysis of the solar collector is coupled with the pressure drop and heat transfer analysis of the two-phase flow inside the collector tubes to determine overall performance of the collector. The set of equations is solved using EES [30].

More detail about two-phase pressure drop and heat transfer coefficient are given in the rest of the chapter. Important terminology, and other two-phase parameters that are required to calculate pressure drop and the heat transfer of the system are explained. Several pressure drop and heat transfer correlations are described and compared to experimental data from available literature to find the best correlation to represent the copper minichannel solar collector. Applying the pressure drop and heat transfer coefficient correlations in the copper minichannel solar collector mathematical model, simulations to analyze the performance of the collector during two-phase flow is presented.

4.1 Definitions and Terminologies

Before discussing about two-phase pressure drop and heat transfer coefficient correlations, some important terminologies and concepts of two-phase flow are introduced since they are repeatedly used throughout the chapter. For an in-depth

understanding of two-phase or multiphase flow phenomena, readers are referred to Collier, Brennen, and Carey [35–37].

To describe the motion of the flow, a few definitions are used. The mass flow rate ($\dot{m}$) has units of $[kg/s]$. The total mass flow rate is the sum of the mass flow rates of the liquid ($\dot{m}_l$) and vapor ($\dot{m}_v$):

$$\dot{m}_{total} = \dot{m}_l + \dot{m}_v \tag{4.2}$$

The total mass flux (G) has units of $[kg/m^2s]$, and it can be defined as the ratio of the mass flow rate and the free flow area:

$$G = \frac{\dot{m}_{total}}{A_{free}} \tag{4.3}$$

The vapor quality, or flow quality, is dimensionless defining the ratio of saturated mixture, or the ratio of the mass of vapor and the total mass of the mixture:

$$x = \frac{m_v}{m_v + m_l} = \frac{m_v}{m_{total}} \tag{4.4}$$

Vapor quality can also be defined as the following,

$$x = \frac{y - y_l}{y_v - y_l} \tag{4.5}$$

where y can represent a thermophysical property such as specific entropy, specific enthalpy, specific volume or specific internal energy. The subscripts l and v are the specific property value of the working fluid at saturated liquid and vapor states, respectively.

Void fraction is used in calculating two-phase pressure drop and sometimes in calculating heat transfer coefficient, depending on the correlation. Void fraction is the ratio of the cross-sectional area that is occupied by vapor to the total cross-sectional area of a tube, or given as:

$$\alpha = \frac{A_v}{A_{total}} = \frac{A_v}{A_l + A_v} \tag{4.6}$$

where A represents the cross-sectional area, and the subscripts v, l, and *total* identifies vapor, liquid and total cross-sectional area, respectively. Void fraction can also be defined as the ratio of volume of space the vapor occupies in a two-phase flow in a tube [34]. Since the volume of vapor is difficult to calculate, there are many correlations in the literature to predict void fraction. For the calculation of two-phase flow in the copper minichannel tubes, the void fraction correlation of

Steiner [38], a version of the drift flux model of Rouhani and Axelsson [39] is used and recommended by Ould Didi et al. [40] and Thome [41]. For horizontal tubes:

$$\alpha = \frac{x}{\rho_v}\left[(1+0.12(1-x))\left(\frac{x}{\rho_v}+\frac{1-x}{\rho_l}\right)+\frac{(1.18-x)\left[g\sigma(\rho_l-\rho_v)\right]^{0.25}}{G\rho_l^{0.5}}\right]^{-1} \tag{4.7}$$

For vertical tubes when $\alpha > 0.1$, void fraction correlation by Rouhani and Axelsson [39] can be used:

$$\begin{aligned}\alpha = \frac{x}{\rho_v}\Bigg[\Bigg[1+0.2\,(1-x)\left(\frac{gD_h\rho_l^2}{G^2}\right)^{0.25}\Bigg]\left(\frac{x}{\rho_v}+\frac{1-x}{\rho_l}\right) \\ +\frac{1.18(1-x)\left[g\sigma\left(\rho_l-\rho_v\right)\right]^{0.25}}{G\rho_l^{0.5}}\Bigg]^{-1}\end{aligned} \tag{4.8}$$

From the equations above, x is the vapor quality, ρ is the density $[kg/m^3]$, g is the gravitational constant $(9.81 m/s^2)$, σ is the surface tension $[N/m]$, G is the total mass flux $[kg/m^2 s]$, D_h is the hydraulic diameter of the tube $[m]$, and the subscripts v, l and *total* identifies the vapor state, liquid state, and total mixture, respectively. Other widely used void fraction expressions in two-phase flow literature include Zivi's [42] and Baroczy's [43].

4.2 Two-Phase Pressure Drop

The conservation equations of two-phase flow is developed using the laws of conservation of mass, momentum and energy. Derivation of pressure drop using two-phase flow conservation equations is lengthy and will not be covered here. Readers are referred to literature by Collier, Brennen, Carey or Hewitt [35–37, 44, 45].

In general and in final form, the calculation of two-phase pressure drop for flow inside any tube is based on three components: static or gravitational pressure drop (ΔP_{static}), momentum or accelerational pressure drop (ΔP_{mom}), and frictional pressure drop (ΔP_{fric}). The total two-phase pressure drop is expressed as,

$$\Delta P_{tp,total} = \Delta P_{static} + \Delta P_{mom} + \Delta P_{frict} \tag{4.9}$$

Momentum or accelerational pressure drop is the pressure drop due to the change of kinetic energy of the flow [41]. The momentum pressure drop is expressed as,

$$\Delta P_{mom} = G^2\left(\left[\frac{(1-x)^2}{\rho_l(1-\alpha)}+\frac{x^2}{\rho_v\alpha}\right]_{out}-\left[\frac{(1-x)^2}{\rho_l(1-\alpha)}+\frac{x^2}{\rho_v\alpha}\right]_{in}\right) \tag{4.10}$$

where G is the total mass flux of the mixture, x is the vapor quality, ρ_v and ρ_l is the density of the vapor and liquid, respectively, and α is the void fraction.

Static or gravitational pressure drop is the pressure drop due to the change of the flow in elevation [34]. The static pressure drop is given by:

$$\Delta P_{static} = [\rho_l(1-\alpha) + \rho_g \alpha]\, gH \sin\theta \tag{4.11}$$

where g is the gravitational constant, H is the vertical height, and θ is the tilt angle of the collector with respect to the horizontal ground. If the collector is horizontal, then ΔP_{static} can be neglected since $H = 0$ and $\sin(\theta)$ at $\theta = 0$ is zero. In addition, according to Kim and Mudawar, gravitation effects can be neglected in minichannels and microchannels compared to larger channels and tubing. Minichannel and microchannels encounter higher shear or frictional stresses than in larger channels and tubing [46].

Frictional pressure drop can be defined as the pressure drop due to the wall frictional forces exerted upon the flow, or the work done by the shear forces at the tube wall and at the vapor-liquid interface [34, 46]. Frictional pressure drop is difficult and complex to predict accurately due to the fact it is dependent on many factors such as tube hydraulic diameter, mass flux of the flow, tube orientation, the interaction between the tube surface roughness and the two phases, working fluid properties and any interaction between the two phases. Usually, since both phases are present in a tube, there are smaller cross-sectional areas where both phases can flow through. The results is higher pressure drop in two-phase flow due to the friction between the phases in comparison to pressure drop due to momentum and static [34].

Since frictional pressure drop is difficult to account for, there are many correlations that have been developed in the literature during the past century. There are correlations that are developed for specific types of flow conditions, fluid types such as refrigerants, oils or gases, or specific type of tubing like sizing, cross-sectional shape, or orientation. There are other correlations that are developed to universally fit any type of fluid and tube configuration. Due to the numerous amount of frictional pressure drop correlations, it becomes difficult to choose one that would be accurate for a certain application. Two-phase frictional pressure drop correlations are developed differently depending on the methods the authors applied. The next subsection will discuss some of the popular methods that are used to develop frictional pressure drop correlations.

4.2.1 Model Types and Two-Phase Pressure Drop Definitions

Two-phase frictional pressure drop and certain heat transfer coefficient correlations are developed depending on the methods the authors applied. To get a better understanding of how many of these correlations are developed, these methods are discussed. The two most common methods are separated flow model and homogeneous flow model. There are other methods such as empirical, numerical and phenomenological models; these will be briefly mentioned.

4.2.1.1 Separated Flow Model

In a separated flow model, each state of the two-phase working fluid is assumed to be flowing separately from each other. In this case, some correlations developed by the separated flow model consider different velocities for each phase, whereas homogeneous flow model considers both phases having the same velocity.

To develop a two-phase frictional pressure drop correlation using separated flow model, it is common to use a two-phase multiplier method. According to Mekisso, the two-phase multiplier method appealed to most researchers since single-phase flow methods and results are analogous to two-phase flow by this method [34]. The two-phase multiplier method helped with eliminating the issue of which thermophysical properties of the phases should be used during the calculation of two-phase frictional pressure drop.

The concept of using the two-phase multiplier to calculate two-phase flow was first introduced by Martinelli et al. [47]. There are two approaches in modeling the two-phase multiplier. One is to consider that all the working fluid is assumed to be in one phase, whether it is considering all working fluid as liquid or as vapor. In this method, the total mass flux, or sum of the vapor and liquid mass flux, is used instead of the mass flux at a single phase. The two-phase multiplier is known as ϕ, and this approach is designated with subscripts 'lo' and 'vo' for liquid-only and vapor-only, respectively:

$$\Phi_{lo}^2 = \frac{\left[\frac{\Delta P}{\Delta L}\right]_{frict}}{\left[\frac{\Delta P}{\Delta L}\right]_{lo}} \tag{4.12}$$

$$\Phi_{vo}^2 = \frac{\left[\frac{\Delta P}{\Delta L}\right]_{frict}}{\left[\frac{\Delta P}{\Delta L}\right]_{vo}} \tag{4.13}$$

where $(\Delta P/\Delta L)_{frict}$ represents the two-phase frictional pressure drop gradient, and $(\Delta P/\Delta L)_{lo}$ and $(\Delta P/\Delta L)_{vo}$ are the single-phase pressure gradients assuming liquid-only and vapor-only, respectively.

The second approach to model the two-phase multiplier is to assume only one of the phases flows alone; it uses the respective mass flux of the phase when calculating Reynolds number [34, 48]. This approach is designated with subscripts 'l' and 'v' when liquid or vapor is the single phase considered:

$$\Phi_{l}^2 = \frac{\left[\frac{\Delta P}{\Delta L}\right]_{frict}}{\left[\frac{\Delta P}{\Delta L}\right]_{l}} \tag{4.14}$$

$$\Phi_{v}^2 = \frac{\left[\frac{\Delta P}{\Delta L}\right]_{frict}}{\left[\frac{\Delta P}{\Delta L}\right]_{v}} \tag{4.15}$$

where $(\Delta P/\Delta L)_l$ and $(\Delta P/\Delta L)_v$ are the single-phase pressure gradients assuming liquid and vapor phase that exists in the flow, respectively.

In the separated flow model approach, the liquid two-phase multiplier, or Eq. 4.14, is preferred due to the assumption that liquid density does not vary significantly in most applications in comparison to vapor density. Martinelli et al. first developed the two-phase multipliers concepts of Eq. 4.14 and 4.15, liquid and vapor two-phase multiplier respectively, in 1944 [47]. A few years later in 1948, Martinelli and Nelson developed the concepts relating to Eq. 4.12 and 4.13, liquid-only and vapor-only two-phase multiplier respectively, and claimed that the two-phase multiplier of Eq. 4.12 is more useful and convenient in calculating two-phase flows in boiling and condensing conditions.

There are many correlations for two-phase multiplier in the literature. One of the common two-phase multiplier in literature, and also the one that will be used in this thesis unless noted otherwise, will refer to the two-phase multiplier by Martinelli et al., and notably used in the widely known Lockhart and Martinelli correlation [47,49]. The two-phase multiplier by Lockhart and Martinelli is a subsequent improvement of Martinelli and Nelson [50]. Lockhart and Martinelli developed a two-phase frictional pressure drop correlation by introducing a new parameter X to help identify the two-phase multiplier needed for the calculation. This parameter is better known as the Lockhart-Martinelli parameter in literature. Using thermophysical properties of the working fluid to calculate X, Φ can be identified and applied to Eq. 4.12 to calculate two-phase frictional pressure drop. X is the ratio of single-phase pressure drops for liquid and gas considering the ratios of mass flow rates, densities and viscosities, or

$$\left[\frac{\Delta P}{\Delta L}\right]_l = X^2 \left[\frac{\Delta P}{\Delta L}\right]_v \tag{4.16}$$

X is calculated and dependent on the type of flow mechanism of the liquid and vapor; the four flow mechanisms are viscous-viscous, viscous-turbulent, turbulent-viscous, and turbulent-turbulent. Liquid is expressed first, followed by vapor; for example, viscous-turbulent refers to the liquid being laminar and the vapor being turbulent. These four mechanisms applied to the X are expressed as:

$$X_{vv}^2 = \left(\frac{\dot{m}_l}{\dot{m}_v}\right)\left(\frac{\rho_v}{\rho_l}\right)\left(\frac{\mu_l}{\mu_v}\right) \tag{4.17}$$

$$X_{vt}^2 = Re_v^{-0.8}\left(\frac{C_l}{C_v}\right)\left(\frac{\dot{m}_l}{\dot{m}_v}\right)\left(\frac{\rho_v}{\rho_l}\right)\left(\frac{\mu_l}{\mu_v}\right) \tag{4.18}$$

$$X_{tv}^2 = Re_l^{0.8}\left(\frac{C_l}{C_v}\right)\left(\frac{\dot{m}_l}{\dot{m}_v}\right)\left(\frac{\rho_v}{\rho_l}\right)\left(\frac{\mu_l}{\mu_v}\right) \tag{4.19}$$

$$X_{tt}^{1.11} = \left(\frac{\dot{m}_l}{\dot{m}_v}\right)\left(\frac{\dot{\rho_v}}{\rho_l}\right)^{0.555}\left(\frac{\mu_l}{\mu_v}\right)^{0.111} \tag{4.20}$$

Table 4.1: Values of C_l and C_v for various flow types

Variables	v-v	v-t	t-v	t-t
C_l	0.046	16	0.046	16
C_v	0.046	0.046	16	16

where C_l and C_v are given in Table 4.1 developed by Lockhart and Martinelli [49].

By calculating the Reynolds numbers of the liquid and vapor phase separately, Lockhart and Martinelli suggested that if $Re < 1000$, then the phase is in the laminar (viscous) regime, and if $Re > 2000$, then the phase is in the turbulent regime. Between these two regimes is the transition regime. At this point, it is up to the user to decide which X parameter to use depending on their experiment and application.

Lockhart and Martinelli established the two-phase parameter in order to determine the multiplier needed to calculate the frictional pressure drop. However, their results were represented graphically, which is not convenient, in addition to causing major issues in terms of accuracy. Many two-phase pressure drop correlations proceeding Lockhart and Martinelli adapted the two-phase multiplier, as well as, adapting their concept of two-phase parameter. Fortunately, these correlations were developed with a convenient approach by formulating equations that would determine the two-phase multiplier with the two-phase parameter known. More details are presented in section 4.2.2.

4.2.1.2 Homogeneous Flow Model

Another common method of developing a prediction of two-phase flow is the homogeneous model. Its concepts are simpler than the separated flow model. The homogeneous flow model determines two-phase flows with single-phase pressure drop relations using average properties of the working fluid. It also assumes that the two-phases have the same mass flux.

Unlike the separated flow model, the homogeneous flow does not use a two-phase multiplier, however, it does involve expressions to calculate two-phase working fluid properties such as density, viscosity, Reynolds number and friction factor. For example, using concepts of a homogeneous flow model to calculate two-phase frictional pressure gradient is expressed as:

$$\left(\frac{\Delta P}{\Delta L}\right)_{fric} = \frac{2 f_{tp} G^2}{D_h \rho_{tp}} \tag{4.21}$$

where G is the mass flux of both phases of the working fluid, D_h is the hydraulic diameter, ρ_{tp} is the density of the two-phase working fluid, and f_{tp} is the friction

factor. Unless noted by the correlation authors, typically ρ_{tp} is calculated by

$$\frac{1}{\rho_{tp}} = \frac{x}{\rho_v} + \frac{1-x}{\rho_l} \tag{4.22}$$

The friction factor f_{tp} is dependent on which friction factor expression to use as well as the flow of the working fluid, and the smoothness and shape of the tubes. Like calculating two-phase multipliers and frictional pressure drop, there are empirical expressions or correlations in the literature to calculate two-phase friction factor. Many of these friction factor empirical formulas involve calculating two-phase Reynolds number and two-phase viscosity. Nonetheless like the friction factor, there are many different ways of calculating two-phase Reynolds number and viscosity [48].

4.2.1.3 Other Models

There are a few other noteworthy flow models in the literature that were used to develop predictions of two-phase flow. They are empirical model, numerical model and phenomenological models. In this subsection, these models will be briefly described.

First to mention, is the empirical flow model. Although there are parts of a two-phase correlation or two-phase parameter that are based on some sorts of experiments, there are two-phase correlations that are solely based on experiments [34]. In contrast, empirical flow model is not based on methods of separated flow model or homogeneous flow model. Correlations using empirical flow model are developed by taking data directly from experiment and curve-fitting. However, the issue is that these correlations are based on quality of data, as well as, the number of data points taken. In addition, these correlations may only work for specific types of fluids, tube dimensions, or other conditions.

Second method worth mentioning is numerical methods. Numerical methods used to solve two-phase flows include techniques such as computational fluid dynamics (CFD), differential analysis, and integral analysis [51]. These methods generally involve the laws of continuity and momentum for two-phase flow on a three dimensional grid. As numerical methods for solving the Navier-Stokes equation in single-phase are becoming more common and available, modeling the phase change in two-phase flows using numerical methods is becoming more accepted. Having multiple phases that have different fluid properties, and since the dispersion of the second phase is not distributed evenly across the tube, numerically modeling of two-phase flow is still under development. This makes numerical methods not practical for two-phase flow applications used today [34].

Lastly, phenomenological flow model heavily depend on observations of flow patterns and phase shapes. Generally, this involve examining the geometrical shapes of the liquid and vapor phase in the tubes. After investigation and categorizing the

geometrical flow patterns of the two phases, the developed formulas are applied to calculate two-phase flow in the tubes at that particular flow configuration. Once the flow pattern changes, another set of formulas are used for calculation. This causes major inaccuracy. Flow patterns are subjective and based on one's opinion and perception. In addition, no standardized flow map of flow patterns has been widely accepted yet. Depending on the author and investigator, there are as many as 16 different flow patterns reported in the literature [52]. There are also various flow maps based on an investigator's criterion. Flow maps define the transition of one phase to another of a two-phase flow by describing flow patterns.

4.2.2 Frictional Pressure Drop Correlations

Four frictional pressure drop correlations were selected to model the two-phase frictional pressure drop in the minichannel solar collector: Chisholm (1967), Muller-Steinhagen and Heck (1986), Mishima and Hibiki (1996), and Sun and Mishima (2009). Chisholm and Muller-Steinhagen and Heck correlations were chosen since many authors has used these two correlations in different tube configurations and fluid types. Mishima and Hibiki correlation was chosen since their correlation was developed when considering smaller diameter tubes. Sun and Mishima correlation was chosen since their correlation was developed considering smaller diameter tube, as well as, multi-port minichannel tube configurations. In addition, these correlations were chosen due to their repeated occurrence in the literature. In this subsection, these four correlations will be mathematically presented. At the end of the subsection, all four frictional pressure drop correlations will compared to experimental data retrieved from literature to select the frictional pressure drop correlation that would be used in the copper minichannel solar collector. Specifically, it will be coupled with a selected heat transfer coefficient correlation to complete the mathematical model in order to predict the performance of the minichannel solar collector under steam generation conditions.

4.2.2.1 Chisholm Frictional Pressure Drop Correlation

Chisholm is selected because it is one of the earlier correlations developed, and it is widely known and used in the literature [53]. This correlation is also meant to be used as a backbone for the Mishima-Hibiki and Sun-Mishima correlations.

In 1967 Chisholm reanalyzed Lockhart and Martinelli (1949) frictional pressure drop correlation and included the effect of interfacial shear forces. This allowed to predict the hydraulic diameters of the phases more accurately than Lockhart-Martinelli. In addition, the Chisholm correlation was presented in equation form making the correlation more convenient than a graphical presentation of the correlation by Lockhart and Martinelli. Chisholm's frictional pressure drop is developed

using separated flow model assuming all the flow is liquid and flows alone. The two-phase frictional pressure drop gradient is:

$$\left(\frac{dp}{dz}\right)_{frict} = \left(\frac{dp}{dz}\right)_{l} \Phi_l^2 \tag{4.23}$$

The liquid single-phase frictional pressure gradient is given by

$$\left(\frac{dp}{dz}\right)_{l} = f_l \frac{2G^2(1-x)^2}{D_h \rho_l} \tag{4.24}$$

where x is the vapor quality, G is the mass flux of the working fluid, D_h is the hydraulic diameter, and ρ_l is the density of the liquid phase. The liquid friction factor, f_l, is dependent on the Reynolds number of the flow. If the flow is laminar ($Re < 2000$), then

$$f_l = \frac{16}{Re_l} \tag{4.25}$$

If the liquid flow is turbulent ($Re \geq 2000$), then Blasius [54] friction factor is used:

$$f_l = \frac{0.079}{Re_l^{0.25}} \tag{4.26}$$

where Reynolds number for liquid flow is

$$Re_l = \frac{GD_h(1-x)}{\mu_l} \tag{4.27}$$

Chisholm simplified and reformulated the two-phase multiplier, Φ_l^2, in terms of Lockhart and Martinelli (1949) parameter, X (Eqs. 4.18 to 4.20), and included a constant, C, that is dependent on the two-phase flow mechanism. Chisholm's two-phase multiplier is given as,

$$\Phi_l^2 = 1 + \frac{C}{X} + \frac{1}{X^2} \tag{4.28}$$

The flow mechanism and value of C is provided in the table below:

The two-phase multiplier, Eq. 4.28, by Chisholm, became a staple to other proposed correlations. Chisholm two-phase multiplier will reappear again in the discussions of other two-phase frictional pressure drop correlations in this subsection.

In 1973, Chisholm proposed a new correlaiton, after investigating Baroczy's (1966) [55] graphical correlation. Chisholm modified Baroczy graphical two-phase frictional pressure drop correlation into sets of equations in order to predict the pressure drop of turbulent flow in evaporating two-phase flow in smooth tubes [34].

Table 4.2: Values of C constant in Chisholm (1967) correlation

Flow mechanism (liquid-vapor)	C
viscous-viscous	5
viscous-turbulent	12
turbulent-viscous	10
turbulent-turbulent	20

His new frictional pressure drop correlation considered the liquid-only and vapor-only method of separated flows and is presented as,

$$\left(\frac{dp}{dz}\right)_{frict} = \left(\frac{dp}{dz}\right)_{lo} \Phi_{lo}^2 \tag{4.29}$$

This new correlation introduced a new definition of liquid-only two-phase multiplier, Φ_{lo}^2 and two new parameters. Φ_{lo}^2 is defined as,

$$\Phi_{lo}^2 = 1 + \left(Y^2 - 1\right)\left[Bx^{(2-n)/2}\left(1-x\right)^{(2-n)/2} + x^{2-n}\right] \tag{4.30}$$

where x is the vapor quality and n is the exponent from Blasius friction factor expression ($n = 0.25$) [40,41]. Y is one of the new parameters representing the ratio of single-phase pressure drop gradient of vapor-only and liquid-only flows:

$$Y^2 = \frac{\left(\frac{dp}{dz}\right)_{vo}}{\left(\frac{dp}{dz}\right)_{lo}} \tag{4.31}$$

where the liquid-only single-phase pressure drop gradient and the vapor-only single-phase pressure drop gradient is given by:

$$\left(\frac{dp}{dz}\right)_{lo} = f_{lo}\frac{2G^2}{D_h\rho_l} \tag{4.32}$$

$$\left(\frac{dp}{dz}\right)_{vo} = f_{vo}\frac{2G^2}{D_h\rho_v} \tag{4.33}$$

The liquid-only and vapor-only single-phase friction factor, f_{lo} and f_{vo} respectively, has the same conditions as Eqs. 4.25-4.26, however, Reynolds number, Re_{lo} and Re_{vo}, are defined as

$$Re_{lo} = \frac{GD_h}{\mu_l} \tag{4.34}$$

$$Re_{vo} = \frac{GD_h}{\mu_v} \tag{4.35}$$

Parameter B is calculated based on the parameter Y and the mass flux G.

If $0 < Y < 9.5$ then,

$$\begin{aligned} B &= \frac{55}{G^{0.5}}, \quad \text{for } G \geq 1900\ kg/m^2s \\ B &= \frac{2400}{G}, \quad \text{for } 500 < G < 1900\ kg/m^2s \\ B &= 4.8, \quad \text{for } G \leq 500\ kg/m^2s \end{aligned}$$

If $9.5 \leq Y < 28$ then,

$$\begin{aligned} B &= \frac{520}{YG^{0.5}}, \quad \text{for } G \leq 600\ kg/m^2s \\ B &= \frac{21}{G}, \quad \text{for } G > 600\ kg/m^2s \end{aligned}$$

If $Y > 28$ then,

$$B = \frac{15000}{Y^2 G^{0.5}}$$

The latter two-phase frictional pressure drop correlation by Chisholm (1973) is applied to the copper minichannel solar collector. This correlation is applicable for vapor qualities from $0 \leq x \leq 1$.

4.2.2.2 Muller-Steinhagen and Heck Frictional Pressure Drop Correlation

The two-phase frictional pressure drop correlation by Muller-Steinhagen and Heck is considered solely empirical based on experiments and an interpolation between liquid-only flow and vapor-only flow [1]. This correlation was tested against a data bank containing $9,300$ measurements of a variety of working fluid types and flow conditions. Muller-Steinhagen and Heck observed that the frictional pressure drop increases with increasing vapor quality. By approximately $x \approx 0.85$, the frictional pressure drop is at its maximum before decreasing toward $x = 1$. Muller-Steinhagen and Heck two-phase frictional pressure drop correlation is given as,

$$\left(\frac{dp}{dz}\right)_{frict} = Y\left(1-x\right)^{1/3} + \left(\frac{dp}{dz}\right)_{lo} x^3 \tag{4.36}$$

where x is the vapor quality, and

$$Y = \left(\frac{dp}{dz}\right)_{lo} + 2\left[\left(\frac{dp}{dz}\right)_{vo} - \left(\frac{dp}{dz}\right)_{lo}\right] x \tag{4.37}$$

$(dp/dz)_{lo}$ and $(dp/dz)_{vo}$ are the liquid-only and vapor-only single-phase pressure drop gradients, respectively, given by Eqs. 4.32 and 4.33.

There are, however, two restrictions Muller-Steinhagen and Heck indicated when using this two-phase frictional pressure drop correlation. First, the liquid-only Reynolds number must be greater than 100. Secondly, the single-phase vapor-only pressure drop must be greater than the single-phase liquid-only pressure drop.

This two-phase frictional pressure drop correlation is applicable for vapor qualities from $0 \leq x \leq 1$. Tribbe and Muller-Steinhagen compared the Muller-Steinhagen and Heck correlation with several other correlations to a large database including working fluids such as water-steam, several refrigerants, air-oil, air-water, and cryogenics, and found that this method gives the best results [56].

4.2.2.3 Mishima and Hibiki Frictional Pressure Drop Correlation

Mishima and Hibiki (1996) studied the characteristics of two-phase flow in smaller diameter tubes of 1 to 4 mm such as flow regime, void fraction, slug bubbles and frictional pressure drop [57]. They developed a two-phase frictional pressure drop correlation based on Chisholm (1967) correlation and C parameter, Eqs. 4.23 and 4.28, respectively. Originally, Chisholm's C parameter was dependent on the flow regimes such as laminar or turbulent. Mishima and Hibiki observed that the Chisholm C parameter decreases with decreasing diameters realizing Chisholm C parameter is dependent of tube diameter. Mishima and Hibiki set to modify Chisholm C parameter making it a function of inner tube diameter. For circular tubes, Mishima and Hibiki modified Chisholm C parameter is given as,

$$C = 21\left(1 - e^{-0.333D}\right) \tag{4.38}$$

where D is the inner diameter of a circular tube. For non-circular tubes, Mishima and Hibiki modified Chisholm C parameter given as,

$$C = 21\left(1 - e^{-0.319D_h}\right) \tag{4.39}$$

where D_h is the hydraulic diameter of a non-circular tube.

Their study concluded that the modified Chisholm C parameter works well in both vertical and horizontal tube configurations, in round tubes and rectangular ducts, small diameters, and working fluids such as air-water, ammonia, and some gases and refrigerants.

4.2.2.4 Sun and Mishima Frictional Pressure Drop Correlation

As Sun and Mishima (2009) analyzed other prediction methods for two-phase frictional pressure drop for small channel tubes ranging hydraulic diameters of 0.506 mm to 12 mm, they proposed a new correlation with a modified Chisholm correlation and C parameter [58]. Their observations and statistical analysis showed that the Chisholm C parameter changes with Reynolds number. In addition, they found that the ratio of Chisholm C parameter and Lockhart and Martinelli X parameter,

C/X, is dependent on the ratio of vapor phase Reynolds number Re_v to liquid phase Reynolds number Re_l. Sun and Mishima proposed a two-phase frictional pressure drop correlation based on Chisholm (1967) correlation, Eq. 4.23, however the two-phase multiplier is modified to,

$$\Phi_l^2 = 1 + \frac{C}{X^{1.19}} + \frac{1}{X^2} \tag{4.40}$$

where X is the Lockhart and Martinelli parameter (Eqs. 4.17 to 4.20), and C is their new Chisholm parameter given as,

$$C = 1.79 \left(\frac{Re_v}{Re_l}\right)^{0.4} \left(\frac{1-x}{x}\right)^{0.5} \tag{4.41}$$

Re_v and Re_l are Reynolds number for vapor and liquid phase, and x is the vapor quality.

Sun and Mishima tested their new proposed correlation against a database of 2,092 data points from 18 published papers and compared it to twelve other correlations for prediction two-phase frictional pressure drop. They concluded that their correlation, in addition to Muller-Steinhagen and Heck (1986) correlation were the best in predicting experimental data.

4.2.2.5 Frictional Pressure Drop Correlations Comparison

In order to validate the mathematical model for predicting two-phase frictional pressure drop and concurrently select the best correlation to represent the copper minichannel solar collector, the four correlations for frictional pressure drop were tested against experimental data from literature. Available literature were limited to pressure data of certain working fluids, mass fluxes, saturation temperatures, tube configurations and hydraulic diameters, therefore, finding available experimental data that matches or even is similar to the copper minichannel solar collector operating conditions was difficult. Each of the copper minichannel tube in the collector has a hydraulic diameter of 2.2 mm and operated with water as the working fluid at a mass flux range of 25 to 250 kg/m^2s. Since the copper minichannel collector usually operates at the lower end of the mass flux range, the corresponding experimental data with mass flux of $50kg/m^2s$ from Jassim and Newell was utilized for choosing the two-phase frictional pressure drop correlation for the copper minichannel solar collector. Experimental two-phase frictional pressure drop data were digitally extracted from Jassim and Newell [59], however, the original experimental data and information about the experiment refers to Nino et al. [60]. The experimental data corresponds to adiabatic testing conditions on a 6-ports minichannel tube with a hydraulic diameter of 1.54 mm, R134A refrigerant as working fluid and a saturation temperature of 10 °C. The comparison of predicted values from each of the four correlations versus the experimental data is presented in Figure 4.1.

From Figure 4.1a, Chisholm correlation mostly under-predicted, while Mishima and Hibiki and Sun and Mishima, Figures 4.1c and 4.1d respectively, under-predicted the frictional pressure drop entirely, falling below the -30% error band consistently. The mean absolute error (MAE) is used to quantify and compare the errors of each correlation. The mean absolute error formula is given as,

$$\text{MAE} = \frac{1}{N} \sum \frac{|dp/dz_{frict,pred} - dp/dz_{frict,exp}|)}{|dp/dz_{frict,exp}|} \times 100\% \tag{4.42}$$

where N is the number of data points. From Table 4.3, the calculated mean absolute errors are given for each correlation. For this specific case, the mean absolute error for Chisholm is 118.7%, 32.1% for Muller-Steinhagen and Heck, 279.7% for Mishima and Hibiki, and 273.5% for Sun and Mishima. Clearly, Muller-Steinhagen and Heck predicted the best out of the four two-phase frictional pressure drop correlations.

More experimental data with various mass fluxes, saturation temperatures, hydraulic diameters and working fluids were used to compare the four correlations. The comparisons and plots are presented in Appendix B. In summary, the additional analysis shows a pattern, where at higher mass fluxes, Sun and Mishima correlation predicted the two-phase frictional pressure drop the best out of the four to a certain vapor quality. Table 4.3 includes the mean absolute errors of the additional cases comparing the performance of the four correlations. However, due to the low flow conditions in the copper minichannel collector, Muller-Steinhagen and Heck correlation proved to make the most accurate predictions. Therefore, Muller-Steinhagen and Heck correlation is used in the mathematical model of the copper minichannel solar collector during two-phase, steam generation.

4.3 Two-Phase Heat Transfer Coefficient

The topic of two-phase flow and convective boiling heat transfer is a lengthy discussion and continues to be researched and studied. Readers are referred to textbooks by Collier, Brennen, Carey and Hewitt for more details [35–37] for present state of knowledge of two-phase flows and heat transfer.

As Section 4.1 also applies to the study of heat transfer coefficient in two-phase flow, the next following subsection focuses on a more detailed discussion of heat transfer coefficient. Flow patterns in vertical and horizontal tubes are presented to generally understand the flow patterns and the mechanism of heat transfer caused by flow boiling. The rest of this section presents and introduces several heat transfer coefficient correlations applicable to the copper minichannel solar collector. By the end of this section, the heat transfer coefficient correlations are validated and compared to experimental data, and a heat transfer coefficient correlation is chosen to represent the copper solar collector in the two-phase flow and heat transfer mathematical model.

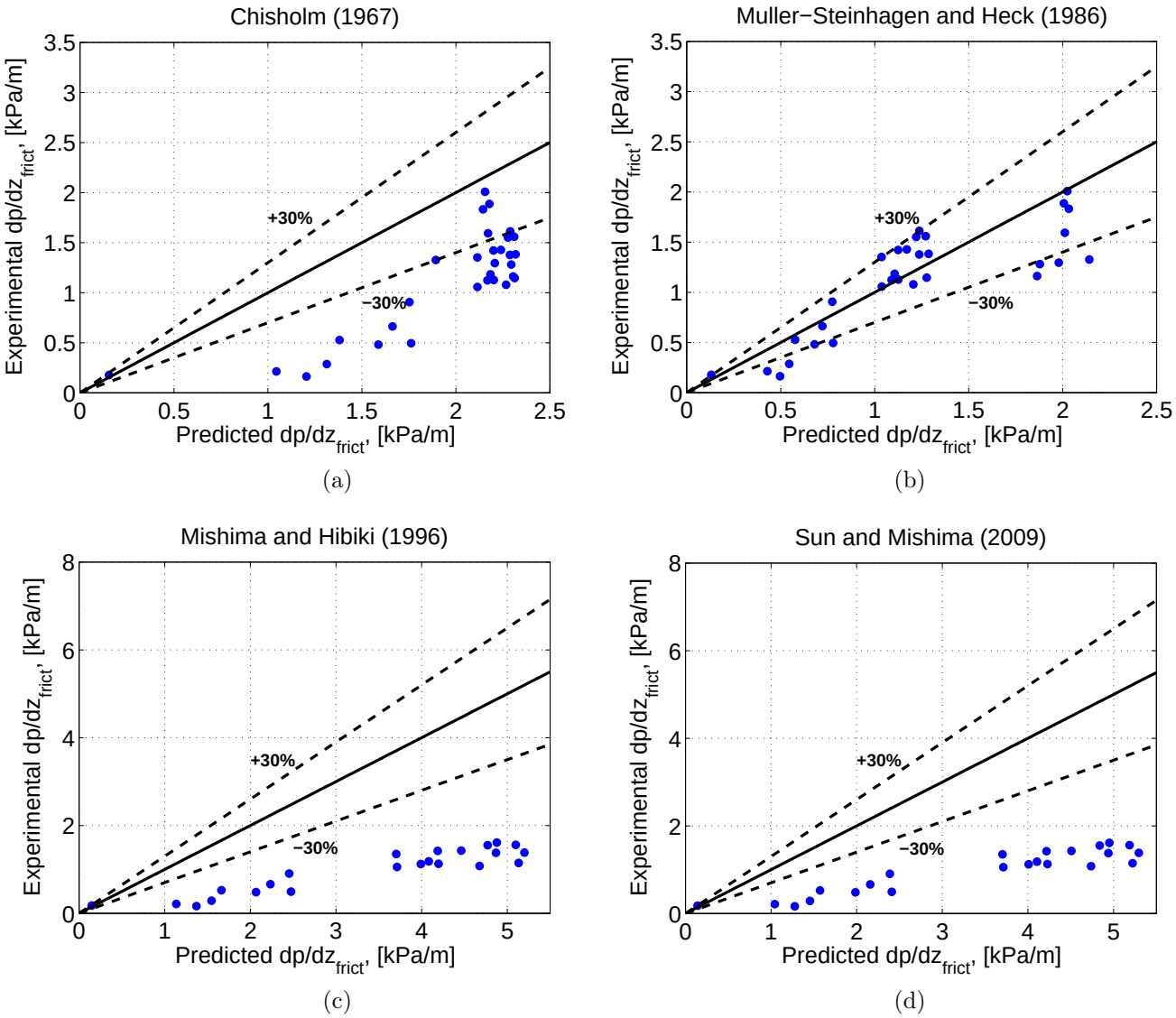

Figure 4.1: Predicted versus experimental two-phase frictional pressure drop in minichannel tubes of $D_h = 1.54\ mm$, R134a refrigeration working fluid, saturation temperature of 10 °C, and at a mass flux $G = 50\ kg/m^2s$ [59, 60].

Table 4.3: Mean absolute error of predicted versus experimental two-phase frictional pressure drop.

	MAE [%]			
	Chisholm [53]	Muller-Steinhagen and Heck [1]	Mishima and Hibiki [57]	Sun and Mishima [58]
R134A, $D_h = 1.54\ mm$ $T_{sat} = 10\ ^\circ C$ [59]				
G = 50 kg/m^2s	118.7	32.1	279.7[1]	273.5[1]
G = 100 kg/m^2s	73.5	24.3	98.7[2]	99.7[2]
G = 200 kg/m^2s	92.9	14.9	46.9[3]	48.4[3]
R410A, $D_h = 1.54\ mm$ $T_{sat} = 10\ ^\circ C$ [59]				
G = 100 kg/m^2s	117.2	42.8	127.5[4]	92.0[4]
G = 200 kg/m^2s	79.8	16.3	37.9[5]	34.7[5]
R12, $D_h = 2.64\ mm$ $T_{sat} = 65\ ^\circ C$ [61]				
G = 400 kg/m^2s	64.9	11.0	92.2	25.0
G = 600 kg/m^2s	37.1	15.0	73.0	14.9
G = 1000 kg/m^2s	19.3	21.8	61.8	12.3

[1] MAE calculated up to vapor quality, x$\approx$ 0.50.
[2] MAE calculated up to x$\approx$ 0.63.
[3] MAE calculated up to x$\approx$ 0.66.
[4] MAE calculated up to x$\approx$ 0.57.
[5] MAE calculated up to x$\approx$ 0.80.

4.3.1 Flow Patterns

One of the most basic ways to describe and visualize two-phase flow and heat transfer in tubes is by examining flow patterns or a boiling map. Because of gravitational forces, flow patterns are different when considering boiling heat transfer and two-phase flows in vertical and horizontal tubes. Flow patterns can be subjective to one's opinions and perceptions. Researchers may have different perceptions such as when one flow patterns starts or ends, how many flow patterns and heat transfer mechanisms there are, and what heat transfer mechanism dominates a particular flow pattern. According to Ferguson and Spedding, there may be as many as 16 flow patters identified [52]. The flow patterns and heat transfer regions presented below, and adapted from Collier and Thome, Thome, and Cheng et al. [35, 41, 62] can be agreed as rudimentary knowledge by most researchers.

First, consider a diabatic flow boiling in a vertical tube with a constant heat flux applied uniformly along its length. In Figure 4.2, the working fluid enters as a single-phase subcooled liquid from the bottom and eventually evaporates or transforms into pure vapor as it reaches to the top. At the bottom of the tube, region A, the liquid of the working fluid is being heated to its saturation temperature at the local pressure. At that region, the working fluid is at single-phase liquid form, and the tube wall temperature is below the temperature of the liquid. However at region B, as the temperature of the tube wall rises above the saturation temperature of the liquid, nucleate boiling occurs causing subcooled nucleate boiling flow and small vapor bubbles to appear on the tube wall. At region C, the working fluid reaches its saturation temperature causing convective boiling and a bubbly flow. This is the start of liquid-vapor, two-phase flow. Convective boiling, and some saturated nucleate boiling, continues in the working fluid changing flow patterns from slug or plug flow (region D) to churn flow (region E) to annular flow (region F). Partial way into the annular flow of region F, film evaporation occurs as the vapor dominated in the center of tube shears the working fluid from the wall. The film of the working fluid on the tube wall begins to shrink and evaporates; this is the onset of a dryout where the liquid film on the wall dries out. When the liquid film is completely gone, only a mist flow or presence of entrained droplets are present as seen in region G. Mist evaporation occurs as the temperature of the vapor in region G rises above the working fluid saturation temperature until the two-phase working fluid completely transform into single-phase vapor flow. The rise of temperature of the vapor in region G is caused by four heat transfer mechanisms: 1. single phase convection to the vapor, 2. heat transfer to the droplets within the mist flow, 3. heat transfer to the droplets caused by the tube wall, and 4. thermal radiation caused by the tube wall to the droplets [41]. From region G and into region H, all liquid from the working fluid is evaporated and single-phase vapor at vapor quality of one is dominant in the tube. At this point, heat transfer is caused by convection by the vapor.

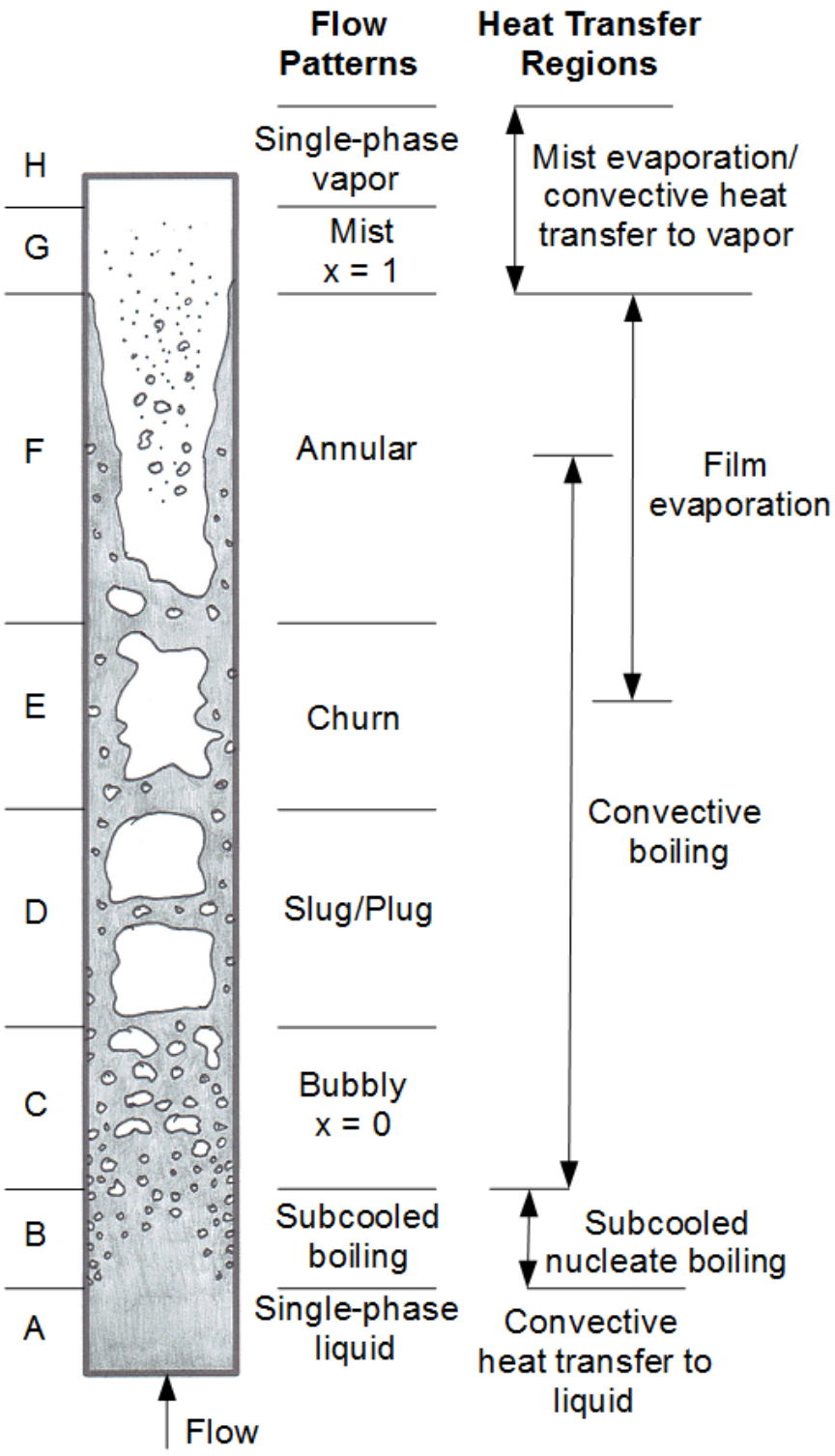

Figure 4.2: Flow patterns and heat transfer mechanism for flow boiling in a vertical tube. Adapted from Collier and Thome, Thome, and Cheng et al. [35, 41, 62].

Figure 4.3 shows flow patterns and heat transfer mechanisms by flow boiling in a horizontal tube. Due to the asymmetric vapor and liquid phase distributions in the tube caused by gravitational forces, this introduces more complications than flow boiling in vertical tubes [41, 62]. In Figure 4.3 starting region A, the working fluid enters the horizontal tube as a subcooled single-phase liquid. As the temperature of the tube wall starts to increase above the saturation temperature of the working fluid, small bubbles are formed on the tube wall and nucleate boiling occurs as seen in region B. In region C, plug or slug flow occurs as convective boiling continues. Eventually by region D as convective boiling continues, film boiling and evaporation occurs, annular flow develops leaving a thicker film on the bottom of the tube than at the top due to gravitational forces. Since the bottom has a thicker film, the top of the tube tends to start experiencing dryouts first. In addition to dryouts in the annular flow region, it is noted that there may be intermittent drying at other parts and perimeters of the horizontal tube, such as in the slug/plug flow area. At the slug/plug flow area, drying can occur on the top momentarily before a subsequent wave wets the top of the tube leaving a thin film of the liquid.

Similar to the flow boiling in a vertical tube, by region E of the horizontal tube, most of the film on the tube wall has evaporated or dried out. Mist flow and mist evaporation occurs as the temperature of the vapor in this region continues to increase pass the working fluid saturation temperature. By the end of region E and into region F, all liquid from the working fluid is evaporated and single-phase vapor is dominant in the tube. Heat transfer mechanism at this point is convection by the single-phase vapor.

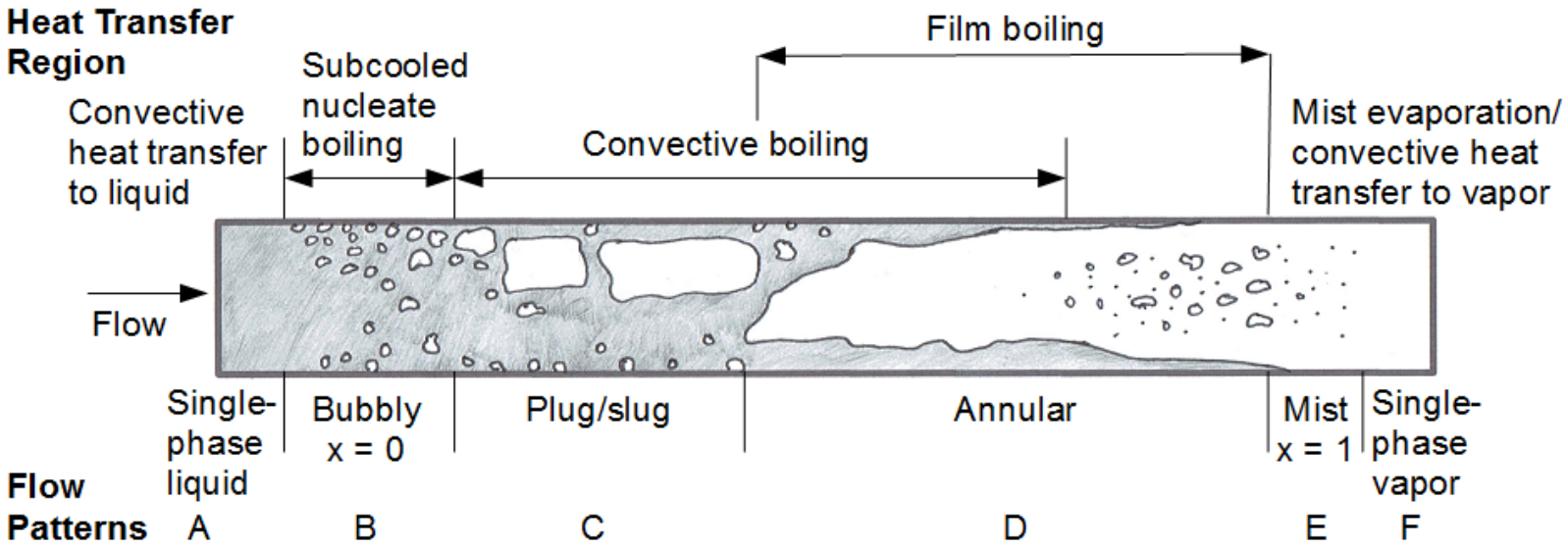

Figure 4.3: Flow patterns and heat transfer mechanism for flow boiling in a horizontal tube. Adapted from Collier and Thome, Thome, and Cheng et al. [35, 41, 62].

Many heat transfer coefficient correlations are developed from experiments while studying flow patterns and the heat transfer mechanism that occur at particular flow patterns. Many empirical predictive tools and correlations are based on the visuals of flow patterns. However, since most users who requires to predict or optimize a two-phase system do not own high resolution cameras and appropriate experimental equipment to capture the flow pattern in their system, researchers have generalized flow patterns and boiling mechanisms. By the generalization, dimensionless parameters were created to describe certain flow patterns or heat transfer mechanism occurring in two-phase boiling heat transfer. Using these dimensionless parameters, assisted in selecting the appropriate empirical formula to predict the heat transfer coefficient of the working fluid in the two-phase flow system. Some of these dimensionless parameters include boiling number (Bo), convection number (Co), Froude's number (Fr_{lo}), and Weber's number (We). Boiling number is represented by the ratio of heat flux to the product of mass flux and latent heat of vaporization ($Bo = \dot{q}/(Gi_{fg})$). It does not have a fundamental basis, however, it involves heat flux and mass flux which are important flow parameters. Convection number is a modified Martinelli number and introduced in Shah heat transfer coefficient correlation [63]. It is mainly used to distinguish between nucleate or convective boiling. Froude number is the ratio of inertial and gravitational forces; it was developed to classify stratification or wavy flow patterns. Weber number is the ratio of inertial to surface tension forces [64]. It is used to analyze the flow where interface between two different fluids or phases exists. More details and how these dimensionless parameters are used are presented in the following heat transfer coefficient correlations.

4.3.2 Heat Transfer Coefficient Correlations

Five heat transfer coefficient correlations are selected to model the boiling heat transfer in the copper minichanel solar collector: Kandlikar (1991), Shah (1982), Liu and Winterton (1991), Odeh et al. (1998), and Kaew-On and Wongwises (2009). Kandlikar, Shah, and Liu and Winterton correlations were chosen for their repeated occurrence in the literature. Many authors has repeatedly selected these correlations to predict heat transfer in different tube configurations and working fluid types. Odeh et al. correlation was chosen since the correlation was developed for predicting heat transfer in a direct steam generation solar collector. Kaew-On and Wongwises correlation was chosen since the correlation was developed for a multi-port minichannel tube configuration. In this subsection, the five correlations are mathematically described. By the end of the subsection, the heat transfer coefficient correlations are compared to experimental data collected from literature to select the best correlation to represent the copper minichannel solar collector. With the frictional pressure drop correlation chosen, the two different two-phase

correlations are coupled in order to predict the heat transfer and performance of the copper minichannel solar collector under steam generation conditions.

4.3.2.1 Kandlikar Heat Transfer Coefficient Correlation

Kandlikar's heat transfer coefficient correlation is chosen due to the correlation's popularity and the author's massive contribution of the study and research of two-phase flow. This correlation was proposed in 1991 and it was tested alongside other correlations by Shah, Gungor and Winterton, Chen and Bjorge et al. [63, 65–69] with 5,246 data points. It was also tested against various working fluids such as water, nitrogen, neon and refrigerants like R134A, R22, and R410A. Kandlikar's correlation can be used in vertical or horizontal tubes, and the correlation has been tested with different geometric tube configuration, for example, small diameter tubes, rectangular ducts, augmented tubes, compacted evaporators, and minichannel tubes [70, 71]. The objectives of Kandlikar correlation is to have the ability to calculate the heat transfer coefficient with any system parameters, i.e., tube configuration, working fluid type, and tube orientation [65]. The Kandlikar heat transfer coefficient correlation is given as,

$$h_{tp} = \left[C_1 Co^{C_2} \left(25 Fr_{lo}\right)^{C_5} + C_3 Bo^{C_4} F_{fl}\right] h_l \tag{4.43}$$

where Bo is the boiling number known as,

$$Bo = \frac{\dot{q}}{G i_{lv}} \tag{4.44}$$

$\dot{q}$ is the heat flux, G is the mass flux of the working fluid, and i_{lv} is the working fluid latent heat of vaporization. Fr_{lo} is known as Froude number with liquid-only flow. Froude number is given as,

$$Fr_{lo} = \frac{G^2}{\rho_l g D_h} \tag{4.45}$$

where ρ_l is the liquid density, g is the gravitational constant, and D_h is the hydraulic diameter. F_{fl} is the fluid-dependent parameter determined by experiments conducted by Kandlikar. A few values of F_{fl} is given in the Table 4.4.

Kandlikar heat transfer coefficient correlation is divided into two parts by considering whether the working fluid is in the nucleate boiling or convective region. C_1 to C_5 are also constants determined by Kandlikar, and Co, the convective number, ultimately determines these constants. The convection number is calculated by:

$$Co = \left(\frac{1-x}{x}\right)^{0.8} \left(\frac{\rho_v}{\rho_l}\right)^{0.5} \tag{4.46}$$

where x is the vapor quality and ρ_v is the vapor density. If $Co < 0.65$, then the working fluid is considered to be in the convective boiling region where convective

Table 4.4: Fluid dependent parameter in Kandlikar's heat transfer coefficient correlation.

Fluid	F_{fl}
Water	1.00
R22	2.20
R134A	1.63
R410A	1.72

mechanism are dominant. If $Co \geq 0.65$, then the working fluid is considered to be in the nucleate boiling region where nucleate boiling regime dominates. With the known Co value and which region the working fluid falls in, the corresponding values for C_1 to C_5 are given in Table 4.5.

Table 4.5: Constants in Kandlikar's heat transfer coefficient correlation.

Constant	Convective region	Nucleate boiling region
C_1	1.2360	0.6683
C_2	-0.9	-0.2
C_3	667.2	1058.0
C_4	0.7	0.7
C_5*	0.3	0.3

* $C_5 = 0$ for vertical tubes, or if $Fr_{lo} > 0.04$ in horizontal tubes.

Finally, h_l is the liquid single-phase heat transfer coefficient and it is given as,

$$h_l = 0.023 Re_l^{0.8} Pr_l^{0.4} \left(\frac{k_l}{D_h} \right) \tag{4.47}$$

where k_l is the liquid thermal conductivity. Re_l is the liquid Reynolds number defined in Eq. 4.27. Pr_l is the liquid Prandtl number, or

$$Pr_l = \frac{C_p \mu_l}{k_l} \tag{4.48}$$

where c_p is the specific heat of the working fluid.

4.3.2.2 Shah Heat Transfer Coefficient Correlation

Shah heat transfer coefficient correlation is also widely cited in the two-phase literature. In 1976, Shah developed a chart to predict heat transfer coefficients in two-phase flow [72]. The graphical correlation was difficult to implement in

computer calculations due to its graphical form raising inaccuracy concerns. Shah developed equations expressing this correlation in 1982 [63]. The correlation has been compared and tested against over 3,000 data points for 12 different fluids such as water and refrigerants (i.e., R11, R134A, R410A) in vertical and horizontal tubes of various diameters [63, 73, 74]. Shah reconfigured his chart correlation into equations by expressing his two-phase heat transfer coefficient correlation in terms of a dimensionless parameter:

$$\Psi = \frac{h_{tp}}{h_l} \tag{4.49}$$

where h_l is the single-phase liquid heat transfer coefficient, or Eq. 4.47. In order to determine Ψ, another dimensionless parameter, N, needs to be determined. For vertical tubes at all values of liquid-only Froude number, Fr_{lo}, and for horizontal tubes with $Fr_{lo} \geq 0.04$,

$$N = Co$$

For horizontal flows with $Fr_{lo} < 0.04$, then

$$N = 0.38 Fr_{lo}^{-0.3} Co$$

where Froude number Fr_{lo} and convection number Co are given in Eqs. 4.45 and 4.46, respectively.

Like Kandlikar's correlation, Shah determined that there were three regions where the boiling working fluid can be classified. Shah classified Ψ as one of the three regions of boiling: boiling suppression (bs), convective boiling (cb), or nucleate boiling (nb). For $N > 1.0$,

$$\Psi_{nb} = 230 Bo^{0.5}, \quad \text{for } Bo > 0.3 \times 10^{-4} \tag{4.50}$$

$$\Psi_{nb} = 1 + 46 Bo^{0.5}, \quad \text{for } Bo \leq 0.3 \times 10^{-4} \tag{4.51}$$

$$\Psi_{cb} = \frac{1.8}{N^{0.8}} \tag{4.52}$$

where Bo is the boiling number in Eq. 4.44. Ψ is the larger of Ψ_{nb} and Ψ_{cb}.

For $0.1 < N \leq 1.0$,

$$\Psi_{bs} = F Bo^{0.5} e^{2.74 N^{-0.1}} \tag{4.53}$$

and Ψ_{cb} is calculated using Eq. 4.52. Ψ is the larger of Ψ_{bs} and Ψ_{cb}.

Lastly, for $N \leq 0.1$,

$$\Psi_{bs} = F Bo^{0.5} e^{2.47 N^{-0.15}} \tag{4.54}$$

and Ψ_{cb} is calculated using Eq. 4.52. Ψ is the larger of Ψ_{bs} and Ψ_{cb}. The constant F in Eqs. 4.53 and 4.54 is determined by the boiling number:

$$\text{if } Bo \geq 11 \times 10^{-4}, \quad F = 14.7 \tag{4.55}$$

$$\text{if } Bo < 11 \times 10^{-4}, \quad F = 15.43 \tag{4.56}$$

4.3.2.3 Liu and Winterton Heat Transfer Coefficient Correlation

Liu and Winterton two-phase heat transfer coefficient correlation is also well-known in the two-phase literature [75]. Liu and Winterton correlation has been tested with different tube configurations such as circular and minichannel tubes of various diameters from 0.21 mm $< D_h <$ 32 mm, and also with different working fluids such as water, ethanol, CO_2 and refrigerants (i.e., R12, R11, R113, R134A, R410A) [70,75,76]. At the time the correlation was created, many other correlations predicting the heat transfer coefficient in two-phase flow contained an empirical boiling number correction. Liu and Winterton observed that the presence of the boiling number prevented the physicality of subcooled boiling. They developed a new correlation that has more reliance on a nucleate boiling term rather than a dependence on boiling number which would allow a more accurate prediction of heat transfer coefficient with a wide range of flow boiling conditions.

Liu and Winterton's correlation has two different forms based on tube orientation and Froude number, Fr_{lo} from Eq. 4.45. For vertical flows at any Fr_{lo}, or for horizontal flows at $Fr_{lo} > 0.05$,

$$h_{tp} = \left[(Sh_{nb})^2 + h_{cb}^2 \right]^{1/2} \tag{4.57}$$

where Sh_{nb} combined is the nucleate boiling mechanism. h_{nb} is obtained from Cooper's pool boiling correlation given as [77]:

$$h_{nb} = 55 M^{-0.5} P_{red}^{0.12} \left(-\log_{10} P_{red} \right)^{-0.55} \dot{q}^{2/3} \tag{4.58}$$

where M is the molecular weight, P_{red} is the reduced pressure ($P_{red} = P/P_{cr}$), P is the pressure of the working fluid and P_{cr} is the critical pressure S is known as the suppression factor:

$$S = \left[1 + 0.055 E^{0.1} Re_{lo}^{0.16} \right]^{-1} \tag{4.59}$$

where Re_{lo} is the liquid-only Reynolds number defined in Eq. 4.34. h_{cb} is the convective boiling heat transfer coefficient given as,

$$h_{cb} = E h_l \tag{4.60}$$

where h_l is the single-phase liquid heat transfer coefficient found in Eq. 4.47. E is the forced convective heat transfer enhancement factor developed for this correlation and can be calculated by

$$E = \left[1 + x Pr_l \left(\frac{\rho_v}{\rho_l} - 1 \right) \right]^{0.35} \tag{4.61}$$

For horizontal flows and at $Fr_{lo} < 0.05$, the heat transfer coefficient is,

$$h_{tp} = \left[\left(\sqrt{Fr_{lo}} Sh_{nb} \right)^2 + \left(Fr^{(0.1 - 2Fr_{lo})} h_{cb} \right)^2 \right]^{1/2} \tag{4.62}$$

4.3.2.4 Odeh et al. Heat Transfer Coefficient Correlation

Odeh et al. two-phase heat transfer coefficient correlation was created for a direct steam generation solar collector in 1998 [2]. Odeh et al. heat transfer coefficient correlation is based on multiple existing correlations and classified as either two flow patterns based on the calculation of Froude number: stratified flow or annular flow. Stratified flow occurs when there are little interaction between the two phases of the working fluid; this usually occurs when the working fluid is still subcooled, nucleate boiling is just beginning, and the liquid phase dominates the tube. Annular flow occurs when there is a layer or a film of liquid on the inner wall of the tube and the vapor flows in the center; annular flow usually occurs when the working fluid is going through convective boiling.

Using Eq. 4.45 for Froude number, when $Fr_{lo} < 0.04$ then stratified flow occurs and the heat transfer coefficient is given by Shah correlation [2, 66, 78]:

$$\frac{h_{tp}}{h_l} = 3.9 Fr_{lo}^{0.24} \left(\frac{x}{1-x}\right)^{0.64} \left(\frac{\rho_l}{\rho_v}\right)^{0.4} \tag{4.63}$$

If $Fr_{lo} > 0.04$ then the inner wall of the absorber tube is completely wet from annular flow. The heat transfer coefficient can be predicted using Chan correlation [2, 66, 78]:

$$h_{tp} = S h_{nb} + F h_l \tag{4.64}$$

where h_{nb} is the heat transfer coefficient in nucleate boiling regime and is given as,

$$h_{nb} = 3800 \left(\frac{\dot{q}}{20,000}\right)^n Fp \tag{4.65}$$

and n and Fp are given, respectively, as:

$$n = 0.9 - 0.3 \left(P_{red}\right)^{0.15} \tag{4.66}$$

$$Fp = 2.55 \left(P_{red}\right)^{0.27} \left(9 + \frac{1}{1-P_n^2}\right) P_n^2 \tag{4.67}$$

where $P_{red} = P/P_{cr}$ is the reduced pressure. P is the pressure of the working fluid and P_{cr} is the critical pressure.

S and F are the correction and enhancement factors, respectively, given by Gungor and Wintertor [66]:

$$S = \frac{1}{\left[1 + \left(1.15 \times 10^{-6}\right) F^2 Re_l^{1.17}\right]} \tag{4.68}$$

$$F = 1 + \left(2.4 \times 10^4\right) Bo^{1.16} + 1.37 \left(X_{tt}\right)^{-0.86} \tag{4.69}$$

where X_{tt} is the Lockhart-Martinelli parameter defined in Eq. 4.20.

4.3.2.5 Kaew-On and Wongwises Heat Transfer Coefficient Correlation

Studies of two-phase heat transfer coefficient in multi-port minichannel tubes are still relatively scarce. Comparatively, many investigators applied heat transfer coefficients correlation developed for small diameter tubes to minichannel tubes [79–82].

While investigating and comparing other heat transfer coefficient correlations, Kaew-On and Wongwises proposed a new correlation specifically for multi-port minichannel tubes based on their experimental data [79]. Their proposed heat transfer coefficient correlation is in the form of Lee and Lee [83]:

$$h_{tp} = Sh_l \tag{4.70}$$

where h_l is the single-phase liquid heat transfer coefficient from Eq. 4.47. S is an additional factor and defined as:

$$S = 1.737 + 0.97\left(\beta\phi_l\right)^{0.523} \tag{4.71}$$

where β is the aspect ratio of a channel $(width/height)$ and ϕ_l is the two-phase multiplier defined in Eq. 4.28. For the two-phase multiplier in Eq. 4.28, C is redefined and given as,

$$C = -3.356 + 41.863e^A + B \tag{4.72}$$

where $A = -69.475\beta f_l D_h$ and $B = 498\beta f_l D_h$, and D_h is the hydraulic diameter in millimeters. f_l is the single-phase liquid friction factor from Haaland [84]:

$$4f_l = \left[\frac{1}{-1.8\log\left[\frac{6.9}{Re_l} + \left(\frac{\varepsilon/D_h}{3.7}\right)^{1.11}\right]}\right]^2 \tag{4.73}$$

where ε is the relative roughness of the tube.

4.3.2.6 Heat Transfer Coefficient Correlation Comparisons

In order to validate and compare the heat transfer coefficient correlations, two cases are observed. The first case is to compare the correlations to experimental heat transfer coefficients in a circular tube. Obtaining experimental data from Park and Hrnjak [74], experimental heat transfer coefficients of R410A flow in a copper tube with a $D = 6.1$ mm diameter and saturation temperature of $T_{sat} = -15$ °C are compared with the correlations results as seen in Figure 4.4. The refrigerant is flowing at a mass flux of $G = 100\ kg/m^2s$ with a constant heat flux of $\dot{q} = 2000\ W/m^2$ and a variation of inlet vapor quality from approximately 0.10 to 0.85. It

can be seen in Figure 4.4 that most of the results of the correlations fall within ±30% of the experimental data. Although the range of uncertainty seems high, according to two-phase heat transfer literature, correlations that fall within ±30% of the experimental results is considered a decent agreement between simulation and experiment [65,70,74,75,79]. It is noted that Kaew-On and Wongwises heat transfer coefficient correlation is not included for this case of a circular tube due to the fact that their correlation is developed for minichannel tubes; however, results for this correlation will be presented in the following paragraph for the second case.

Studies of two-phase heat transfer in multi-port minichannel tubes are still relatively new, however, it is gaining in popularity during the past decade. Experimental data from literature is limited in the minichannel tube configuration and more limited in desirable working fluid. The second case compares the heat transfer coefficient correlations with experimental data in a multi-port minichannel tube from Kaew-On and Wongwises [79]. The minichannel tube tested is made from aluminum, and it has three ports with a total hydraulic diameter of 3.48 mm. The operating conditions considered are working fluid of refrigerant R410A flowing through the minichannel tube at a mass flux of $G = 200\ kg/m^2s$, a saturation temperature of $T_{sat} = 10\ ^\circ$C, a inlet vapor quality of $x_{in} = 0.10$, and a variation of constant heat flux from about 1.5 to 12 kW/m^2. Figure 4.5 shows the experimental data versus the predicted data from the five heat transfer coefficient correlations. It can be seen that the heat transfer coefficients are more difficult to predict in minichnanel tubes. Certain correlations in Figure 4.5 such as Kandlikar, Shah, and Liu and Winterton shows at least half of their predictions falling over the ±30% uncertainty.

Table 4.6 presents the mean absolute error, Eq. 4.42, of the experimental versus predicted heat transfer coefficients from Figures 4.4 and 4.5. Two additional heat transfer coefficient cases are considered in a circular and minichannel tube with different mass fluxes and presented in Table 4.6; the graphical representations are referred to Appendix C.

From the graphical results comparing experimental and predicted heat transfer coefficients in a circular and a minichannel tube, as well as, the calculated mean absolute errors, Odeh et al. correlation is chosen to best represent the prediction of heat transfer coefficient in the copper minichannel solar collector.

4.4 Simulations of Copper Minichannel Solar Collector During Two-Phase Flow

Since steam generation is not currently produced directly from the collector as described in the experimental set-up in Section 2.2, validation of the two-phase mathematical model versus experimental results cannot be done at this time. Nonetheless, performance simulations and predictions of the copper minichannel

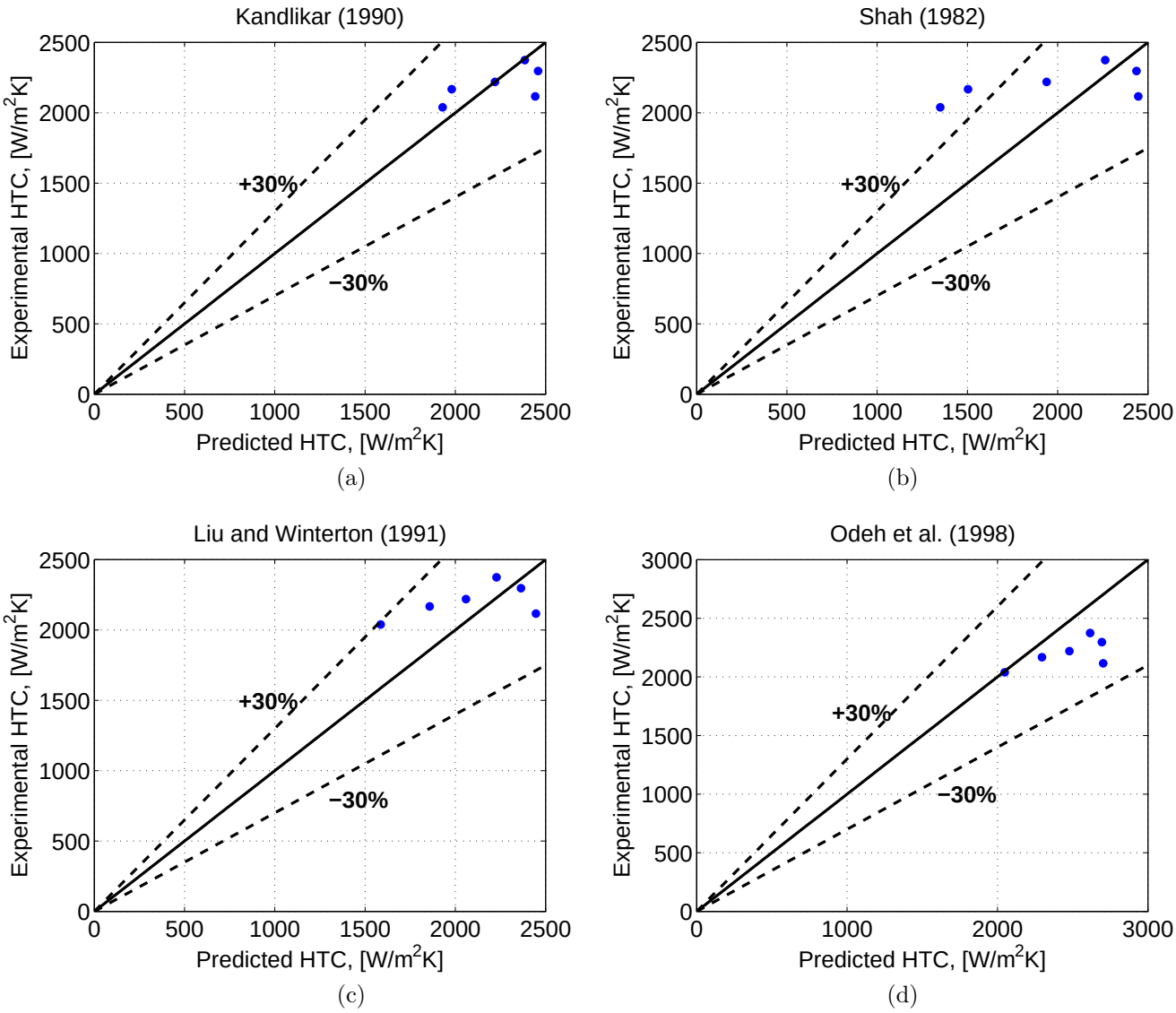

Figure 4.4: Predicted versus experimental two-phase heat transfer coefficient in a copper circular tube of $D = 6.1\ mm$, R410a refrigeration working fluid, saturation temperature of -15 °C, constant heat flux of $\dot{q} = 2000\ W/m^2$, and at a mass flux $G = 100\ kg/m^2s$ [74]. Correlations used: (a) Kandlikar (1990), (b) Shah (1982), (c) Liu and Winterton (1991), and (d) Odeh et al. (1998).

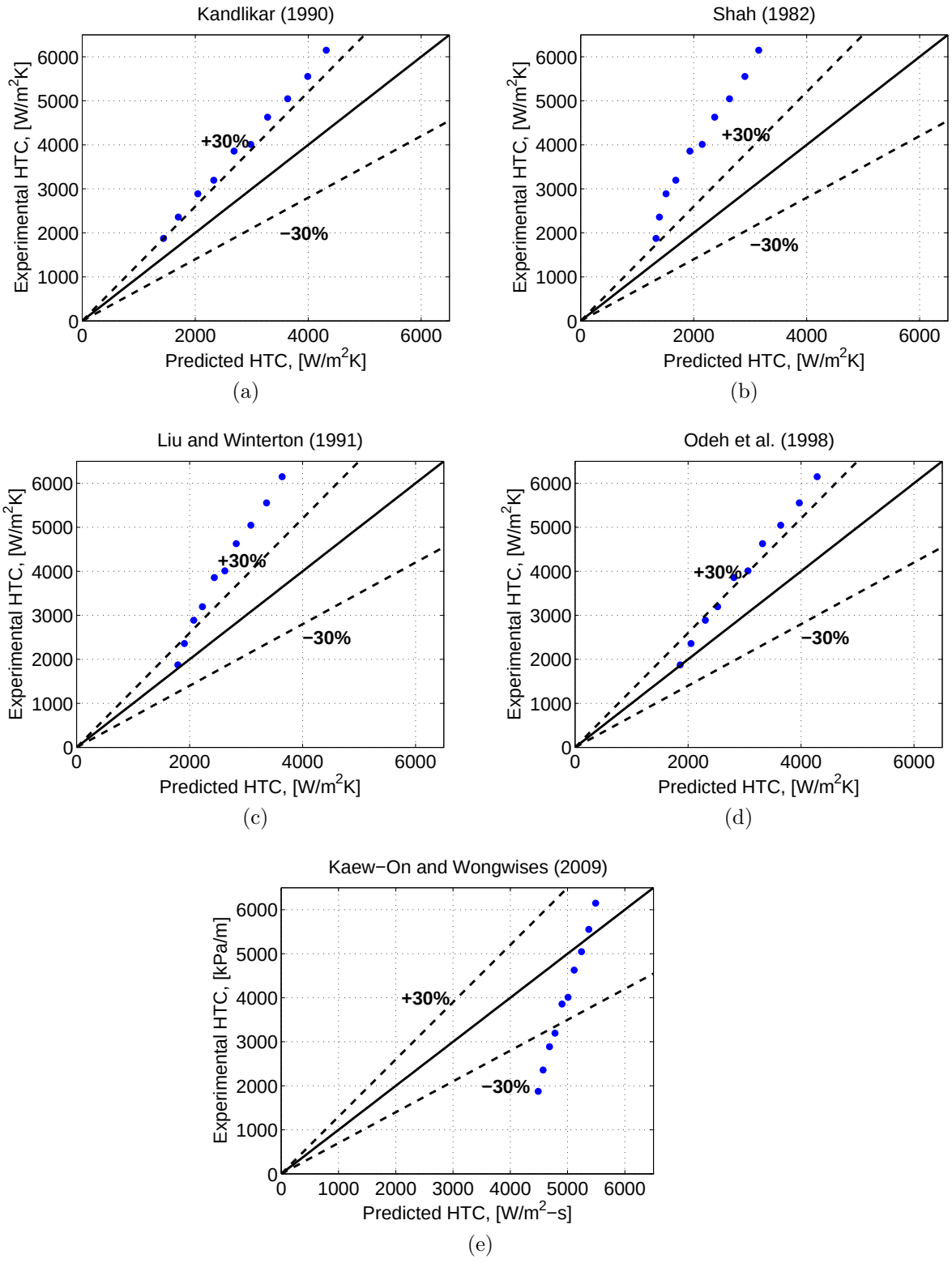

Figure 4.5: Predicted versus experimental two-phase heat transfer coefficient in a minichannel tube of $D_h = 3.48\ mm$, R410a refrigeration working fluid, saturation temperature of 10 °C, and at a mass flux $G = 200\ kg/m^2s$ [79]. Correlations used: (a) Kandlikar (1990), (b) Shah (1982), (c) Liu and Winterton (1991), (d) Odeh et al. (1998), and (e) Kaew-On and Wongwises (2009).

Table 4.6: Mean absolute error of predicted versus experimental two-phase heat transfer coefficient.

	MAE [%]				
	Kandlikar [65]	Shah [63]	Liu and Winterton [75]	Odeh et al. [2]	Kaew-On and Wongwises [79]
R410A, D_h = *3.48 mm* T_{sat} = *10 °C*, x_{in} = *0.1* [79]					
G = 200 kg/m^2s	27.8	45.4	31.1	22.1	38.7
G = 300 kg/m^2s	31.2	46.6	32.2	25.4	50.4
R410A, D = *6.1 mm* T_{sat} = *-15 °C*, q = *5000* W/m^2K [74]					
G = 100 kg/m^2s	6.2	17.2	11.4	12.2	-
G = 200 kg/m^2s	9.2	16.0	5.3	8.7	-

solar collector during two-phase flow in comparison to single-phase flow can be analyzed.

Figure 4.6 represents simulations comparing performance during single and two-phase flow in the copper minichannel solar collector. The plot compares the thermal efficiency versus a common parameter used in solar energy research $(T_{in} - T_\infty)/G_s$. Thermal efficiency is determined by the ratio of energy absorbed by the fluid to the energy transmitted through the collector, or $q_{fluid}/q_{absorbed}$ where q_{fluid} is described in Eq. 4.1 and $q_{absorbed}$ is described in Eq. 3.1. The simulations conducted with operating conditions such that the ambient temperature, T_∞, is at 30 °C, the flow rate of the working fluid in the copper minichannel solar collector is 10 L/min, and the solar irradiance, G_s, ranges from 400 to 1000 W/m^2. Single phase inlet temperatures are 50 and 90 °C, represented by black circles and blue triangles, respectively. Two-phase inlet temperatures are 100, 105 and 110 °C, represented by red pluses, green x's and yellow asterisks, respectively. Although it is difficult to tell, as the inlet temperatures increases, the efficiency decreases. Inlet temperature of 50 °C shows higher efficiency than the rest, while it can be seen that inlet temperature of 90 °C has slightly higher efficiencies than inlet temperatures at saturation liquid.

Figure 4.7 shows the same simulation, however, represented differently; it shows the thermal efficiency plotted against the various solar irradiance. From Figure 4.7, it can be seen that efficiency decreases as inlet temperature increases. There are higher differences of efficiencies at lower solar irradiance between the varying inlet temperatures, but the differences are lower at higher solar irradiance. From Figures 4.6 and 4.7, the simulations show that at higher solar irradiance, the efficiencies during two-phase flow are not penalized significantly in comparison to

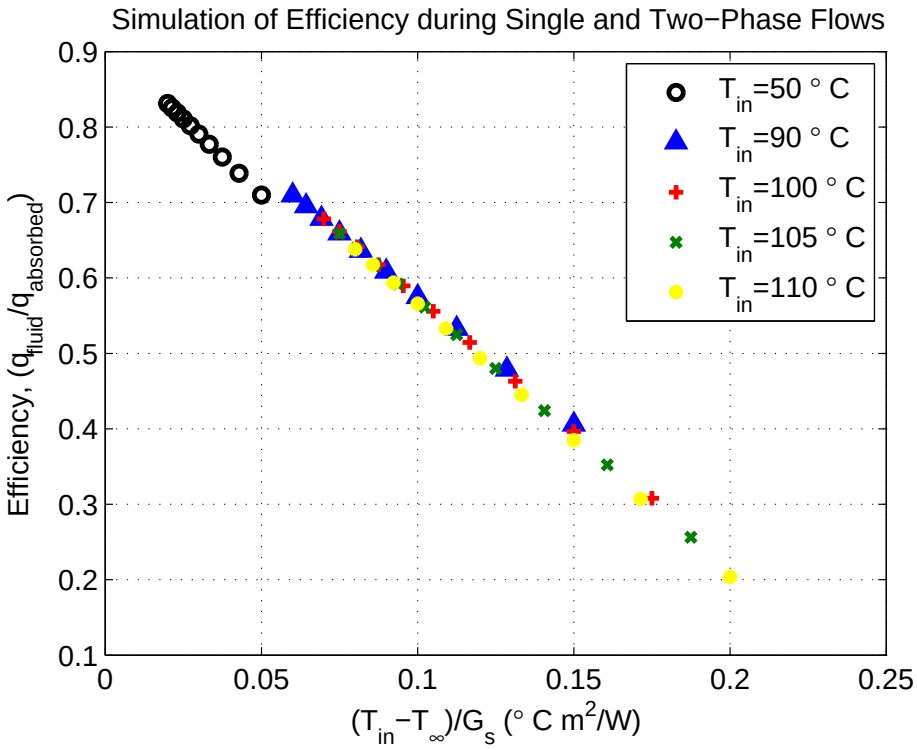

Figure 4.6: Comparison of simulated performance during single and two-phase flows in the copper minichannel solar collector by analyzing efficiency ($q_{fluid}/q_{absorbed}$) versus $(T_{in} - T_\infty)/G_s$. Single phase inlet temperatures are 50 and 90 °C, and two-phase inlet temperatures are 100, 105 and 110 °C. Inlet conditions are $T_\infty = 30$ °C, flow rate of working fluid in the collector is 10 L/min, and solar irradiance range from 400 to 1000 W/m^2.

single-phase flow with temperatures close to saturation temperature. The range of difference between entering in single-phase flow inlet temperature of 90 °C and in two-phase flow inlet temperature of 100 °C is 3% to 10% depending on the solar irradiance.

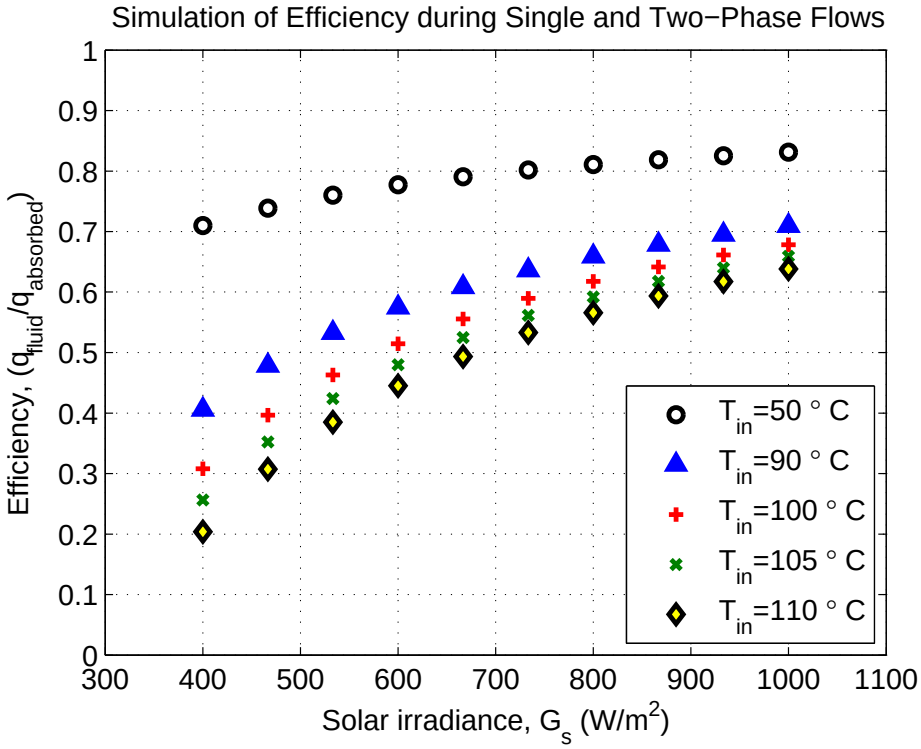

Figure 4.7: Comparison of simulated performance during single and two-phase flows in the copper minichannel solar collector by analyzing efficiency ($q_{fluid}/q_{absorbed}$) versus solar irradiance (G_s). Single phase inlet temperatures are 50 and 90 °C, and two-phase inlet temperatures are 100, 105 and 110 °C. Inlet conditions are T_∞ = 30 °C, flow rate of working fluid in the collector is 10 L/min, and solar irradiance range from 400 to 1000 W/m^2.

Figure 4.8 simulates the ratio of rate of energy loss to rate of energy transmitted to the collector, or $q_{loss}/q_{absorbed}$, during single and two-phase inlet operating temperatures. The rate of energy loss is determined by the sum of convective and radiative losses from the glass to the sky, or $q_{loss} = q_{conv,g-sky} + q_{rad,g-sky}$, where $q_{conv,g-sky}$ and $q_{rad,gsky}$ are referenced in Eq. 3.1. For this simulation, the inlet conditions are: ambient temperature T_∞ = 30 °C, flow rate of the working fluid at the collector is 10 L/min, and solar irradiance of G_s = 800 W/m^2. The inlet temperatures vary from entering single or two-phase with a range of 50 to 125 °C. From

Figure 4.8, it can be seen that the ratio of rate of energy loss to energy transmitted to the collector increases as inlet temperature of the collector increases. Higher heat losses occur at higher temperatures, therefore, more heat losses occur during two-phase flow than single-phase flow.

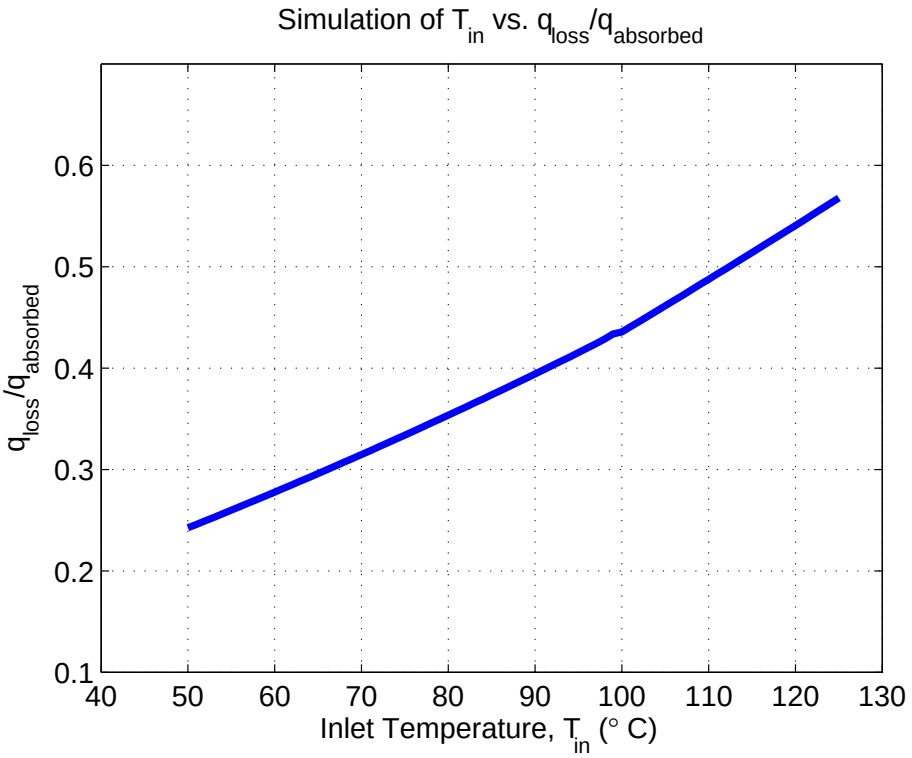

Figure 4.8: Comparing inlet temperature (T_{in}) and ratio of heat loss to heat transmited to the copper minichannel solar collector ($q_{loss}/q_{absorbed}$).

Chapter 5

EXPERIMENTAL ANALYSIS

This section presents and discusses the experimental results obtained with the different solar collectors. Section 5.1 presents performance of the aluminum minichannel and conventional copper flat-plate solar water heaters operating under a variety of ambient conditions between February 2013 to February 2014. Section 5.2 describes results obtained with the copper minichannel solar water heater.

5.1 Low temperature: aluminum minichannel and copper flat-plate solar water heaters

The performance of the aluminum minichannel solar water heater is presented first, followed by a performance comparison with the copper flat-plate solar water heater.

5.1.1 Performance of aluminum minichannel solar water heater

Experimental performance tests were conducted during more than a year in order to obtain a detailed characterization of the collectors. The test data covered Spring, Summer, Fall and Winter conditions. However, in this section individual Spring and Summer dates were chosen to show the performance of the aluminum minichannel solar water heater. Several measurements were taken and analyzed from the experiments: the temperature from the water storage tank, inlet and outlet temperatures at the collector, and the solar irradiance. These measurements were recorded every minute from sunrise to sunset.

Figure 5.1(a-b) shows a set of measured data plotted against time from Spring and Summer conditions. Each subfigure shows measured inlet temperature entering the solar collector (solid green line), outlet temperature exiting the collector (bold solid red line), and storage-tank water temperature (dashed blue line). The solar irradiance was also measured and recorded (dot-dash line).

A typical performance on a Spring day is shown in Figure 5.1(a). The Spring day selected was April 12, 2013 with ambient conditions fluctuating between 16 °C and 28 °C during operation depicted as circles in the figure. Data for present and historical ambient temperatures for a particular day were obtained from local

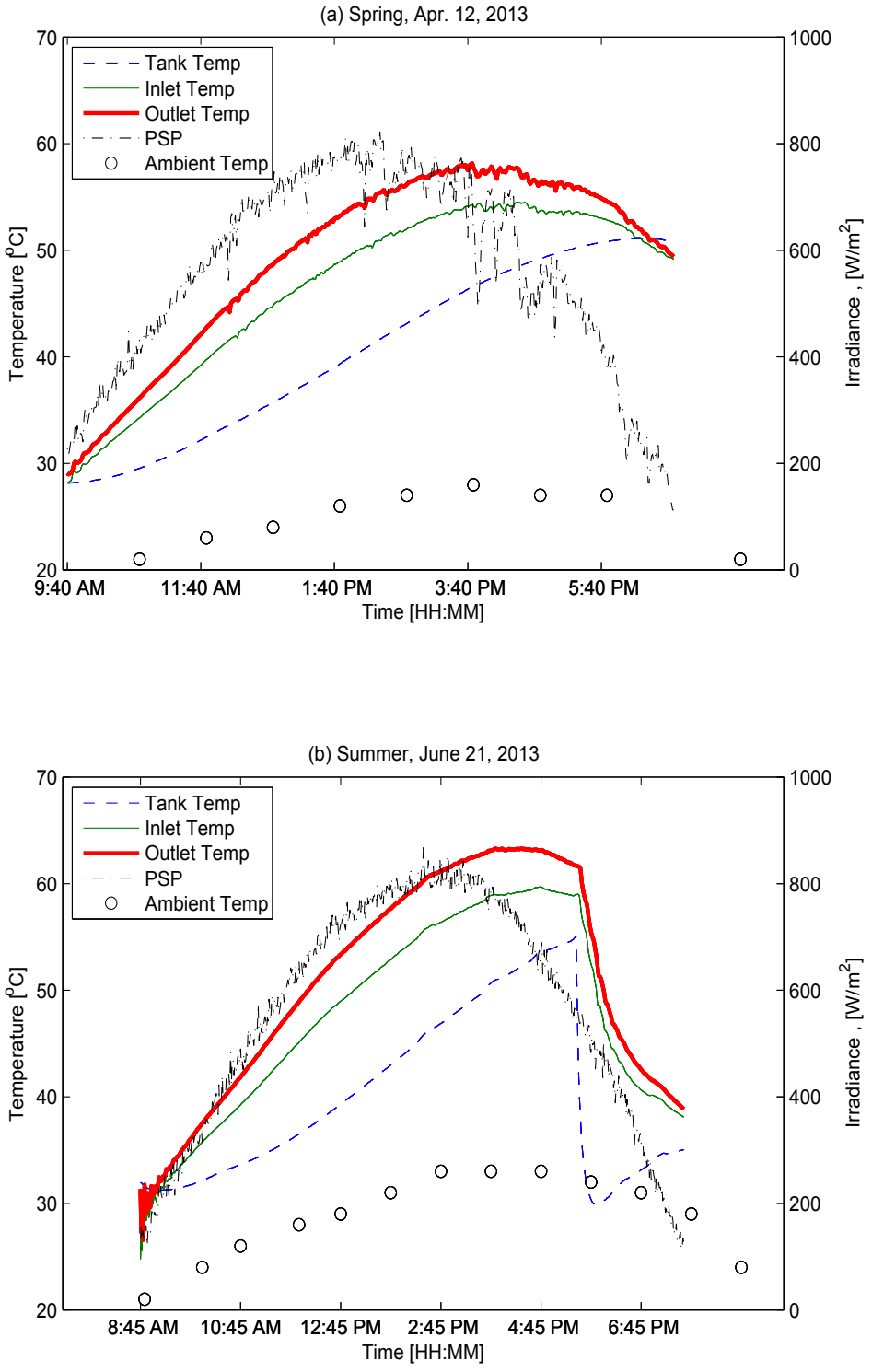

Figure 5.1: Aluminum minichannel solar water heater performance in (a) Spring, and (b) summer.

weather stations collected by Weather Underground[1]. The measured volumetric flow rate through the collector was set to 6.4 liters per minute. Under these conditions, there was an increase of temperature of about 23 °C in the water storage tank observed over the 9 hours of operation during the day. It was recorded that the maximum outlet temperature at the collector was 58.1 °C and the maximum difference between the inlet and outlet temperatures at the collector was 4.6 °C at 2:14 PM. Solar irradiance is shown on the right vertical axis, which reached a maximum value of 822 W/m^2 during the day. In the figure, the solar irradiance shows some oscillation and variability; this was due to the cloud cover during the afternoon. The maximum heat transfer rate calculated for this Spring day was 1.84 kW and the energy per unit area for the entire day of operation was approximately 3.2 kWh/m^2.

The date selected to represent a typical Summer day was June 21, 2013, and the performance of the aluminum minichannel solar water heater is presented in Figure 5.1(b). The ambient temperatures ranged between 21 °C and 33 °C during the day of operation. The volumetric flow rate was measured to be 6.4 liters per minute through the collector. The maximum outlet temperature at the collector reached 63.3 °C, while the maximum temperature difference between the inlet and outlet temperatures was 4.9 °C at 2:05 PM. It is seen that the water storage tank started at 31.6 °C in the morning and reached 55.1 °C by 5:27 PM in the afternoon triggering the control logic to open the discharge valve to cool the water storage tank, since the maximum water storage temperature was allowed to reach 55 °C. The discharge valve was closed at 5:48 PM when the temperature inside the tank reached below 30 °C. The temperature inside the water storage tank begun to rise again. The solar irradiance during the day reached a maximum of 867 W/m^2 at 2:24 PM. The maximum heat transfer rate obtained for this summer day was 1.92 kW and the total energy per unit area during the day of operation was 4.22 kWh/m^2.

5.1.2 Performance comparison with conventional copper flat-plate solar water heater

Selected dates of each season between February 2013 to February 2014 were examined to compare both the novel aluminum minichannel and conventional copper flat-plate solar water heater. February 13, 2014 was chosen to represent a typical Winter day; April 12, 2013 for a Spring day; June 21, 2013 for a Summer day; and September 28, 2013 for a Fall day. The comparison of temperatures at the water storage tank for the aluminum minichannel and copper flat-plate collectors are seen in Figure 5.2(a-d). The water storage tank temperature of the aluminum minichannel collector is represented by the red dashed line, and the water storage tank temperature of the copper flat-plate collector is represented by the green solid

[1]http://www.wunderground.com/history/

line. The solar irradiance (PSP) is depicted by a dot-dash line and the ambient temperature by circles.

Figure 5.2(a) corresponds to Winter conditions where ambient temperatures for that day ranged between 11 °C to 23 °C during the seven and a half hours of operation. The maximum solar irradiance reached 547 W/m^2 at 1:42 PM. The water storage tank of the aluminum minichannel collector started 0.4 °C above the temperature of the water storage tank of the copper flat-plate collector, which started at 24.3 °C. From Figure 5.2(a), it is observed that the pumps are turned off at 4:35 PM by the control logic due to low solar irradiance. However at that instance, the temperature in the water storage tank of the aluminum minichannel solar collector showed a higher value of 40.2 °C compared to the 38.5 °C of the water storage tank for the copper flat-plate collector, indicating a 1.3 °C increase in performance by the aluminum minichannel collector compared to the copper flat-plate collector.

The gain in temperature in the water storage tank of the aluminum minichannel solar collector can be seen again in Figure 5.2(b) corresponding to Spring time conditions. The ambient temperatures fluctuated between 16 °C and 28 °C during operation of the day. The water storage tank in the aluminum minichannel collector started at 28.1 °C which is 0.7 °C lower than the water storage tank of the copper flat-plate collector. Both systems operated for about 10 hours raising the water temperature in the storage tanks for the aluminum minichannel and copper flat-plate collectors by 22.6 °C and 20.3 °C, respectively. Therefore, the aluminum minichannel solar collector generated a net gain of 2.3 °C in the water storage tank with respect to the copper flat-plate solar collector. This net gain is significant considering each water storage tank carries a large volume of about 300 liters of water (80 gallons) each. The additional energy obtained from the net gain by the the aluminum minichannel collector was calculated to be 2,898 kJ or 805 Wh. This indicates that the aluminum minichannel design is capable of heating the storage tank quicker than the copper flat-plate design. A detailed analysis pertaining to the speed of response of the minichannel and copper flat-plate designs are presented in Section 5.1.3.

Figure 5.2(c) reports the performance comparison for a Summer day with ambient temperatures ranging between 21 °C and 33 °C during operation. In the morning, the water storage tank for the aluminum minichannel solar water collector started at 31.9 °C, which was 0.9 °C below the water storage tank temperature of the copper flat-plate collector. It can be seen that the discharge valve of the water storage tank for the aluminum minichannel solar collector opened at 5:37 PM due to the temperature of the water in the storage tank reaching the safety limit of 55 °C. On the contrary, the discharge valve of the water storage tank for the copper flat-plate solar collector never opened that day; the temperature in the water storage tank for the copper flat-plate solar collector did not reach the safety

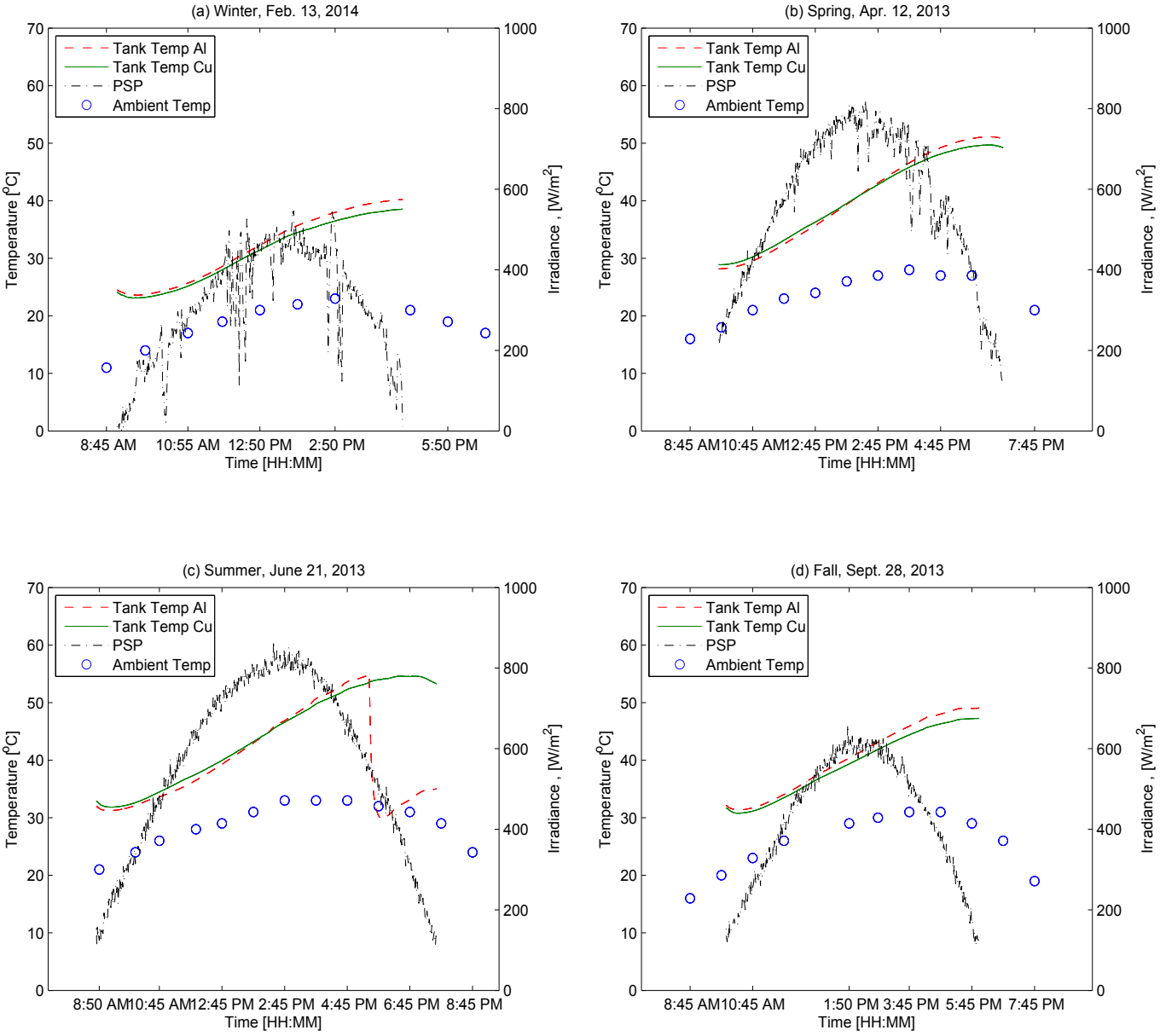

Figure 5.2: Comparison of aluminum minichannel and flat-plate copper solar water heater storage tank temperature in (a) Winter, (b) Spring, (c) Summer, and (d) Fall.

limit of 55 °C during the entire day of operation. Volumetric flow rates reported as 6.57 liters/min for the aluminum minichannel collector and 6.15 liters/min for the copper flat-plate solar collector with both pumps individually set to high speed. The maximum heat transfer rate was calculated to be 1.92 kW and 1.77 kW for the aluminum minichannel and copper flat-plate solar collectors, respectively. The total energy collected during the eleven hours of operation was 13.4 kWh for the aluminum minichannel collector and 12.1 kWh for the copper flat-plate collector.

Lastly, Figure 5.2(d) shows the comparison performance for a Fall day. This particular Fall day shows weather condition with low solar irradiance and ambient temperatures ranging from 16 °C and 31 °C during the hours of operation. During the entire day for both collectors, the water storage tanks did not reach the safety limit of 55 °C so the discharge valves did not open. Nonetheless, the aluminum minichannel solar water heater continues to consistently showed improvement in performance compared to the copper flat-plate solar water heater. For instance, during this day with eight hours of operation, the aluminum minichannel solar collector gained 17.0 °C while the copper flat-plate solar collector gained 15.6 °C.

In general, it was observed that during Summer when both the water storage tanks reached the safety limit of 55 °C triggering the discharge valve to open, usually the water inside the water storage tank of the aluminum minichannel solar collector consistently reached the safety limit approximately an hour faster than the the water in the water storage tank of the copper flat-plate solar collector. This can be seen in Figure 5.3 where the plot compares the water storage tanks temperatures throughout the day on June 27, 2013. At approximately 4:45 PM, the aluminum minichannel water storage tank reached the safety limit of 55 °C, triggering its discharge valve to open first. A little after an hour later, at approximately 5:51 PM, the copper flat plate water storage tank finally reached 55 °C, triggering its discharge valve to open. Although the water in the aluminum minichannel and copper flat plate water storage tanks started at, respectively, 29.6 and 28.9 °C, the temperature of the aluminum minichannel water storage tank (red-dashed line) increased much more rapidly than the copper flat plate water storage tank (green solid line) when comparing the lines on Figure 5.3.

5.1.3 Thermal efficiency

The thermal efficiency of the minichannel solar thermal collector was determined by taking the ratio between the heat transfer rate at the collector and the solar irradiance reaching the absorber:

$$\eta = \frac{\dot{Q}}{\left(\frac{\alpha_{Abs}\tau_g}{1-(1-\alpha_{Abs})\rho_g}\right) G_s A_{Abs}} \tag{5.1}$$

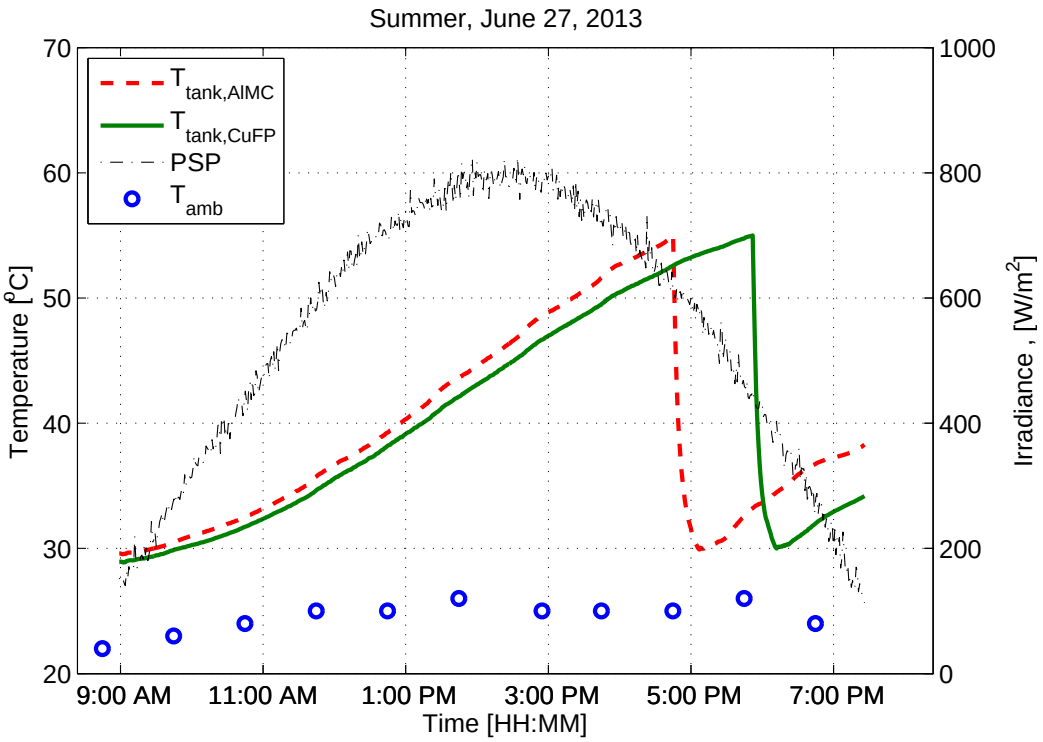

Figure 5.3: Comparison of aluminum minichannel and flat-plate copper solar water heater storage tank temperatures on a summer day (June 27, 2015).

In the equation above, $\dot{Q}$ is the heat transfer rate in the collector and is defined as $\dot{Q} = \dot{m}C_p\,(T_{out} - T_{in})$ and is similar to the definition of 3.8 without the division of the collector surface area; $\dot{m}$ is the mass flow rate of the working fluid flowing through the collector, C_p is the specific heat of the working fluid, G_s is the solar irradiance or total incident radiation hitting the collector per unit area, A_{abs} is the absorber area, and T_{out} and T_{in} are the outlet and inlet temperatures of the working fluid at collector, respectively.

As a note and also described in Chapter 2: Experimental Design, the absorber areas of the aluminum minichannel and the copper flat-plate solar collectors are different. The aluminum minichannel absorber area is $A = NWL$, where N is the number of minichannel tubes used to build the solar water heater, W is the width of each minichannel tube, and L is the length of the minichannel tubes. The area of the copper flat-plate collector corresponded to the area of the copper plate inside the collector metallic frame. A summary of the absorber areas and characteristic properties of the aluminum minichannel and copper flat-plate solar water heaters are presented in Table 5.1

Table 5.1: Collector properties of the aluminum minichannel and copper flat-plate solar water heaters.

Parameter	Aluminum Minichannel	Copper Flat-Plate	Units
Frame length	3048	3048	mm
Frame width	1219	1219	mm
Number of tubes	11	10	–
Absorber area	3.20	3.68	m^2
Absorber fin thickness	–	0.2032	mm
Glass transmissivity	0.909	0.909	–
Total free flow area	1015.5	1026.1	mm^2
Hydraulic diameter of each tube	1.42 mm	12.7 mm	
Ratio of free flow area to absorber area	317.3	278.8	mm^2/m^2
Collector mass (including headers and-without frame)	11.96	15.086	kg
Thermal inertia ($I = \sqrt{k\rho c_p}$)	22,492.7	34,438.3	J m^{-2} K^{-1} $s^{-1/2}$

The comparison of thermal efficiencies obtained experimentally for each collector during a Spring day is shown in Figures 3.3 and 3.4 of Section 3.1.5. As seen in the figures, the aluminum minichannel solar collector shows a higher efficiency obtained during the day with an average improvement of 12% in thermal efficiency with respect to the copper flat-plate solar collector. The difference can be examined and explained by a couple of phenomena. One explanation of the difference is by analyzing the thermal resistances of both solar collectors. The thermal resistance

from fluid to the air gap between the absorber and the glass for the conventional copper flat-plate collector is obtained from Duffie and Beckman [8]:

$$R_{fp} = W_t \left[\frac{1}{U_L \left(W_t - D_e \right) \eta_{fp}} + \frac{1}{\pi D_i h_{fp,i}} \right] \tag{5.2}$$

where U_L represents the overall heat transfer coefficient at the absorber surface, W_t is the tube spacing, D_e is the tube external diameter, D_i is the tube internal diameter, and $h_{fp,i}$ is the internal heat transfer coefficient. The fin efficiency is given by,

$$\eta_{fp} = \frac{tanh \left[m \left(W_t - D_e \right) / 2 \right]}{m \left(W_t - D_e \right) / 2} \tag{5.3}$$

where $m = \sqrt{\frac{U_L}{k_{fp} t_{fp}}}$. k_{fp} is the thermal conductivity and t_{fp} is the fin thickness. On the other hand, the thermal resistance for the aluminum minichannel collector (R_{mc}) is given by Equation 3.4 described in the previous chapter and reproduced below:

$$R_{mc} = \left(\frac{t_{abs}}{k_{abs}(L_{tube} a)} \right) + \left(\frac{t_{wall}}{k_{wall}(L_{tube} a)} \right) + \left(\frac{1}{\eta_o h_{fluid} A_{tube}} \right) \tag{3.4}$$

Under the operating conditions shown in Figure 3.3, R_{fp} is an order of magnitude larger than R_{mc}. This illustrates the beneficial aspects of the aluminum minichannel design: the avoidance of using thin metal sheet absorber attached to a tube reduces the thermal resistance. Compared to the copper flat-plate collector, where there is a temperature gradient in between the tubes at the absorber fin which can reach a few centigrade degrees, the aluminum minichannel tube is able to achieve uniform wall temperature across the width of the minichannel tube.

Another explanation of the efficiency gap between the aluminum minichannel and copper flat-plate in Figure 3.3 can be explained by the thermal inertia of the materials. The thermal inertia of a material is calculated by

$$I_{thermal} = \sqrt{k \rho c_p} \tag{5.4}$$

where k, rho, and c_p are the material's thermal conductivity, density and specific heat, respectively. Thermal inertia is the material's resistance to change in temperature. A higher value of thermal inertia means it would take a material longer to heat up or cool down. A lower value of thermal inertia means it would take a material quicker to heat up or cool down. The calculated thermal inertia of the aluminum minichannel and copper flat-plate solar collectors are shown in Table 5.1 and they are given as 22,492.7 and 34,438.3 (J m^{-2} K^{-1} $s^{-1/2}$), respectively. It can be seen that the thermal inertia of the aluminum minichannel solar collector is about 35% less than the thermal inertia of the copper flat-plate solar collector.

Lastly, using COMSOL Multiphysics[2] software, a simple transient heat transfer simulation is calculated to analyze the speed of response comparing the aluminum minichannel solar collector and the copper flat-plate solar collector. Due to the high computational power and time required for three-dimensional models, the analysis is simplified. An aluminum single-channel tube and a copper circular tube are representing the aluminum minichannel solar collector and the copper flat-plate solar collector, respectively. The single-channel tube has the dimensions of a single port of the aluminum minichannel tube, and the circular tube has the dimension of one of the tubes used in the copper flat-plate collector. For fairness, both tubes flow at the same Reynolds number corresponding to a typical Reynolds number used in both solar collectors during experiments ($Re = 169.5$). This simulation assumes pure conduction only and a constant heat flux of 500 W/m^2 applied to the top surface of the single-channel tube and the circumference of the circular tube. Water is used as the working fluid. The inlet temperature is 25 °C, and the temperature of all surfaces is initiated at 25 °C. Figure 5.4 shows the speed of response results of the single-channel tube and circular tube, comparing the average temperature of the fluid at the end of each tube versus the time lapsed. In addition, the average temperature of each tube material at the end of the tubes are also compared. Due to the nonexistent convective and radiative effects, the heat transfer by conduction continues to raise the temperature of both tubes. However, from the figure it clearly shows that due to the effective design, the minichannel tube is capable of raising the temperature of the working fluid quicker than a flat-plate collector. It is also shown that the temperature difference of the fluid and the tube material is small in the single-channel tube in comparison to the round tube due to the thin wall thickness.

5.2 Medium temperature: copper minichannel solar collector

The performance of the copper minichannel solar collector is presented in this section followed by a discussion of steam generation. Due to the low absorber area of the original solar collector, thermal losses along the pipes were very detrimental to the performance of the system. Therefore, modifications to the original system were made and are discussed first.

5.2.1 Modifications and adjustments to the copper minichannel solar collector

From April 2015 to mid June 2015, several tests were ran after the fabrication of the copper minichannel solar collector as described in Section 2.2.1. During these tests, the collector inlet and outlet temperatures would have difficulty reaching past 100 °C. The temperature readings at the flow meter and the inlet of the steam heat

[2] www.comsol.com/

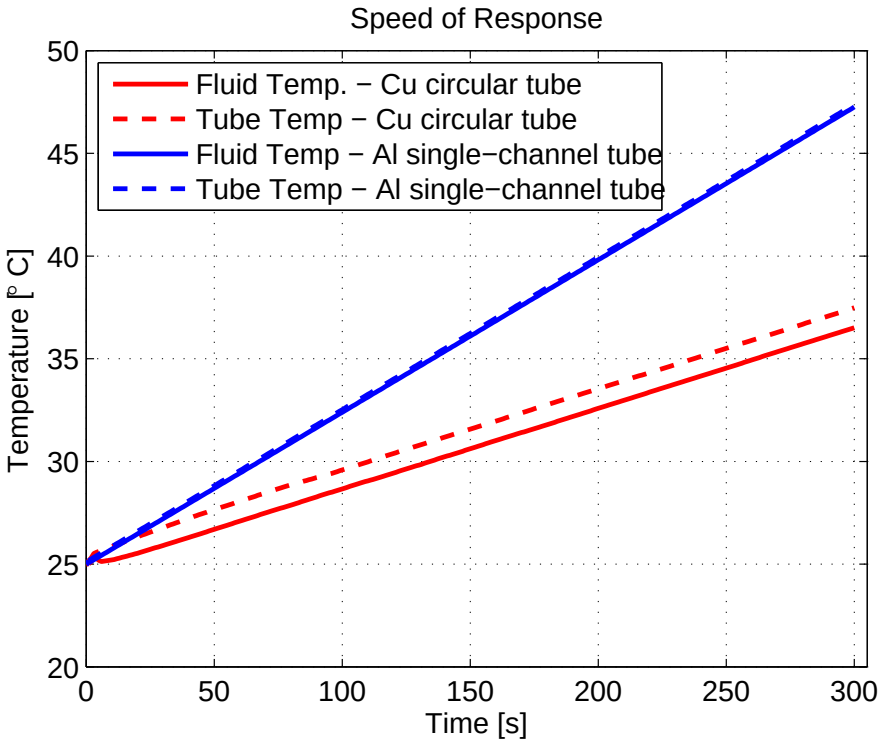

Figure 5.4: Speed of response comparing a single-channel aluminum tube and a circular copper tube.

exchanger also had difficulty reaching higher temperatures. This meant that the effect of heat losses in the system was important. Besides heat losses that occur at the collector and the piping, heat also escaped from the system through the water storage tank. When the working fluid flows into the water storage tank and into the internal heat exchanger coil, convective losses from the coil to the surrounding air in the water storage tank occurred. As seen in Figure 2.17, bypass valve one can allow the working fluid to divert from entering the water storage tank.

However, closing the bypass valve only made a slight improvement to the performance so heat losses were still significant. The next step to reduce heat losses was to remove the water storage tank. It was plausible that even if the bypass valve is closed, heat losses can occur by conduction at the bypass valve to the water inside the storage tank. After the removal of the water storage tank, there was a significant reduction in heat losses, and temperatures at the inlet and outlet of the collector were reading past 100 °C, temperatures at the inlet of the steam heat exchanger and at the flow meter were reading above 90 °C, and steam was generated through the steam generator.

An additional modification to the original system included adding a sheet of copper underneath the surface of the minichannel tubes. This increase surface area of heat absorbed to the working fluid. Discussion of experimental results taken after this adjustment to the copper minichannel solar collector system is presented in the next subsection.

5.2.2 Performance of copper minichannel solar collector

Due to the amount of time between fabrication and adjustments made to the copper minichannel solar collector and the completion of this thesis, experimental performance tests were only conducted for a couple months. Unlike the aluminum minichannel solar collector that operates at lower temperatures, the copper minichannel solar collector operates at higher temperatures, and therefore supervision was needed at all times, and availability of the lab group was limited reducing the number of days for testing.

Figure 5.6 represents an experiment and performance test on July 29, 2015, a clear and sunny day with ambient temperatures reaching as high as 36.9 °C (thick solid purple line). The experiment ran from 8:30 AM to 1:26 PM. From the figure, it can be seen that the collector inlet ($T_{col,in}$) and outlet ($T_{col,out}$) temperatures (dashed blue line and solid red line, respectively) started at 31.5 and 32 °C, respectively. After two hours, the collector inlet and outlet temperatures reached over 100 °C, and stayed above 100 °C until the end of the experiment. The highest point the collector temperatures reached at the inlet and outlet was 107.5 and 107.9 ° C, respectively, which can be seen around 12:51 PM. The solar irradiance remained within the range of 565.7 to 787.50 W/m^2 during the test (dash-dot black line).

In the beginning, the valve of the steam heat exchanger outlet was shut but left with a slight opening. As the steam outlet temperature begun to increase, the valve of the steam heat exchanger outlet was manually opened all the way. Steam was generated as the temperature at the outlet of the steam heat exchanger reached 99 °C seen by the turquoise dashed line. The thermocouple used has an accuracy of ± 2.2 °C in the range of 0 to 1250 °C. This may have prevented the thermocouple from reaching 100 °C. Steam was generated at the steam heat exchanger multiple times during the day as the steam heat exchanger outer shell was refilled with water. It can be seen a couple times as the water was refilled into the steam generator shell when its outlet temperature drops; this occurred approximately at 11:08 AM and 12:07 PM. Figure 5.5 shows low-grade steam generated at the outlet of the steam heat exchanger.

Figure 5.5: Low-grade steam generated at the outlet of the steam heat exchanger.

The short length of the inlet thermocouple and the location far away from the heat exchanger may have caused the temperature readings at the steam heat exchanger inlet and flow meter to read lower temperatures than steam generation at saturation conditions occurring at atmospheric pressure. From Figure 5.6, the temperature at the steam generator inlet ($T_{s,in}$, green dotted line) was in the nineties while the temperatures of the collector inlet and outlet were above 100 °C. The thermocouple at the steam heat exchanger inlet is placed at the valve where the steam heat exchanger is replenished with water from the tap; this location is about 15 *cm* away from the body of the steam heat exchanger where most of the heat

exchange occurs. In addition, the thermocouple is not long enough to read an accurate reading.

The solid yellow line representing the temperature reading at the flow meter (T_{flow}) was also reading lower temperatures than saturation temperature. It was reading in the nineties while the collector inlet and outlet temperatures were reading at least 100 °C. A couple of reasons may cause this. There are heat losses in the piping from the outlet of the collector to the flow meter. In addition, as heat is exchanged in the steam generator, there is a temperature gradient inside the shell. However, even with the heat losses, the average temperature difference of the collector and the temperature at the flow meter is 12.5 °C. Possible causes for low temperature readings at the flow meter are currently being investigated. A probable cause of lower temperature readings may be due to the inaccurate reading of the flow meter device itself. The maximum temperature that the flow meter can read is 100 °C, and errors reading this temperature range is ±2 °C.

Figure 5.7 represents the flow rate during the operation of the experiment. The collector operated between 9.8 to 10.6 L/min during the majority of the experiment. This is the flow rate of the system at low pump speed without any bypass valves opened. The average temperature difference between the inlet and outlet collector was 0.47 °C during a flow rate of 9.8 to 10.6 L/min. More experiments are underway to analyze the effect of the system at various flow rates.

5.2.3 Steam generation

Quantification of steam generation rate was approximated. To calculate the approximated steam generation rate, the amount of water filling the outer shell of the steam heat exchanger was initially recorded by using the rotameter and marking the start and end fill lines on the sight glass as seen in Figure 5.8. The sight glass detects the water level or amount of water in the outer shell. The rotameter reads the rate of water in volume per time entering into the outer shell. By allowing the rotameter to read a constant flow rate and timing the fill to the end mark, the volume of water in the outer shell of the steam heat exchanger can be calculated. Once steam is generated, time is recorded to analyze the time it takes the water level in the sight glass to reach to the starting fill mark. The rate of steam generation can be calculated by dividing the volume of water of the outer shell of the heat exchanger by the time it takes the water level to reach from the end to the start marks of the fill. Then multiply that volumetric flow rate by the density of saturated steam. Several calculations were made and the steam generation rate for the limited testing period of the copper minichannel solar collector was in the range of 2.4 to 2.8 g/min.

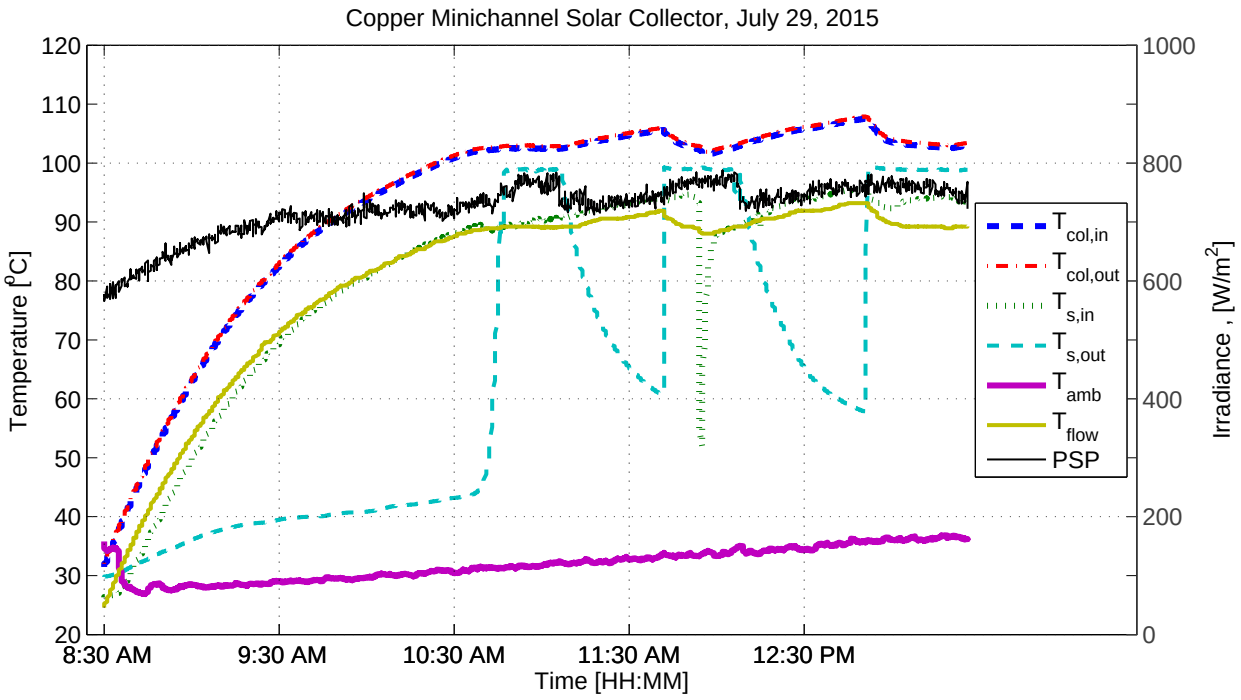

Figure 5.6: Performance of the copper minichannel solar collector in operation on July 29, 2015.

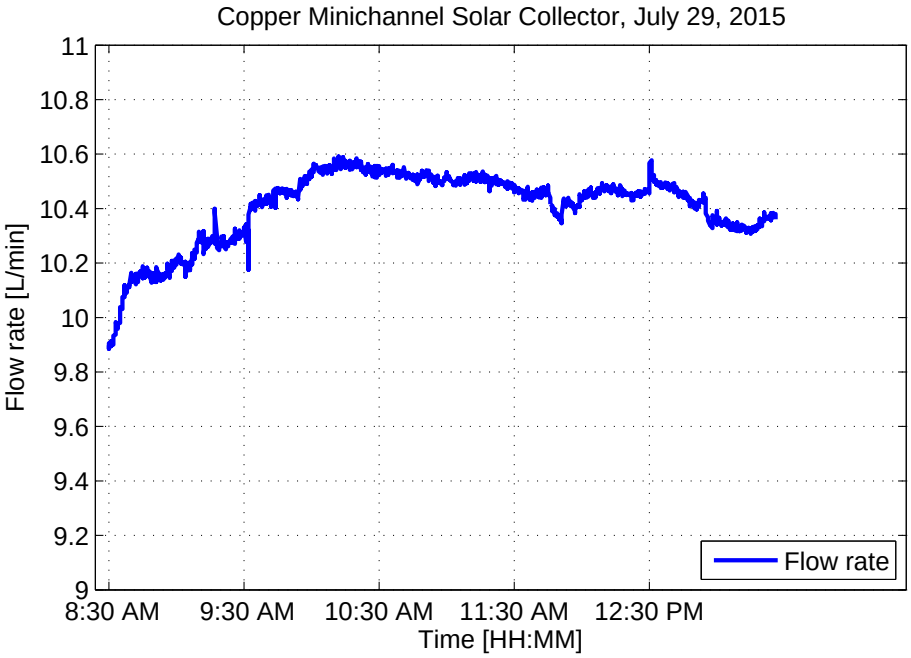

Figure 5.7: Flow rate of the copper minichannel solar collector in operation on July 29, 2015.

5.2.4 Stagnation Temperatures and Thermosyphon Effects

Test results obtained showing effects of the copper minichannel solar collector during stagnation and thermosyphon operating conditions are presented in Figures 5.9 and 5.10. Figure 5.9a shows the performance of the copper minichannel solar collector during stagnation on April 30, 2015. As the flow rate (black line) drops to zero, the spikes in the temperature at the outlet (green dashed line) between 11:00 AM and 12:30 PM shows the collector during stagnation. It can be seen that during stagnation, the temperature at the outlet of the collector can gain as much as 40 °C. For instance, at 11:15 AM the temperature at the outlet of the collector was at 71.8 °C. As the pump was turned off at that time, the flow in the system became stagnant. At around 11:30 AM, the temperature at the outlet of the collector was at 112.1 °C. Figure 5.9b references the solar irradiance during that day with values that ranged from 795 to 860 W/m^2 during stagnation conditions.

The effect of the copper minichannel solar collector in thermosyphon mode can be seen in Figure 5.10. The copper minichannel solar collector was able to self-pump and circulate the working fluid through the collector without the use of a pump. In Figure 5.10a at around 12:50 PM, the pump is turned off resulting in a decrease of flow rate (black line). However, due to the temperature difference between the outlet of the collector and the water in the jacket of the steam heat

Figure 5.8: Tracking the steam generation rate by marking the sight glass with the start and end fill lines, and timing the steam generation as the water level at the end line drops to the start line.

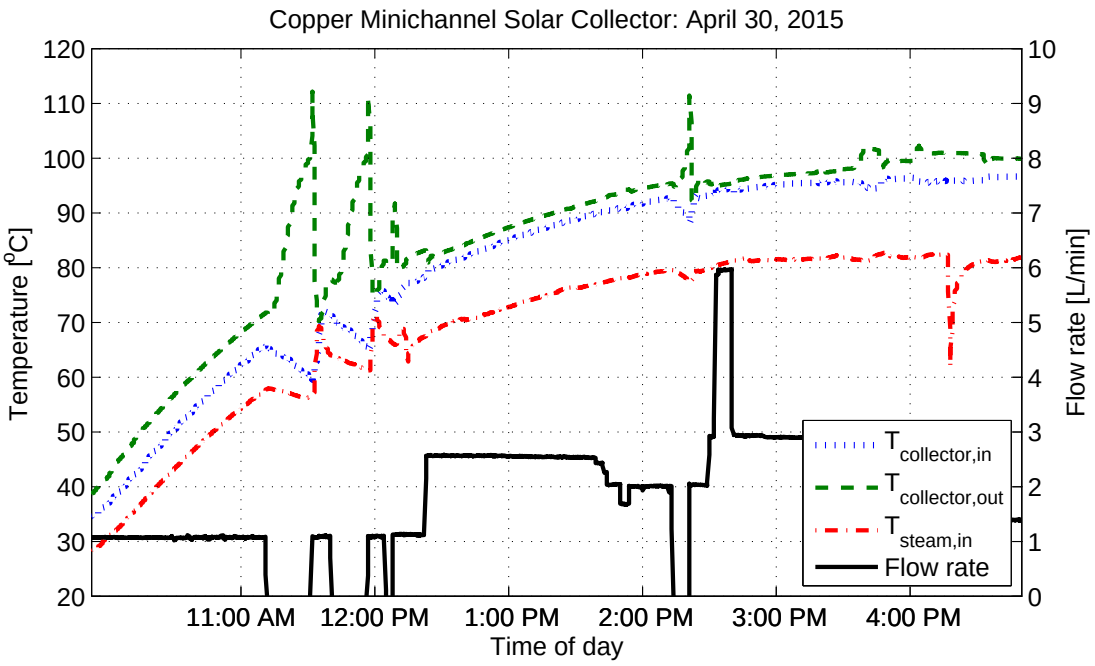

(a)

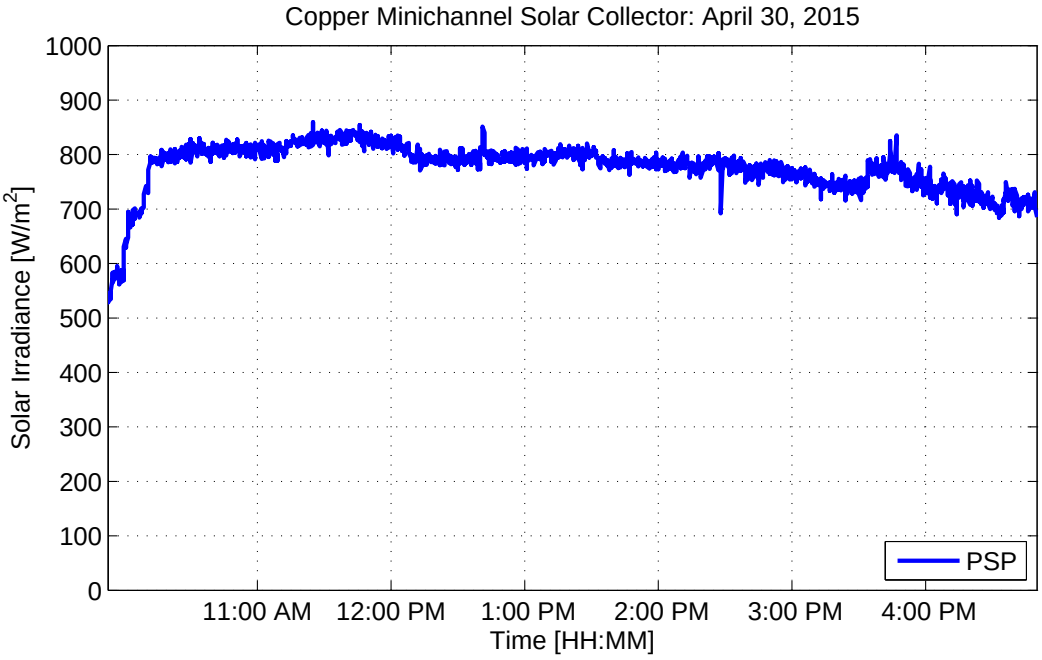

(b)

Figure 5.9: Effect of the copper minichannel solar collector during stagnation on April 30, 2015 showing: (a) temperature and flow rate versus time of the day, and (b) solar irradiance versus time of the day.

exchanger, the collector started to self-pump the working fluid through the system. Instead of the flow rate dropping to zero, the flow rate remained at 1.3 L/min. At that instance, it can be seen that the temperature at the inlet of the collector decreases rapidly. The system was self-pumping from 12:40 PM to 1:10 PM. Then the pump is turned back on represented by the increase of flow rate and an oscillation of the inlet and outlet collector temperatures. Figure 5.10a shows the solar irradiance for that day. Between 12:40 PM and 1:10 PM, an oscillation in the value of the solar irradiance appeared when the pump was turned off. The cause of the problem was investigated but not determined. The connections of the sensor wires to the data acquisition system were checked and reconnected. The problem did not appear again in subsequent tests.

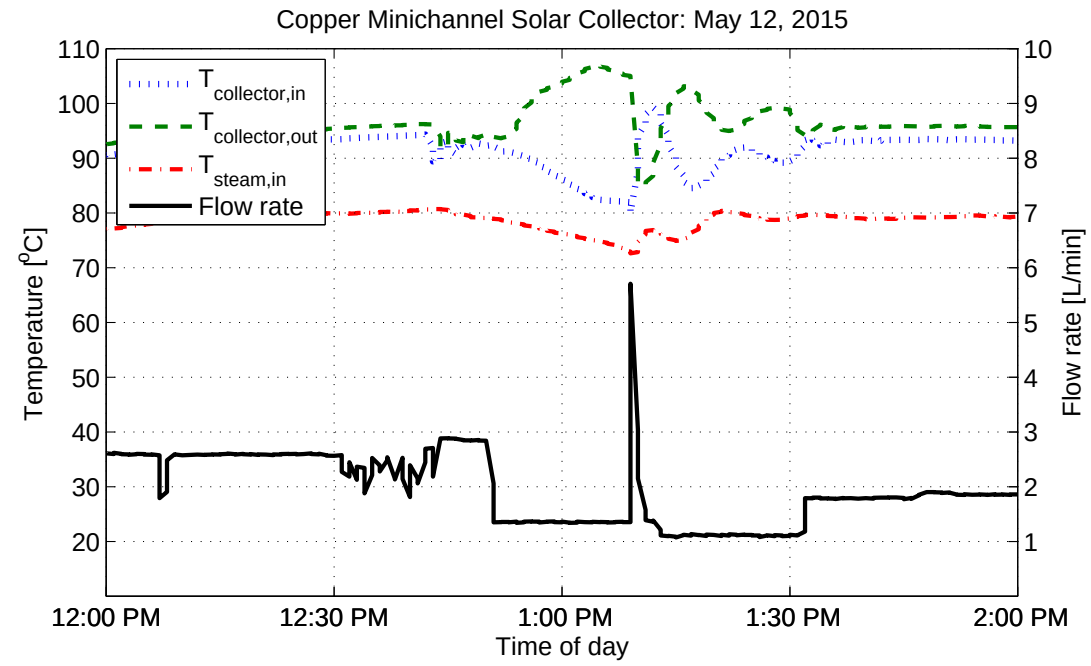

(a)

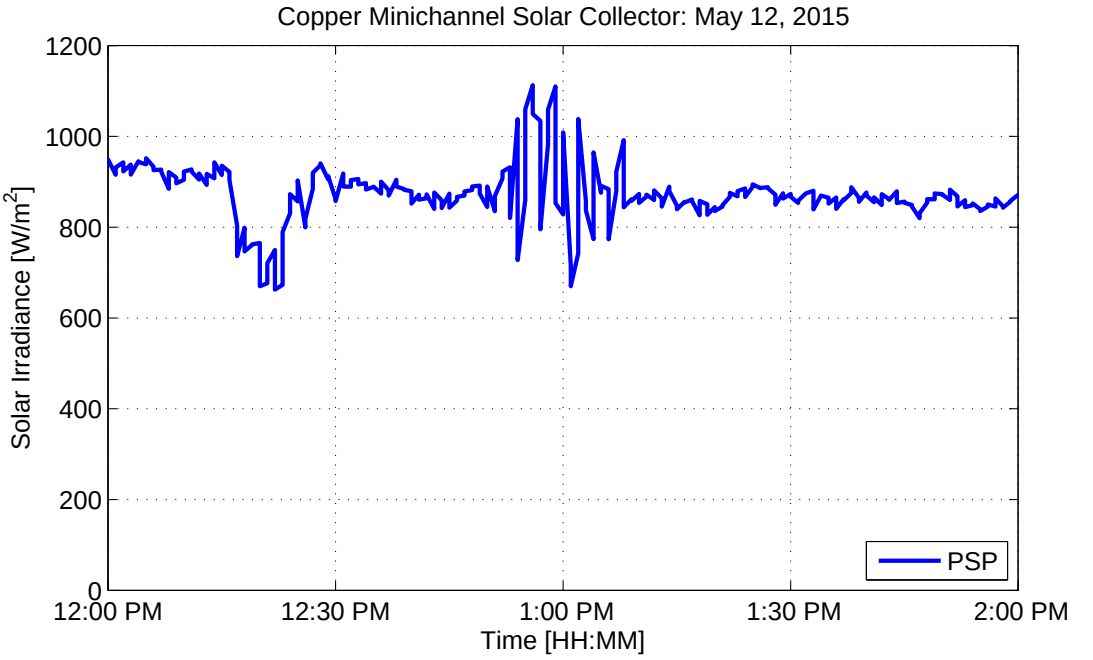

(b)

Figure 5.10: Effect of the copper minichannel solar collector experiencing thermosyphon within the system on May 12, 2015 showing: (a) temperature and flow rate versus time of the day, and (b) solar irradiance versus time of the day.

Chapter 6

ECONOMIC AND MARKET ANALYSIS

As reported in 2012 by Hudon et al., the United States' energy consumption from residential and commercial sectors accounted for approximately 40% of the country's total primary energy consumption [85]. Within a typical household, 20% of the total energy consumption accounts for water heating [86]. Water heating technology has come a long way from heating water in a pot over an open fire to gas-powered water heater. The technology comes in different forms depending on which energy source is being utilized. Therefore costs such as installation, maintenance and operation can vary. According to a technical report by *Newport Partners*, water heating systems that utilize electricity in water heater have the highest energy consumed and highest operating costs compared to other technologies [5]. Other types of systems can have lower energy consumption and operating costs by utilizing other forms of fuel such as natural gas and propane.

Solar thermal energy for water heating has been used since the late 19th century. One of the first solar water heater collectors was invented by C. M. Kemp and documented as a patent for "apparatus for utilizing the sun's rays" [6]. During the past decade, solar thermal water heaters have grown in popularity experienced from large studies on copper flat-plate and evacuated tubes, which have become the most popular solar thermal designs. Solar thermal systems have proved to be capable of providing low to medium temperature heat in a sustainable way. Common applications using solar thermal energy include pool, space and water heating. One of the most active area of research in solar thermal systems deals with the effective heat transfer described in the sun to the working fluid.

A prototype of an aluminum-based minichannel solar water heater was designed, built and installed at the Castle facilities of University of California-Merced since February 2012. A conventional copper flat-plate collector with similar dimensions was also built and installed as a controlled variable to compare and analyze the performance of the aluminum minichannel solar water heater. Data were collected on a daily basis and analyzed to asses the performance of both collectors. Based on the more effective heat transfer design on the aluminum minichannel tubes, the aluminum minichannel solar water heater system was shown to outperform the copper flat-plate solar water heater as shown in the results from Chapter 4.

Based on the remarkable performance results of aluminum minichannel tubes used in a solar collector water heater, it is inferred that there is potential marketability and interest for this technology. Prior to considering commercialization, a study of market size potential is required to understand the marketability of this new technology. If the market size and interest is strong and promising, changes in the design will be required to optimize the technology, as well as, the manufacturing process and costs for mass production.

In this chapter, the market for solar thermal technologies in California and the U.S. is studied, as well as, discussing what is hindering and what can be done to strengthen the market. Costs of conventional solar thermal systems are researched and estimated. The cost of producing the aluminum minichannel solar collector prototype is approximated to compare with costs of conventional solar collectors. Estimated cost of material for mass production of both the aluminum minichannel solar collector is calculated. Although more analysis and study is needed for the copper minichannel solar collector before considering commercialization, cost of material for mass production of the copper minichannel solar collector is estimated as well.

6.1 Market Size: Overlook of acceptance and usage of solar thermal technologies in California and the U.S.

Solar technology, whether photovoltaic or thermal, has been gaining awareness and popularity throughout the years. According to the *Solar Energy Industries Association (SEIA)*, solar water heating installation capacity has increased and is steadily growing from 2006 to 2010. As seen in Figure 6.1, 2.4 million square feet of solar water collectors were sold in 2010, an increase of 5% since the previous year [87].

In addition in order to gain more acceptance and interest, some states are promoting and encouraging solar water heating systems and other solar thermal technologies in the residential and commercial sectors by offering incentives such as rebates. Some of the more popular states offering rebates are Arizona, California, Hawaii, North Carolina, Massachusetts, Pennsylvania, Florida and Oregon [88, 89]. Other states that do not offer rebates, however, offer other sorts of incentives such as savings, tax credits and loan programs. More information about incentives like rebates, tax credits and savings in any particular state can found be in [90, 91].

Comparing the performance and results between the two collectors, the aluminum based minichannel solar water heater can be a potential replacement for the copper flat-plate solar water heater and its market. The market size increases when private companies and state governments promote and market solar thermal energy systems in the residential and commercial sector with tax credits and incentives. In Table 6.1, according to the *U.S. Solar Market Insight Report: 2011 Solar Heating and Cooling Year-In-Review*, the market in 2011 has shown that 40,839 square feet

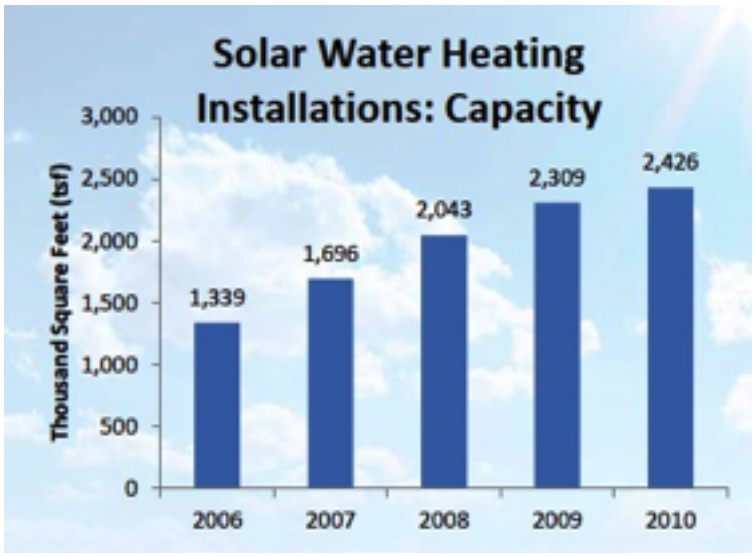

Figure 6.1: Steady growth of solar water heating systems capacity installation by year from 2006 to 2010 in the United States [87].

of solar water heating collectors were installed in the residential sector in California; in the non-residential sector, such as commercial applications, 97,283 square feet of solar water heating collectors were installed. This gives in California a total of 138,122 square feet of solar water heating collectors installed in 2011 [92]. According to the technical report, these numbers were collected from primarily incentive program administrators, utility companies, manufacturers and installers that chose to participate.

Some of the issues that have been delaying the growth of solar water heater system installations has been the lack of awareness of the technology, as well as, the potential incentives, tax credits and savings offered by state and federal government. However, a huge hinder in growth of solar water heating system installations has been the low cost of natural gas especially in California. In the 2007, Assembly Bill (AB) 1470 of California assumed that the price of natural gas was to be increased from 2010 to 2017. However, due to unforeseen circumstances at that time like the economic crisis of October 2008 and the introduction of new drilling techniques, prices of natural gas have plundered since 2008, as seen in Figure 6.2 and 6.3 in the United States and California, respectively [88]. Due to the reduction of natural gas prices, the growth of solar thermal energy systems has been stagnant.

6.2 Estimated costs

In the following subsections, estimated costs of conventional solar thermal systems on residential and commercial buildings in California and the United States

Table 6.1: Solar water heating systems installed capacity in 2011 in square feet. [92].

	Residential	Non-Residential	Total
AZ	135,607	14,620	150,227
CA	40,839	97,283	138,122
CT	5,374	-	5,374
DC	-	25,000	25,000
DE	269	128	397
HI	138,533	-	138,533
IL	1,157	845	2,002
MA	10,905	16,628	27,533
MD	15,596	160	15,756
ME	16,559	-	16,559
MN	2,460	1,901	4,361
NC	3,114	126,195	129,309
NH	14,032	2,498	16,529
NY	7,600	-	7,600
OR	4,099	9,450	13,549
PA	15,359	10,080	25,439
TX	3,075	360	3,435
VT	17,378	10,990	28,368
WI	16,976	-	16,976
Total	448,930	316,138	635,760

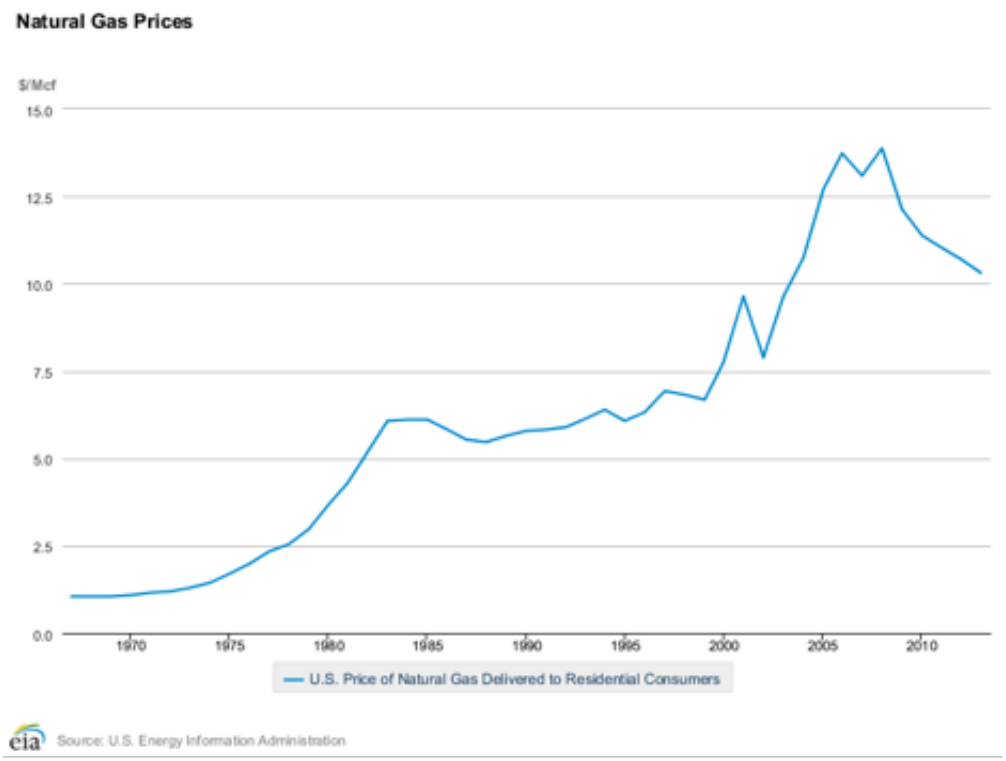

Figure 6.2: Annual natural gas prices in the United States ($/Mcf) [93].

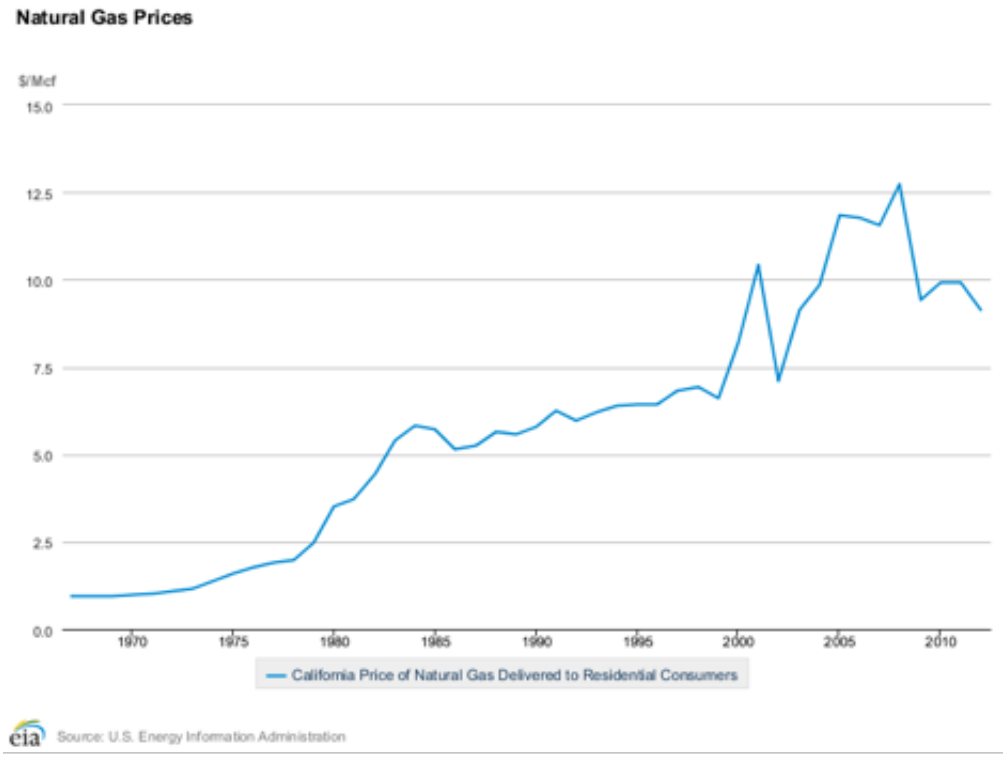

Figure 6.3: Annual natural gas prices in California ($/Mcf) [93].

are presented based on data analyzed from a survey collected. These estimated costs are compared with the costs of the prototype aluminum minichannel solar collector. In addition, the estimated costs of mass production of the aluminum and copper minichannel solar collectors are calculated and compared.

6.2.1 Conventional solar thermal systems on residential and commercial buildings in California and the U.S.

The most popular solar water heating collectors utilized in the United States are flat-plate collectors and evacuated tube collectors. Depending on the size of a residential dwelling or non-residential building and the type of collectors, solar water heating systems will vary in cost. Literature and data of solar water heater installation size and costs are limited in availability. However, a collaborative effort from *SEIA Policy and Research Divsion* and *GTM Research Solar Analysts* were able to obtain data from a survey of installation sizes and costs in residential and non-residential sectors in the United States in 2011 [92]. Data were gathered from installers, solar heating and cooling manufacturers, and incentive program administrators who chose to participate and share their data. Data of average costs of installation and installation sizes in residential and non-residential, which include flat-plate and evacuated tube collectors, are shown in Tables 6.2 and 6.3. In Table 6.2, SEIA and GTM reported in 2011 that the average cost to install a solar water heating system in a residential dwelling in California was $8,364.32; Nationally, the average cost to install a solar water heating system is $9,235.45. The average costs includes the system, installation design and labor; the system consists of the the collectors, recommended equipment such as the water storage tank, pump, controller, piping, etc.

In Table 6.3, average installation size of solar water heating systems are displayed. In California, the average installation size is about 48.8 square feet in the residential sector. Based on the average cost of a system installed in California mentioned previously, this leads to $171.40 per square foot. On the other hand, national average installation size is 50.2 square feet on residential housings. The number may be higher due to the amount of collectors required in states with cooler climates and longer winter seasons. Based on the costs of an average solar water heater system nationally, this leads to $198.22 per square foot.

Considering commercial and the non-residential sector, from Tables 6.2 and 6.3, *SEIA* and *GTM Research* reported an average costs of a solar water heating system of $116,953.90 in California with average installation size of 1,069 square feet. This gives a calculated average of $109.40 per square foot. On the other hand, nationally an average system costs $82,165.14 with an average installation size of 530 square feet, or $111.78 per square foot.

From the same report by *SEIA* and *GTM Research*, the breakdown costs of a solar water heating system installed on a residential housing led to approximately

Table 6.2: Average price of solar water heater systems installed in 2011 in various states for residential and non-residential sectors [92].

	Residential $/sq. ft.	Non-Residential $/sq. ft.	Average Total Cost Residential	Average Total Cost Non-Residential
AZ	$232.82	$109.86	$8,847.24	$59,544.12
CA	$171.40	$109.40	$8,364.32	$116,953.90
CT	$138.40	$103.23	$11,830.71	$85,733.71
DE	$255.79	$234.20	$11,446.67	$29,978.00
MA	$156.31	$124.98	$11,371.14	$106,482.96
MD	$175.45	$117.48	$10,246.28	$18,796.80
MN	$157.91	$136.06	$11,416.89	$28,749.48
TX	$138.71	$141.67	$6,463.89	$25,500.60
VT	$152.55	$112.29	$10,144.58	$28,046.67
WI	$115.63	-	$15,575.36	-
National Average	$198.22	$111.78	$9,235.45	$82,165.14

Table 6.3: Average size of solar water heater systems installed in 2011 in various states for residential and non-residential sectors in square feet. [92].

	Residential	Non-Residential
AZ	38.0	542.0
CA	48.8	1069.0
CT	85.5	830.5
DC	-	1,000.0
DE	44.8	128.0
MA	72.7	852.0
MD	58.4	160.0
MN	72.3	211.3
TX	46.6	180.0
VT	66.5	249.8
WI	134.7	-
National Average	50.2	530.0

30% cost for the collectors themselves, 35% for other equipment (piping, tank, pump, etc.), 5% for site design, and 30% for the installation labor [92]. In the commercial and non-residential sector, the same breakdown costs were approximately 35% for the collectors, 18% for the other equipment, 5% for the site design and 42% for the installation labor. These numbers are shown in a chart in Figure 6.4.

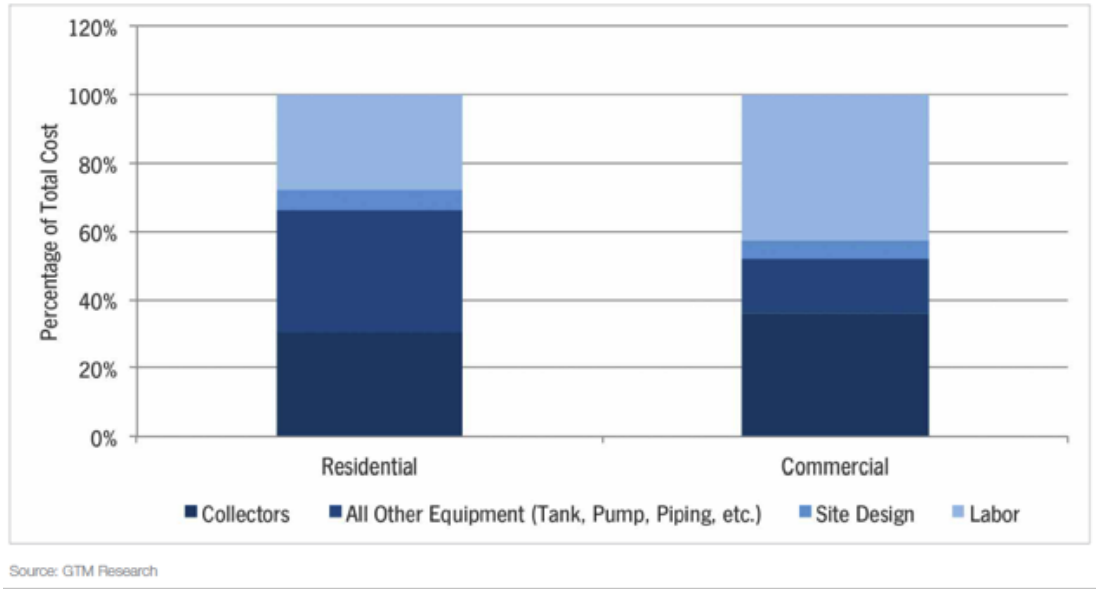

Figure 6.4: Solar water heating system breakdown costs in residential and non-residential sectors: collectors, other equipment, site design and labor. [92].

It was difficult to find a comprehensive research or resource of average solar water heating collector costs. In addition, many solar heating and cooling businesses are hesitant to share and display up-to-date solar collector costs on the Internet. Many require to call-in and request a quote. However, with the information share previously from the report by *SEIA* and *GTM Research*, the estimated cost of today's conventional solar thermal collectors, such as flat-plate and evacuated tube collectors, can be approximated. Using the information gathered from the system breakdown costs and the average price in California to install a solar water heating system in residential sector, the approximated calculated costs of a conventional solar thermal collector is $51.42 per square foot ($553.50 per square meter); in California commercial sector, the approximated costs of a conventional solar thermal collector is $38.29 per square foot ($412.16 per square meter). Furthermore, the national average costs of a conventional solar thermal collector in the residential and commercial sectors, respectively, are $59.47 per square foot ($640.11 per square meter) and $39.12 per square foot ($421.13 per square meter). A summary of this information is shown in Table 6.4.

Table 6.4: Average costs of conventional solar thermal collectors in California and nationally for residential and commerical sectors.

	Residential	Commercial
California	\$51.42/sq. ft	\$38.29/sq. ft
	(\$553.50/sq. meters)	(\$412.16/sq. meters)
National	\$59.47/sq. ft	\$39.12/sq. ft
	(\$640.11/sq. meters)	(\$421.13/sq. meters)

6.2.2 Prototype costs of aluminum minichannel solar collector

The approximate total cost of the aluminum minichannel solar collector prototype is shown in Table 6.5 below. This approximate price is for a 10 feet by 4 feet collector, or 3.72 square meters.

Table 6.5: Approximate cost of the aluminum minichannel solar collector prototype breakdown.

Item/Material	Quantity	Cost
Aluminum minichannel tubes (Norsk Hydro ASA)	11	\$440*
Headers, schedule 40 aluminum pipes	2	\$28
Collector frame and glass (SunEarth, Inc.)	1	\$500
TIG Welding	-	\$1056
	Total	\$2024
	\$/sq. ft	\$50.60
	\$/sq. m	*\$544.67*

*Prototype price

Comparing the projected costs per unit are of the prototype aluminum minichannel collector to the estimated costs of a conventional solar collectors, such as flat-plate and evacuated tube collectors, in section 6.2.1, savings could be made in the residential sector. In section 6.2.1, it was estimated that conventional collectors itself calculated to cost approximately between \$51.42 to \$59.47 per square foot in the residential sector. This gives a difference of \$0.82 to \$8.87 savings per square foot switching conventional solar collectors to aluminum minichannel collectors using residential pricing.

Generally in commercial sites, the installation size is larger than residential sites therefore requiring more collectors for installation. This can be seen in Table 6.3. Table 6.3 shows nationally that commercial installations are at least ten times larger than residential installations. Usually costs of collectors can be lower if more quantity are needed as shown in the commercial column in Table 6.4. Although there are no savings resulted from comparing the costs of the prototype aluminum

minichannel solar collector and conventional solar collectors using prices in the commercial sector, the emphasis is that the cost of a prototype would be higher than if the aluminum minichannel solar collectors are mass produced.

6.2.3 Estimated material costs of aluminum and copper minichannel collectors for mass production

Mass production of the aluminum minichannel collector is very much possible due to the extensive use of extruded aluminum minichannel tubes. Considering the automotive, HVAC and electronics industries that extensively uses extruded minichannel tubes, costs of mass production can be low especially for more common sizes that are produced. Generally, aluminum are purchased by weight. In 2012, it was reported by the *U.S. Geological Survey* that for large volumes or in bulk, aluminum can be purchased for as low as $2.23 per kilogram depending on the current value of aluminum in the market [94]. Assuming the aluminum minichannel tubes are approximated to be $2.23 per kilogram without the refining and extrusion process, the estimated material cost for mass production of the aluminum minichannel solar water heater of the same dimensions$\sim$(10 feet by 4 feet) are shown in Table 6.6. Note that this approximation does not include the extrusion process, manufacture and labor costs.

Table 6.6: Approximated material cost for mass production of the aluminum minichannel solar water heater collector.

Item/Material	Quantity	Cost
Aluminum minichannel tubes ($2.23/kg; each tube is $\sim$0.85 kg)	11	$20.90
Headers, schedule 40 aluminum pipes*	2	$28
Collector frame and glass*	1	$500
	Total	$548.90
	$/sq. ft	$13.72
	$/sq. m	*$147.69*

*Note: Costs per unit can be lower if purchased in bulk quantities.

The copper minichannel collectors can be estimated as well. Again according to the *U.S. Geological Survey*, the prices of copper in 2012 was averaged to $8.10 per kilogram without the refining and extrusion process. If the copper minichannel prototype collector was to be mass produced, the material costs are shown in Table 6.7 below. The copper minichannel prototype collector is smaller$\sim$(6.4 ft by 3.4 ft) than the aluminum minichannel collector. Again, the material costs of mass producing the prototype also does not include the extrusion process, manufacture and labor costs as this information is difficult to find and assess fairly.

Table 6.7: Approximated material costs for mass production of the copper minichannel solar water heater collector.

Item/Material	Quantity	Cost
Copper minichannel tubes ($8.10/kg; each tube is 0.23 kg)	20	$37.26
Headers, Type L copper pipes*	2	$38
Collector frame and glass*	1	$200
	Total	$275.26
	$/sq. ft	$12.94
	$/sq. m	*$139.29*

*Note: Costs per unit can be lower if purchased in bulk quantities.

In the material costs of mass producing either of the minichannel collectors, it is expected that the costs for the headers and the collectors can be reduced if bulk amounts were purchased. This will depend on the supplier of the collector frames and glasses, and pipes used for the headers. In addition, due to the popularity of vacuum brazing used in the manufacturing process of conventional copper flat-plate solar collectors as well as radiators, this method of metal-joining can also be applied to both the manufacturing process of copper and aluminum minichannel solar collectors.

Chapter 7

CONCLUSIONS AND FUTURE WORK

Novel solar thermal collectors based on minichannel tubes with no concentration for low to medium temperature applications were introduced. The design processes and assemblies of the aluminum and copper minichannel solar collectors were described. The performance of the minichannel solar collectors was analyzed with experimental results. The aluminum minichannel solar collector was tested for over a year and compared alongside to copper flat-plate collector. The copper minichannel solar collector was tested for a couple months in order to obtain preliminary results. Mathematical models were created as a tool to predict the performance of the collectors under various operating conditions and parameters. The mathematical models simulated the performances of the minichannel solar collectors under single or two-phase flow. The single-phase mathematical model was compared to experimental results. The two-phase mathematical model was compared to single-phase simulations to analyze performances under these operating conditions. The economics of solar thermal collectors, the market potential, and the costs of mass production of the minichannel solar collectors were also discussed.

The novel minichannel solar collector design uses minichannel tubes as the absorber, eliminating the need for an absorber fin attached to the tubes such as in the conventional copper flat-plate collector. This is an advantage as the working fluid is directly in contact with the tube walls that absorbs energy from the sun. The thermal resistance of the copper flat-plate collector is an order magnitude larger than the thermal resistance of the aluminum minichannel solar collector.

During summer conditions, the aluminum minichannel solar water heater was able to usually heat up the water inside a 300 L (80 *gallons*) water storage tank up to 55 °C approximately an hour quicker than the copper flat-plate solar collector. In Spring test conditions, the aluminum minichannel solar collector generated a net gain of 2.3 °C in the water storage tank in comparison to the copper flat-plate collector. This additional energy obtained from the the net gain was calculated to be additional 2,898 kJ or 805 Wh.

A speed of response simulation shows that due to the minichannel tube design, the working fluid in the aluminum minichannel solar collector can increase the

working fluid temperatures quicker than the copper flat-plate collector. The thermal inertia of the aluminum minichannel and copper flat-plate solar collector are respectively, 22,492.7 and 34,438.3 $Jm^{-2}K^{-1}s^{-1/2}$.

The copper minichannel solar collector was only tested for a couple of months due to time constraints of completing this thesis. However, preliminary results indicate that with a steam generator heat exchanger, steam can be produced using the copper minichannel solar collector with temperatures up to 105 °C for solar irradiances near 800 W/m^2. Data obtained during the summer showed that the copper minichannel tube collector increased the temperature of the working fluid in the collector to a value over 100 °C within two hours of operation, and it is capable of staying over 100 °C until late afternoon.

Mathematical models were created as predictive tools to simulate the minichannel solar collectors under different operating conditions. The single-phase mathematical model was validated with experimental data from the aluminum minichannel solar collector. The single-phase mathematical model had good agreement with the aluminum minichannel solar collector during steady-state condition.

For two-phase flow, various pressure drop and heat transfer coefficient correlations were analyzed to solve the coupled mathematical heat transfer problem. After the correlations were validated and compared against experimental data obtained from the literature, the best pressure drop and heat transfer coefficient correlation were implemented in the minichannel solar collector mathematical model to predict performances of the collectors under two-phase flow. Muller-Steinhagen and Heck correlation [1] pressure drop correlation and Odeh et al. [2] heat transfer correlation were chosen to represent the copper minichannel solar collector. Although the two-phase mathematical model could not be validated with experimental data during this thesis, simulations that compared the copper minichannel solar collector during single and two-phase flow were generated. The simulated results show that efficiencies are higher during single-phase temperatures due to the lower heat losses even though the internal heat transfer coefficient of the working fluid is lower than in two-phase flow conditions. However, efficiencies are not significantly lower during two-phase flow in comparison to single-phase flow temperatures close to saturation conditions. The range of efficiency difference between operating at a single-phase flow inlet temperature of 90 °C and a two-phase flow inlet temperature between 100 and 100 °C is 3% to 10% depending on the solar irradiance.

The solar thermal market was researched and while solar thermal technology in other countries such as Finland and China is gaining in popularity, the solar thermal market in the United States is slow. One reason is due to the low cost of natural gas. The other reason is that the technology is not properly marketed and citizens are not fully aware of this technology. While rebates and incentives offered by the government can help increase the solar thermal market, there is very little awareness of them. Promotion and advertisement contributions from both the

government and businesses are required to gain more awareness and popularity in solar thermal technology.

In terms of the marketability of the minichannel solar collectors, the aluminum minichannel solar collector has the potential to compete with the copper flat-plate solar collector due to the experimental results conducted over a year and the lower costs of aluminum in comparison to copper. While it costs conventional solar thermal collector approximately $421.24 to $640.11 per square meter, it was calculated that the materials to build an aluminum minichannel solar collector was $147.69 per square meter if mass produced. However, the cost of extrusion, manufacture and labor costs were not included.

7.1 Future Work

There are many possible areas for future work and research. One possible area is improving the method of quantifying the amount of steam generated from the steam heat exchanger at the copper minichannel solar collector test stand. This would provide more information about the copper minichannel solar collector such as the rate of steam produced can be better quantified. Accordingly, this would aid in determining the required size for specific applications requiring steam generation.

Second area for future work is combining the single and two-phase flow mathematical models and adding subdivisions to the mathematical model. This will allow a predictive tool to accurately provide the performance of the copper minichannel solar collector in two-phase flow operating conditions. In addition, the subdivisions would provide more accuracy in determining the temperature of the fluid or steam quality within the length of the copper minichannel solar collector.

Another possible area for future work is studying two-phase flow in minichannel tube configurations, and developing more accurate pressure drop and heat transfer coefficient correlations applicable to minichannel tube configurations using various working fluid types. Although there is a large database of literature regarding two-phase flow in various shape single tubes and small diameter tubes, the database of literature is smaller regarding studying two-phase flow in minichannel tubes. As minichannel tubes are gaining in popularity due to their effectiveness in heat transfer such in HVAC and electronics cooling industries, accuracy is necessary when developing computational tools to reduce costs.

Finally, another important area of future research relates to the use of minichannel tubes in evacuated tube solar collectors. The improved heat transfer characteristics of this design can increase thermal efficiency at high operating temperatures when convective losses are eliminated.

As research is continued and more awareness is gained to this novel type of solar thermal collector, minichannel tube solar collectors can potentially provide applications to many fields. For instance, this type of collectors can be used in

space heating and cooling, as well as, residential water heating. For medium temperature or steam generation, the copper minichannel solar collector can be used in applications such in food processing, refrigeration or HVAC.

BIBLIOGRAPHY

[1] H. Müller-Steinhagen, K. Heck, A simple friction pressure drop correlation for two-phase flow in pipes, Chemical Engineering and Processing: Process Intensification 20 (6) (1986) 297–308.

[2] S. Odeh, G. Morrison, M. Behnia, Modelling of parabolic trough direct steam generation solar collectors, Solar energy 62 (6) (1998) 395–406.

[3] Heating and cooling no longer majority of u.s. home energy use, Tech. rep., U.S. Energy Information Administration (EIA), Washington, D.C., website accessed on May 29, 2014 and available at `http://www.eia.gov/todayinenergy/detail.cfm?id=10271` (2009).

[4] J. B. Maguire, A parametric analysis of residential water heaters, Master's thesis, University of Colorado (2012).

[5] NewportPartners, Comparing Residential Water Heaters for Energy Use, Economics and Emissions, Tech. rep., Propane Education and Research Council, Davidsonville, MD (2011).

[6] C. M. Kemp, Apparatus for utilizing the sun's rays for heating water, US Patent 451,384 (Apr. 28 1891).

[7] Y. Tian, C. Y. Zhao, A review of solar collectors and thermal energy storage in solar thermal applications, Applied Energy 104 (2013) 538–553.

[8] J. A. Duffie, W. A. Beckman, Solar Engineering of Thermal Processes, John Wiley & Sons Inc, 2006.

[9] L. M. Ayompe, A. Duffy, Thermal performance analysis of a solar water heating system with heat pipe evacuated tube collector using data from a field trial, Solar Energy 90 (2013) 17–28.

[10] A. Rabl, J. O'Gallager, R. Winston, Design and test of non-evacuated solar collectors with compound parabolic concentrators, Solar Energy 25 (1980) 335–351.

[11] R. Shukla, K. Sumanthy, P. Erickson, J. Gong, Recent advances in the solar water heating systems: A review, Renewable and Sustainable Energy Reviews 19 (2013) 173–190.

[12] F. Jafarkazemi, E. Ahmadifard, Energetic and exergetic evaluation of flat plate solar collectors, Renewable Energy 56 (2013) 55–63.

[13] W. Liu, J. Davidson, S. Mantell, Thermal analysis of polymer heat exchangers for solar water heating: a case study, Journal of solar energy engineering 122 (2) (2000) 84–91.

[14] R. Liang, L. Ma, J. Zhang, D. Zhao, Theoretical and experimental investigation of the filled-type evacuated tube solar collector with u tube, Solar Energy 85 (2011) 1735–1744.

[15] L. Ma, Z. Lu, J. Zhang, R. Liang, Thermal performance analysis of the glass evacuated tube solar collector with u-tube, Building and Environment 45 (2010) 1959–1967. doi:doi:10.1016/j.buildenv.2010.01.015.

[16] Y. Kim, T. Seo, Thermal performances comparisons of the glass evacuated tube solar collectors with shapes of absorber tube, Renewable Energy 32 (5) (2007) 772–795.

[17] L. J. Shah, S. Furbo, Vertical evacuated tubular-collectors utilizing solar radiation from all directions, Applied energy 78 (4) (2004) 371–395.

[18] M. Thirugnanasambandam, S. Iniyan, R. Goic, A review of solar thermal technologies, Renewable and Sustainable Energy Reviews 14 (1) (2010) 312 – 322.

[19] T. Chow, A review on photovoltaic/thermal hybrid solar technology, Applied Energy 87 (2) (2010) 365 – 379.

[20] G. Diaz, Performance analysis and design optimization of a mini-channel evacuated-tube solar collector, in: Proceedings of ASME IMECE 2008, Paper # IMECE2008-67858, Boston, MA, 2008, pp. 1–7.

[21] N. Sharma, G. Diaz, Minichannel tube solar collector, US patent US 2011/0186043 A1 (August 2011).

[22] N. Sharma, G. Diaz, Performance model of a novel evacuated tube solar collector based on minichannels, Solar Energy 85 (2011) 881–890. doi:doi:10.1016/j.solener.2011.02.001.

[23] M. K. Mansour, Thermal analysis of novel minichannel-based solar flat-plate collector, Energy 60 (2013) 333–343.

[24] M. E. Steinke, S. G. Kandlikar, Single-phase heat transfer enhancements techniques in microchannel and minichannel flows, in: Proceedings of Microchannels and Minichannels ASME Conference, ASME, 2004, pp. 141–148, iCMM2044-2328.

[25] R. Yun, Y. Kim, C. Park, Numerical analysis on a microchannel evaporator designed for co_2 air conditioning systems, Applied Thermal Engineering 27 (2007) 1320–1326.

[26] N.-H. Kim, S.-P. Han, Distribution of air-water annular flow in a header of a parallel flow heat exchanger, International Journal of Heat and Mass Transfer 51 (2008) 977–992.

[27] A. Robles, V. Duong, A. J. Martin, J. L. Guadarrama, G. Diaz, Aluminum minichannel solar water heater performance under year-round weather conditions, Solar Energy 110 (2014) 356–364.

[28] F. P. Incropera, D. P. DeWitt, Fundamentals of heat and mass transfer, 5th Edition, John Wiley & Sons, 2001.

[29] F. Kraft, Micro-channel tubes and apparatus and method for forming microchannel tubes, CA Patent 2,672,098 (Jul. 30 2013).
URL `https://www.google.com/patents/CA2672098C?cl=en`

[30] EES, Engineering Equation Solver. F-Chart Software. http://www.fchart.com/ees/ (2014).

[31] A. T. Fonseca, Performance assessment of three concentrating solar thermal units designed with xcpc reflectors and evacuated tubes, using an analytical thermal model, Master's thesis, University of California, Merced (2008).

[32] M. Khoukhi, S. Maruyama, Theoretical approach of a flat plate solar collector with clear and low-iron glass covers taking into account the spectral absorption and emission within glass covers layer, Renewable Energy 30 (2005) 1177–1194.

[33] K. G. T. Hollands, T. E. Unny, G. D. Raithby, L. Konicek, Free convection heat transfer across inclined air layers, Trans. ASME J. Heat Transfer 98.

[34] H. M. Mekisso, Comparison of frictional pressure drop correlations for isothermal two-phase horizontal flow, Ph.D. thesis, Oklahoma State University (2013).

[35] J. G. Collier, J. R. Thome, Convective boiling and condensation, Oxford University Press, 1994.

[36] C. E. Brennen, Fundamentals of multiphase flow, Cambridge University Press, 2005.

[37] V. Carey, Liquid Vapor Phase Change Phenomena: An Introduction to the Thermophysics of Vaporization and Condensation Processes in Heat Transfer Equipment, Second Edition, Taylor & Francis, 2007.

[38] D. Steiner, Heat transfer to boiling saturated liquids vdi-wärmeatlas (vdi heat atlas), VDI-Gesellschaft Verfahrenstechnik und Chemieingenieurswesen (GCV), Düsseldorf.

[39] S. Z. Rouhani, E. Axelsson, Calculation of void volume fraction in the subcooled and quality boiling regions, International Journal of Heat and Mass Transfer 13 (2) (1970) 383–393.

[40] M. O. Didi, N. Kattan, J. Thome, Prediction of two-phase pressure gradients of refrigerants in horizontal tubes, International Journal of refrigeration 25 (7) (2002) 935–947.

[41] J. R. Thome, Engineering data book iii, Wolverine Tube Inc.

[42] S. Zivi, Estimation of steady-state steam void-fraction by means of the principle of minimum entropy production, Journal of Heat Transfer 86 (2) (1964) 247–251.

[43] C. Baroczy, Correlation of liquid fraction in two-phase flow with application to liquid metals, Tech. rep., Atomics International. Div. of North American Aviation, Inc., Canoga Park, Calif. (1963).

[44] G. F. Hewitt, Pressure drop, Handbook of Multiphase System. Hemisphere Publishing Corporation, Washington DC (1982) 2–44.

[45] G. Hewitt, Two-phase flow through orifices, valves, bends and other singularities, Proceedings of the Ninth Lecture Series on Two-Phase Flow (1984) 163.

[46] S.-M. Kim, I. Mudawar, Universal approach to predicting two-phase frictional pressure drop for adiabatic and condensing mini/micro-channel flows, International Journal of Heat and Mass Transfer 55 (11) (2012) 3246–3261.

[47] R. Martinelli, L. K. Boelter, T. Taylor, E. Thomsen, E. Morrin, Isothermal pressure drop for two-phase two-component flow in a horizontal pipe, Trans. ASME 66 (2) (1944) 139–151.

[48] Y. Xu, X. Fang, X. Su, Z. Zhou, W. Chen, Evaluation of frictional pressure drop correlations for two-phase flow in pipes, Nuclear Engineering and Design 253 (2012) 86–97.

[49] R. Lockhart, R. Martinelli, Proposed correlation of data for isothermal two-phase, two-component flow in pipes, Chem. Eng. Prog 45 (1) (1949) 39–48.

[50] R. t. Martinelli, D. Nelson, Prediction of pressure drop during forced circulation boiling of water, Trans. Asme 70 (6) (1948) 695–702.

[51] M. M. Awad, Two-phase flow modeling in circular pipes, Ph.D. thesis, Memorial University of Newfoundland (Canada). (2007).

[52] M. E. Ferguson, P. L. Spedding, Measurement and prediction of pressure drop in two-phase flow, Journal of Chemical Technology and Biotechnology 63 (3) (1995) 262–278.

[53] D. Chisholm, A theoretical basis for the lockhart-martinelli correlation for two-phase flow, International Journal of Heat and Mass Transfer 10 (12) (1967) 1767–1778.

[54] H. Blasius, Das ähnlichkeitsgesetz bei reibungsvorgängen in flüssigkeiten, Forschung Ver. deaf. Ing 131 (1913) l–34.

[55] C. Baroczy, Systematic correlation for two-phase pressure drop., in: Chem. Eng. Progr., Symp. Ser., 62: No. 64, 232-49 (1966)., Atomics International, Canoga Park, Calif., 1966.

[56] C. Tribbe, H. Müller-Steinhagen, An evaluation of the performance of phenomenological models for predicting pressure gradient during gas–liquid flow in horizontal pipelines, International Journal of Multiphase Flow 26 (6) (2000) 1019–1036.

[57] K. Mishima, T. Hibiki, Some characteristics of air-water two-phase flow in small diameter vertical tubes, International Journal of Multiphase Flow 22 (4) (1996) 703–712.

[58] L. Sun, K. Mishima, Evaluation analysis of prediction methods for two-phase flow pressure drop in mini-channels, International Journal of Multiphase Flow 35 (1) (2009) 47–54.

[59] E. Jassim, T. Newell, Prediction of two-phase pressure drop and void fraction in microchannels using probabilistic flow regime mapping, International Journal of Heat and Mass Transfer 49 (15) (2006) 2446–2457.

[60] V. G. Nino, P. Hrnjak, T. Newell, Characterization of two-phase flow in microchannels, Tech. rep., Air Conditioning and Refrigeration Center. College of Engineering. University of Illinois at Urbana-Champaign. (2002).

[61] C. Yang, R. Webb, Friction pressure drop of r-12 in small hydraulic diameter extruded aluminum tubes with and without micro-fins, International Journal of Heat and Mass Transfer 39 (4) (1996) 801–809.

[62] L. Cheng, G. Ribatski, J. R. Thome, Two-phase flow patterns and flow-pattern maps: fundamentals and applications, Applied Mechanics Reviews 61 (5) (2008) 050802.

[63] M. Shah, Chart correlation for saturated boiling heat transfer: equations and further study, ASHRAE Trans.;(United States) 88 (CONF-820112-).

[64] S. G. Kandlikar, Heat transfer mechanisms during flow boiling in microchannels, in: ASME 2003 1st International Conference on Microchannels and Minichannels, American Society of Mechanical Engineers, 2003, pp. 33–46.

[65] S. G. Kandlikar, A general correlation for saturated two-phase flow boiling heat transfer inside horizontal and vertical tubes, Journal of heat transfer 112 (1) (1990) 219–228.

[66] K. Gungor, R. Winterton, A general correlation for flow boiling in tubes and annuli, International Journal of Heat and Mass Transfer 29 (3) (1986) 351–358.

[67] K. Gungor, R. Winterton, Simplified general correlation for saturated flow boiling and comparisons of correlations with data, Chemical engineering research & design 65 (2) (1987) 148–156.

[68] J. C. Chen, Correlation for boiling heat transfer to saturated fluids in convective flow, Industrial & Engineering Chemistry Process Design and Development 5 (3) (1966) 322–329.

[69] R. W. Bjorg, G. R. Hall, W. M. Rohsenow, Correlation of forced convection boiling heat transfer data, International Journal of Heat and Mass Transfer 25 (6) (1982) 753–757.

[70] L. Sun, K. Mishima, An evaluation of prediction methods for saturated flow boiling heat transfer in mini-channels, International Journal of Heat and Mass Transfer 52 (23) (2009) 5323–5329.

[71] S. Kandlikar, A model for correlating flow boiling heat transfer in augmented tubes and compact evaporators, Journal of heat transfer 113 (4) (1991) 966–972.

[72] M. M. Shah, A new correlation for heat transfer during boiling flow through pipes, 1976.

[73] A. Cavallini, G. Censi, D. Del Col, L. Doretti, G. Longo, L. Rossetto, Experimental investigation on condensation heat transfer and pressure drop of new hfc refrigerants (r134a, r125, r32, r410a, r236ea) in a horizontal smooth tube, International Journal of Refrigeration 24 (1) (2001) 73–87.

[74] C. Park, P. Hrnjak, Co2 and r410a flow boiling heat transfer, pressure drop, and flow pattern at low temperatures in a horizontal smooth tube, International Journal of Refrigeration 30 (1) (2007) 166–178.

[75] Z. Liu, R. Winterton, A general correlation for saturated and subcooled flow boiling in tubes and annuli, based on a nucleate pool boiling equation, International journal of heat and mass transfer 34 (11) (1991) 2759–2766.

[76] B. Watel, Review of saturated flow boiling in small passages of compact heat-exchangers, International Journal of Thermal Sciences 42 (2) (2003) 107–140.

[77] M. Cooper, Saturation nucleate pool boilinga simple correlation, in: Inst. Chem. Eng. Symp. Ser, Vol. 86, 1984, pp. 785–793.

[78] K. Stephan, C. V. Green, Heat transfer in condensation and boiling, Springer, 1992.

[79] J. Kaew-On, S. Wongwises, Experimental investigation of evaporation heat transfer coefficient and pressure drop of r-410a in a multiport mini-channel, International Journal of Refrigeration 32 (1) (2009) 124–137.

[80] F. Vakili-Farahani, B. Agostini, J. R. Thome, Experimental study on flow boiling heat transfer of multiport tubes with r245fa and r1234ze (e), International Journal of Refrigeration 36 (2) (2013) 335–352.

[81] R. Yun, J. H. Heo, Y. Kim, Evaporative heat transfer and pressure drop of r410a in microchannels, International journal of refrigeration 29 (1) (2006) 92–100.

[82] W. Li, Z. Wu, Generalized adiabatic pressure drop correlations in evaporative micro/mini-channels, Experimental Thermal and Fluid Science 35 (6) (2011) 866–872.

[83] H. J. Lee, S. Y. Lee, Heat transfer correlation for boiling flows in small rectangular horizontal channels with low aspect ratios, International Journal of Multiphase Flow 27 (12) (2001) 2043–2062.

[84] S. Haaland, Simple and explicit formulas for the friction factor in turbulent pipe flow, Journal of Fluids Engineering 105 (1) (1983) 89–90.

[85] K. Hudon, T. Merrigan, J. Burch, J. Maguire, Low-cost solar water heating research and development roadmap, Contract 303 (2012) 275–3000.

[86] H. Cassard, P. Denholm, S. Ong, Break-even cost for residential solar water heating in the united states: key drivers and sensitivities, Contract 303 (2011) 275–3000.

[87] Solar heating and cooling, slides of a presentation by Solar Energy Industries Association (SEIA), Feb. 6 (2013).

[88] Review of the incentive levels and progress of the California solar initiative-thermal program, Tech. rep., California Public Utilities Commission, Energy Division, Customer Generation Programs, available at http://www.cpuc.ca.gov/NR/rdonlyres/B7D3D1AC-5C9A-49C9-81E1-8E03E471AA73/0/CSIThermalAB2249ReportFinalWebVersionJanuary292014.pdf (January 2014).

[89] E. Murray, US solar thermal market outlook, california Solar Energy Industries Association, Aztec Solar Inc., ELM Distribution and SEIA. Slides presented at the 6th Germany California Solar Day, Sept. 14, 2010. Available at http://www.gaccwest.com/fileadmin/ahk_sanfrancisco/Dokumente/2010-09_Solar_Day_3_Ed_Murray_The_U.S._Solar_Thermal_Market.pdf (2010).

[90] Tax credits, rebates and savings — Department of Energy, from http://energy.gov/savings (2015).

[91] F. Proske, Solar thermal energy technology and market trends, powerpoint slides by A.O. Smith Water Products Co., Meshoppen, PA. Available at http://www.asse-plumbing.org/chapters/NOH_SolarEnergy.pdf (2010).

[92] US solar market insight report: 2011 solar heating and cooling year-in-review, Tech. rep., GTM Research Solar Analysts, and SEIA Policy and Research Division (2012).

[93] Natural gas: Natural gas prices, Tech. rep., U.S. Energy Information Administration, available at http://www.eia.gov/dnav/ng/ng_pri_sum_dcu_nus_a.htm (2015).

[94] I. M. M. . Investments, Commodity and metal prices, important industrial commodities, Tech. rep., InfoMine Inc., data accessed on Feb. 6, 2015 and available at http://www.infomine.com/investment/metal-prices/.

NOMENCLATURE

a	width of one minichannel tube (m)
A	area (m^2)
Bo	boiling number
C_1 to C_5	constants in Kandlikar heat transfer coefficient correlation
Co	convective boiling number
C_p	specific heat of working fluid $(Jkg^{-1}K^{-1})$
D	diameter (m)
E	enhancement factor in Liu and Winterton heat transfer coefficient correlation
f	friction factor
F	enhancement factor in Odeh et al. heat transfer coefficient correlation
F_{fl}	fluid dependent parameter in Kandlikar heat transfer coefficient correlation
Fr	Froude number
g	gravitational constant (ms^{-2})
G	mass flux $(kgm^{-2}s^{-1})$
G_s	total insolation, or solar irradiation (Wm^{-2})
h	convection heat transfer coefficient $(Wm^{-2}K^{-1})$
H	vertical height (m)
i	enthalpy $(kJkg^{-1})$
$I_{thermal}$	thermal inertial of a material $(Jm^{-2}K^{-1}s^{-1/2})$
i_{lv}	latent heat of vaporization (Jkg^{-1})
k	thermal conductivity $(Wm^{-1}K^{-1})$
L	length (m)
m	mass (kg)
$\dot{m}$	mass flow rate (kgs^{-1})
M	molecular weight $(gmol^{-1})$
N	number of tubes
N_f	number of fins in a minichannel tube
Nu	Nusselt number
P	pressure (Pa)
P_w	wetted perimeter (m)
Pr	Prandtl number
q	heat flux (Wm^{-2})
$\dot{Q}$	heat transfer rate (W)
R	thermal resistance (KW^{-1})

Re	Reynolds number
Ra	Rayleigh number
S	suppression factor in Liu and Winterton heat transfer coefficient correlation; correction factor in Odeh et al. correlation; additional factor in Kaew-On and Wongwises correlation
t	thickness (m)
T	temperature (K)
U_L	overall heat transfer coefficient at the absorber surface
v	velocity (ms^{-1})
v_{air}	velocity of the ambient air surrounding the collector (ms^{-1})
W	width (m)
W_t	tube spacing (m)
x	vapor quality
X	Lockhart-Martinelli two-phase parameter

Greek Letters

α	absorption coefficient; or void fraction
β	title angle; aspect ratio
ϵ	emissivity
η	efficiency
μ	dynamic viscosity
Φ	two-phase multiplier
Ψ	Shah dimensionless heat transfer coefficient parameter
ρ	reflectivity; or density (kgm^{-3})
σ	Stefan-Boltzmann constant $(Wm^{-2}K^{-4})$; or surface tension (Nm^{-1})
τ	transmissivity
θ	angle (deg)

Subscripts and superscripts

abs	absorber
$absorbed$	incident radiation with effect of glass transmissivity
air	air between the glass cover and absorber
Al	aluminum
bs	boiling suppression
cb	convective boiling
$cond$	conductive heat transfer
$conv$	convective heat transfer
cr	critical
Cu	copper
e	external
fin	fin of the minichannel tube

$fluid$	working fluid
fp	flat-plate collector
Fr	Froude number
$free$	free-flow
$frict$	frictional
g	glass cover
h	hydraulic
i	internal
in	inlet
l	liquid
lo	liquid-only
$major$	major, or the width of a minichannel tube
mc	minichannel tubes collector
$mean$	mean average
$minor$	minor, or the height of a minichannel tube
mom	momentum
nb	nucleate boiling
o	overall
out	outlet
rad	radiative heat transfer
red	reduced
sky	sky
$static$	static
tp	two-phase
tt	turbulent-turbulent
tv	turbulent-viscous
$tube$	minichannel tube
v	vapor
vo	vapor-only
vt	viscous-turbulent
vv	viscous-viscous
$wall$	wall of the minichannel tube
web	web of the minichannel tube
$wind$	wind; ambient air
∞	ambient

Appendix A

COPPER MINICHANNEL TUBE MANUFACTURING

The following information about the manufacturing process of the copper minichannel was shared by Dr. Frank F. Kraft of Ohio University. All photos were provided and credited to Dr. Kraft.

The primary components that were needed for extrusion were the following: container, ram-stems, dummy blocks, and extrusion dies. Figures A.1 and A.2 shows the components. The extrusion dies were fabricated from ATI 720, Inconel 720 and Rene 41 nickel-based alloys and superalloys that can withstand high temperatures from the extrusion.

Figure A.1: Extrusion die.

The extrusion components are assembled on a servo-hydraulic machine, model 810 MTS®. This machine is capable of producing up to 250 kN of ram force. Prior to extrusion, cartridge heaters are inserted into the container while the entire apparatus is insulated with a zirconia "blanket". Zirconia is a type of ceramic also known as zirconium dioxide, a white crystalline oxide of zirconium. Figures A.3 and A.4 are photos of the servo-hydraulic 810 MTS®.

The extrusion billets were made and machined from OFHC 101-Cu copper rods to fit the container. In order to fulfill the design requirements and constraints, the container bore dimensions are critical due to several factors: 1. width of the tube, 2. buckling criteria of the ram-stems, 3. ram pressure required for extrusion, 4. the force limitations of the MTS® machine, and 5. the billet volume required to

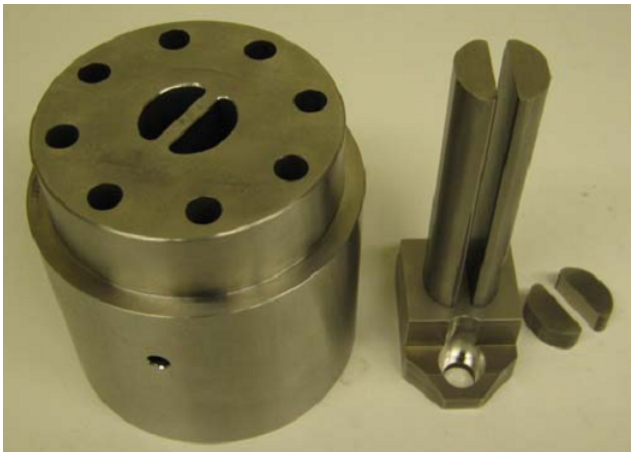

Figure A.2: Form left to right: container, ram-stems and dummy-blocks.

Figure A.3: The components assembled together on the MTS® machine.

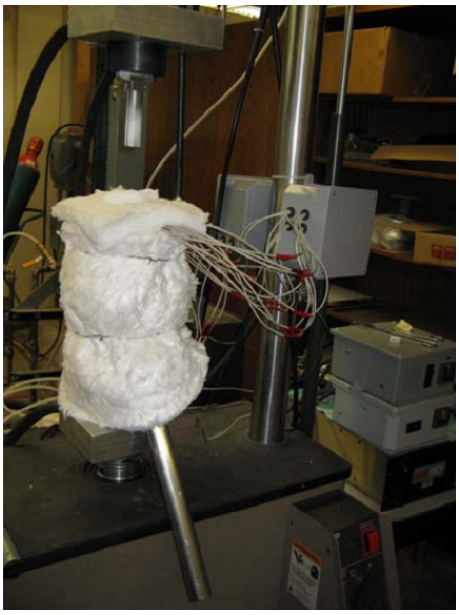

Figure A.4: The assembled components wrapped with zirconia insulation.

manufacture the desired tube length plus the discard lengths at the beginning and end of extrusion. For the copper minichannel solar collector, 1819 mm in length was required for each tube and 42 copper extrusion billets were used for to make 20 copper minichannel tubes. Figures A.5 and A.6 shows the copper billets and the copper billets placed in the container, respectively.

Figure A.5: Copper billets.

Figure A.6: Copper billets machined to fit into the contaner.

As the copper billets are heated to the required temperature for extrusion in the apparatus, the MTS® machine provides the ram-stems with a force of up to 250 kN to push the copper billets through the extrusion die. The minichannel tube exits the heated extrusion apparatus through a nitrogen gas tube that is attached to the lower part of the apparatus as seen in Figures A.7 and A.8.

After the extrusion of the copper minichannel tubes, the tubes were straightened and the ends were cut and discarded to the desired length. Figures A.9, A.10 and A.11 shows the finished product measured, straightened and packaged.

At the end of the extrusion of each tube, the apparatus is allowed to cool to room temperature before it was disassembled. The remaining copper that in the die is removed using an Instron® test machine by pulling it from the die. A special custom fixture was constructed for this purpose. Lastly, the residual copper left in the container and die was dissolved in nitric acid under a fume hood. Photos of the

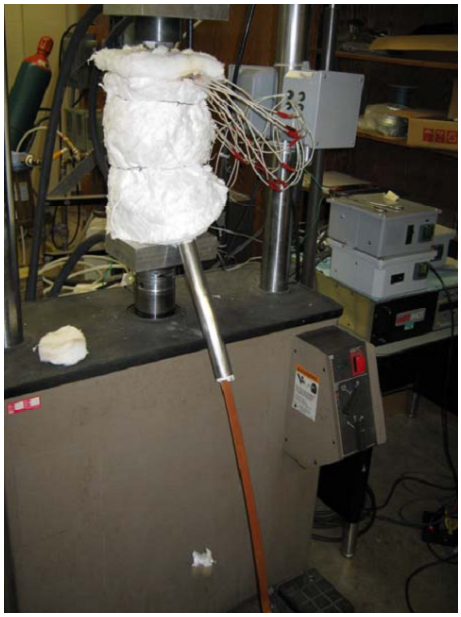

Figure A.7: Extruded copper minichannel tube exiting through a nitrogen gas tube.

Figure A.8: The nitrogen gas tube attached to the apparatus.

Figure A.9: Copper minichannel tubes after extrusion.

Figure A.10: Copper minichannel tubes straightened.

Figure A.11: Tubes packed with aluminum angle supports for shipment.

container and die after extrusion, and the process of removing the residual copper with the Instron® machine is shown in figures A.12 and A.13.

Figure A.12: Residual copper in the container and die.

Figure A.13: The Instron® machine removing the residual copper from the container.

Appendix B

ADDITIONAL FRICTIONAL PRESSURE DROP VALIDATION ANALYSIS

Additional cases of frictional pressure drop correlations in comparison with experimental data from literature are analyzed and presented in Figures B.1 to B.7. Experimental data are taken from Jassim and Newell [59] and Yang and Webb [61]. Cases operate with two different minichannel tube configurations, a range of mass fluxes from 100 to 1000 kg/m^2s, R134a, R410a and R12 as working fluids at various saturation temperatures, and varying inlet vapor qualities. Seven cases are analyzed, and the specific cases are described as, in respect to the following figures: for a six-port minichannel tube with hydraulic diameter of $D_h = 1.54\ mm$ and saturation temperature of $T_{sat} = 10\ ^\circ C$ operating at (1) a mass flux of $G = 100\ kg/m^2s$ using R134a as the working fluid, (2) $G = 200\ kg/m^2s$ using R134a, (3) $G = 100\ kg/m^2s$ using R410a, and (4) $G = 200\ kg/m^2s$ using R410a; for a 4-port minichannel tube with a hydraulic diameter of $D_h = 2.64\ mm$ and saturation temperature of $T_{sat} = 65\ kg/m^2s$ operating at a (5) $G = 400\ kg/m^2s$ using R12, (6) $G = 600\ kg/m^2s$ using R12, and (7) $G = 1000\ kg/m^2s$ using R12.

Jassim and Newell provided frictional pressure drop data from two-phase flow in a 6-port minichannel tube of hydraulic diameter of 1.54 mm using R134a and R410a as working fluids at a saturation temperature of 10 $^\circ C$ and varying inlet vapor qualities. Figure B.1 shows predictions of the four frictional pressure drop correlations (Chisholm (1967) [53], Muller-Steinhagen and Heck (1986) [1], Mishima and Hibiki (1996) [57], Sun and Mishima (2009) [58]) compared to experimental values with a mass flux of G = 100 kg/m^2s and R134a as the working fluid. It is seen that Mishima and Hibiki and Sun and Mishima correlations did not predict the test data well with a majority of their predictions under -30% of the experimental values with Chisholm falling right behind. Muller-Steinhagen and Heck gives better predictions. Mean absolute errors are calculated and presented in Table 4.3 in Chapter 4. In Figure B.1, the mean absolute error for Chisholm, Muller-Steinhagen and Heck, Mishima and Hibiki, and Sun Mishima, respectively, are 73.5%, 24.3%, 98.7% and 99.7%.

It is noted that the frictional pressure drop predictions and mean absolute errors for Mishima and Hibiki and Sun and Mishima are simulated up to certain vapor qualities. These two correlations are not accurate predicting frictional pressure

drop at higher vapor qualities and show increasing deviations. For instance, in Figure B.1, Mishima and Hibiki and Sun and Mishima correlations were simulated up to a vapor quality of approximately x $\approx$ 0.50. Beyond x = 0.50, the predictions from the two correlations are extremely inaccurate.

Figure B.2 has a similar outcome with the predictions of frictional pressure drop correlations compared to the previous case. The operating conditions are similar except the mass flux is raised to $G = 200\ kg/m^2s$. Mishima and Hibiki and Sun and Mishima correlations made better predictions at lower fricitonal pressure drops. Majority of prediction from Chisholm are under -30%. Muller-Steinhagen and Heck gives the best prediction out of the four correlations. The mean absolute errors calculated are 46.9%, 48.4%, 92.9%, and 14.9%, respectively. Predictions and mean absolute errors calculated for Mishima and Hibiki and Sun and Mishima simulated up to a vapor quality of x $\approx$ 0.63 due to the increased inaccuracy as vapor quality increases.

Figure B.3 shows experimental versus predicted values of frictional pressure drop in the same tube configuration except with R410a as the working fluid operating at a mass flux of $G = 100\ kg/m^2s$. Mishima and Hibiki, Sun and Mishima, and Chisholm shows similar prediction patterns as Figure B.1 with the same mass flux. Muller-Steinhagen and Heck provides the best predictions out of the four. The mean absolute errors of the correlations are 127.5%, 92.0%, 117.2%, and 42.8%, respectively. Again, Mishima and Hibiki and Sun and Mishima correlations are unable to predict at higher qualities. In this case, the two correlations are only simulated up to a vapor quality of x $\approx$ 0.57.

Lastly, from Jassim and Newell experimental data, Figure B.4 shows predicted frictional pressure drops with experimental values at a mass flux of $G = 200\ kg/m^2s$ using R410a as the working fluid. While the majority of Chisholm correlation under-predicted the frictional pressure drops, Mishima and Hibiki and Sun and Mishima correlations made better predictions in comparison to the last three cases. However, Mishima and Hibiki and Sun and Mishima correlations only simulated up to a vapor quality of x $\approx$ 0.80 before increasing inaccuracies. Again, Muller-Steinhagen and Heck seem to provide the best results out of the four. The mean absolute errors are 79.8%, 37.9%, 34.7%, and 16.3%, respectively.

From running these five cases and comparing with experimental data from Jassim and Newell, a couple observations can be made. The correlations have more difficulty in predicting frictional pressure drops at lower mass flux, seen from the increased mean absolute errors. Mishima and Hibiki and Sun and Mishima correlations have a significant lower mean absolute errors as the mass flux increased. Muller-Steinhagen also shows slightly better mean absolute errors with higher mass fluxes.

Yang and Webb measured experimental frictional pressure drops in a 4-port minichannel tube with a hydraulic diameter of 2.64 mm using R12 as the working

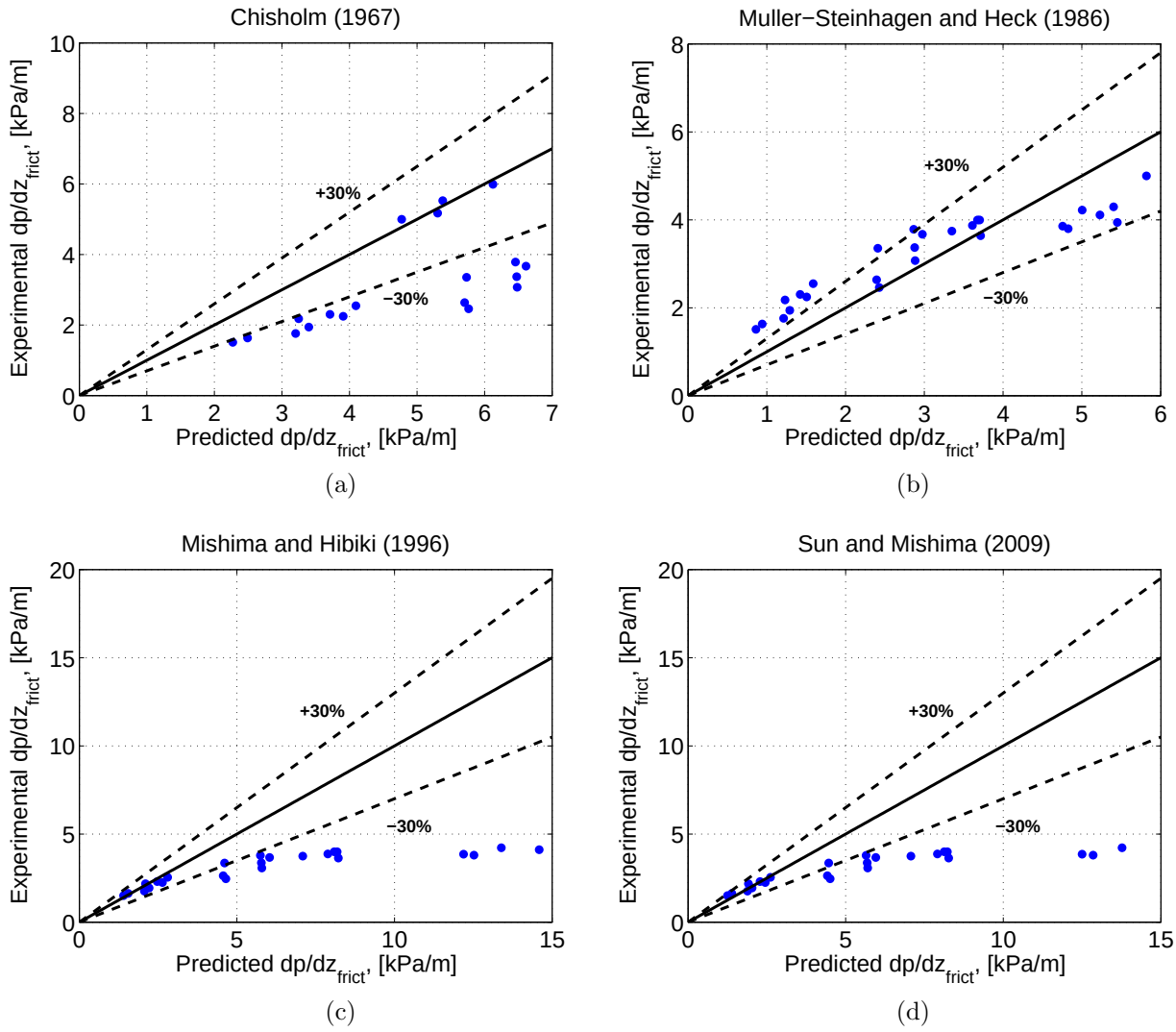

Figure B.1: Experimental versus predicted values of frictional pressure drop using (a) Chisholm (1967), (b) Muller-Steinhagen and Heck (1986), (c) Mishima and Hibiki (1996), and (c) Sun and Mishima frictional pressure drop correlations in a D_h = 1.54 mm 6-port minichannel tube at a mass flux of $G = 100\ kg/m^2s$ with R134a as the working fluid [59, 60].

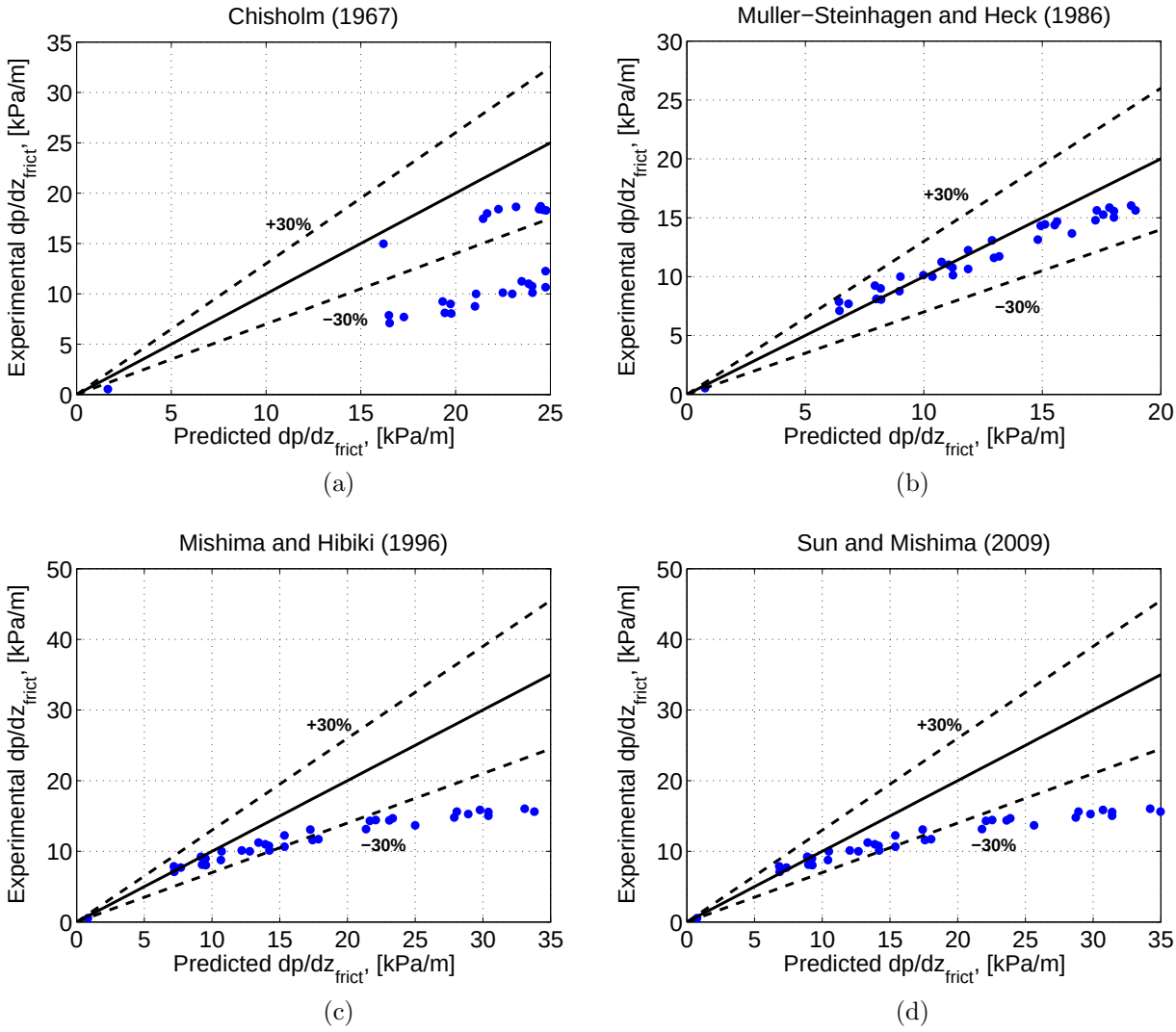

Figure B.2: Experimental versus predicted values of frictional pressure drop using (a) Chisholm (1967), (b) Muller-Steinhagen and Heck (1986), (c) Mishima and Hibiki (1996), and (c) Sun and Mishima frictional pressure drop correlations in a D_h = 1.54 mm 6-port minichannel tube at a mass flux of $G = 200\ kg/m^2s$ with R134a as the working fluid [59, 60].

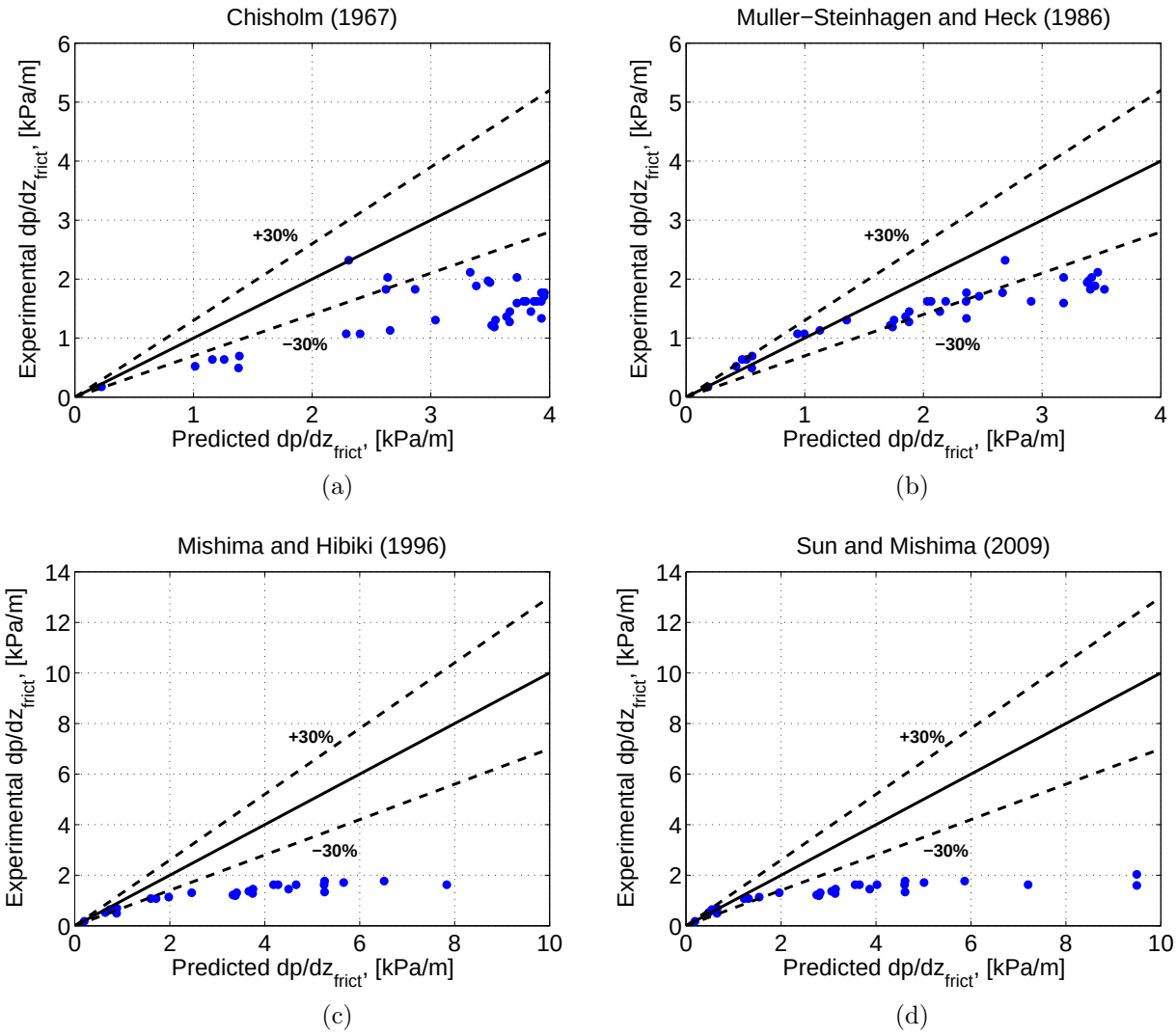

Figure B.3: Experimental versus predicted values of frictional pressure drop using (a) Chisholm (1967), (b) Muller-Steinhagen and Heck (1986), (c) Mishima and Hibiki (1996), and (c) Sun and Mishima frictional pressure drop correlations in a D_h = 1.54 mm 6-port minichannel tube at a mass flux of $G = 100\ kg/m^2s$ with R410a as the working fluid [59, 60].

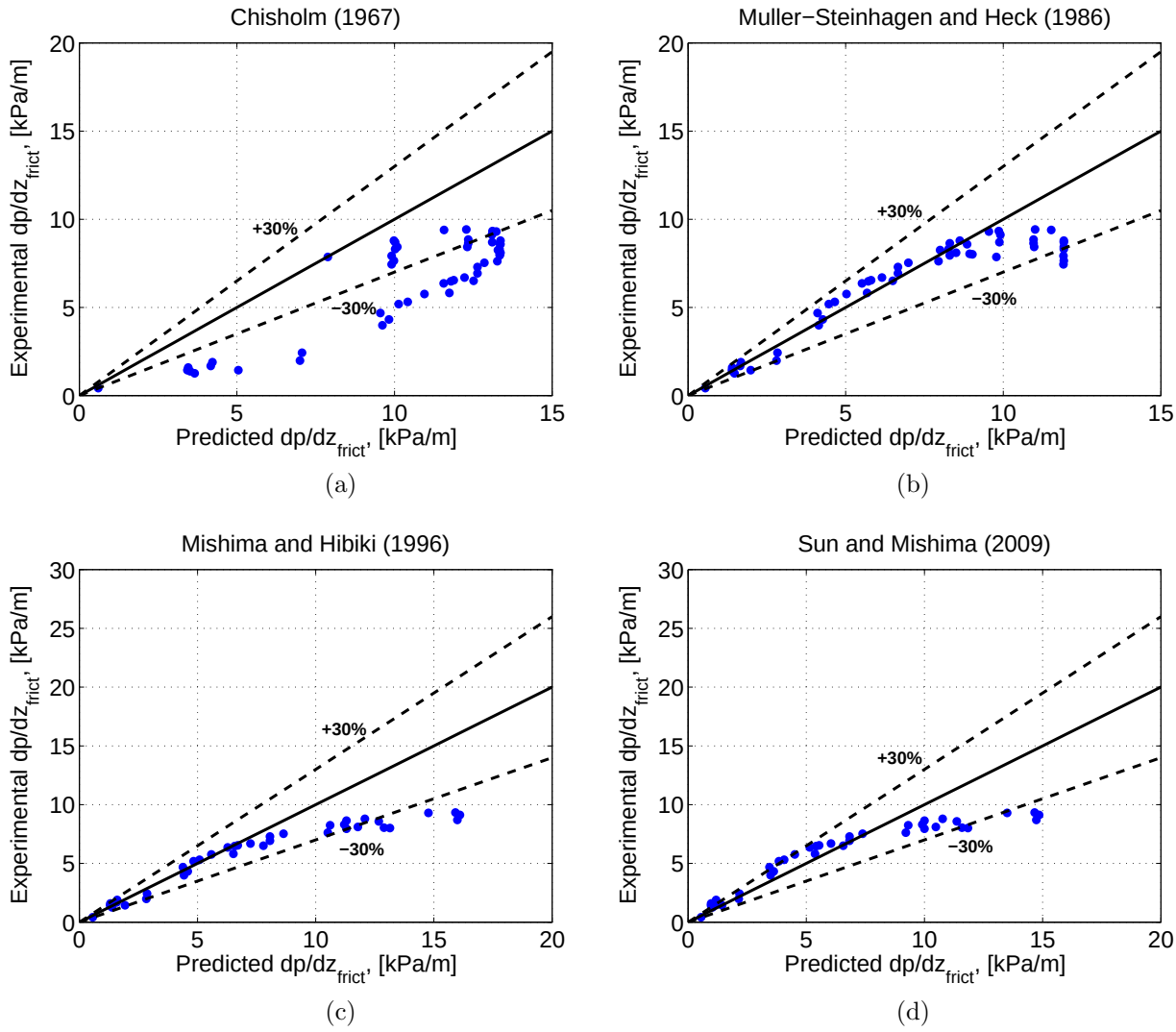

Figure B.4: Experimental versus predicted values of frictional pressure drop using (a) Chisholm (1967), (b) Muller-Steinhagen and Heck (1986), (c) Mishima and Hibiki (1996), and (c) Sun and Mishima frictional pressure drop correlations in a D_h = 1.54 mm 6-port minichannel tube at a mass flux of $G = 200\ kg/m^2s$ with R410a as the working fluid [59, 60].

fluid at a saturation temperature of 65 $^{\circ}C$. The cases analyzed operates at a range of mass fluxes from 400 to 1000 kg/m^2s and varying inlet vapor qualities. From Figures B.5 to B.7, the three figures shows cases of mass fluxes of 400, 600 and 1000 kg/m^2s, respectively. There are less experimental data than Jassim and Newell, however, it can be seen that predictions by Chisholm, Mishima and Hibiki, and Sun and Mishima are better as higher mass fluxes are tested. The mean absolute errors calculated for Chisholm, Muller-Steinhagen, Mishima and Hibiki, and Sun and Mishima, respectively, for Figure B.5 that operated at a mass flux of 400 kg/m^2s are 46.9%, 11.0%, 92.2%, and 25.0%. For Figure B.6 operating at mass flux of 600 kg/m^2s, the mean absolute errors, respectively, 37.1%, 15.0%, 73.0% and 14.0%. Finally, for Figure B.7 operating at a mass flux of 1000 kg/m^2s, the mean absolute errors are 19.3%, 21.8%, 61.8%, and 12.3%, respectively. All correlations except Muller-Steinhagen and Heck, made better predictions as mass flux increased. From all the frictional pressure drop validation analyses, Muller-Steinhagen and Heck provides better results in most cases out of the four correlations, and therefore, Muller-Steinhagen and Heck correlation is used to predict frictional pressure drop in the minichannel solar collector during steam generation.

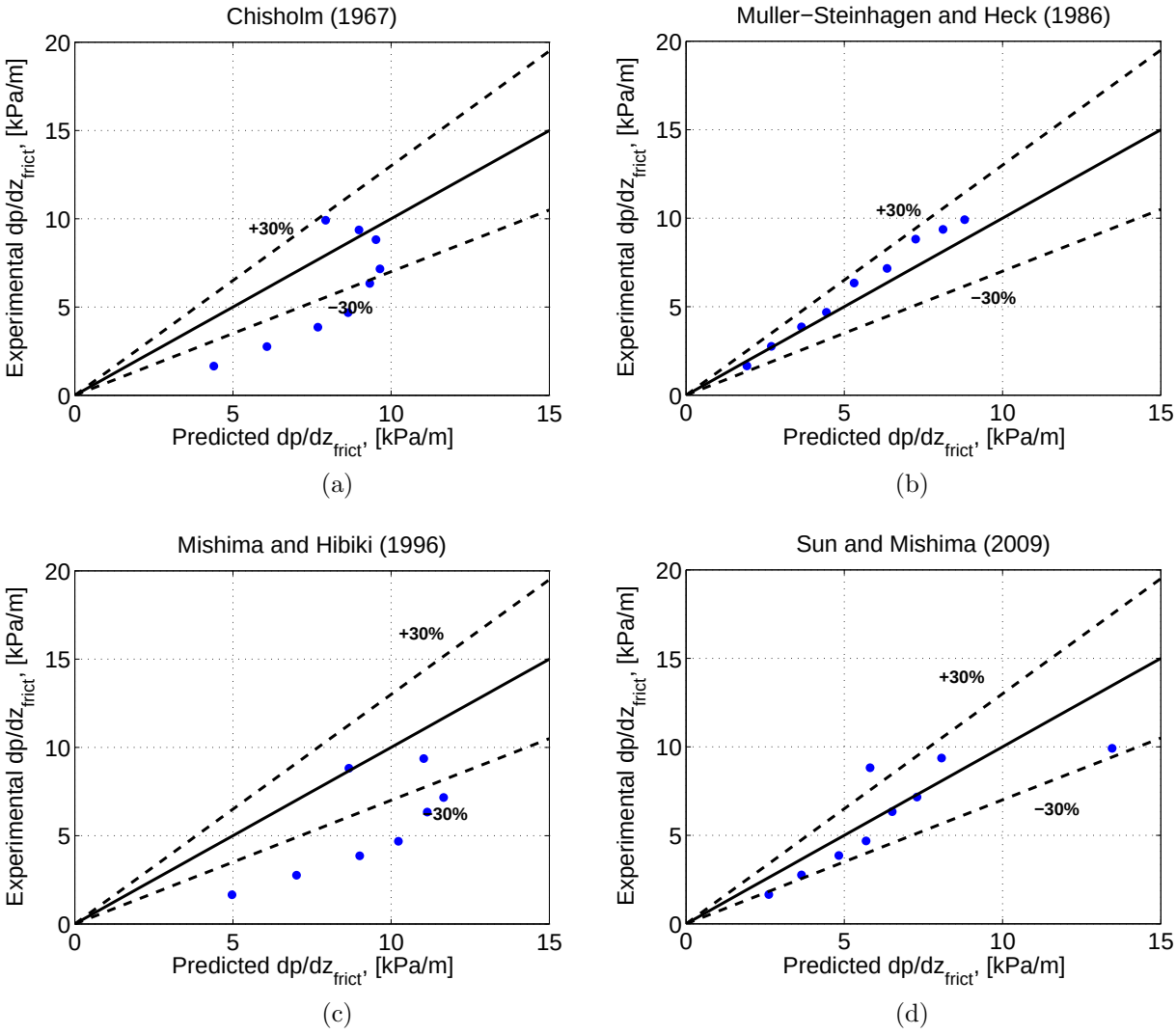

Figure B.5: Experimental versus predicted values of frictional pressure drop using (a) Chisholm (1967), (b) Muller-Steinhagen and Heck (1986), (c) Mishima and Hibiki (1996), and (c) Sun and Mishima frictional pressure drop correlations in a D_h = 2.64 mm 4-port minichannel tube at a mass flux of $G = 400\ kg/m^2s$ with R12 as the working fluid [61].

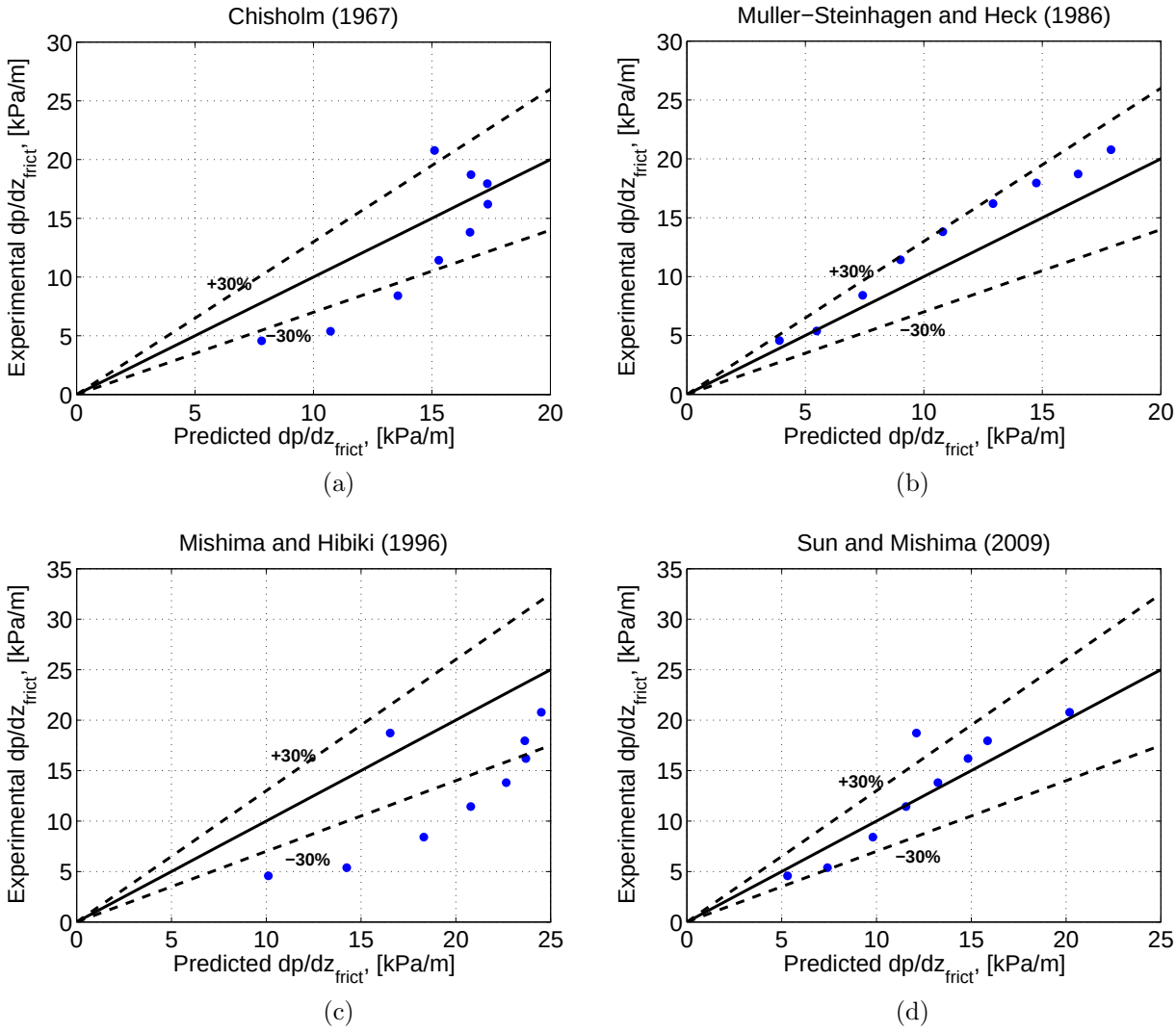

Figure B.6: Experimental versus predicted values of frictional pressure drop using (a) Chisholm (1967), (b) Muller-Steinhagen and Heck (1986), (c) Mishima and Hibiki (1996), and (c) Sun and Mishima frictional pressure drop correlations in a D_h = 2.64 mm 4-port minichannel tube at a mass flux of $G = 600\ kg/m^2s$ with R12 as the working fluid [61].

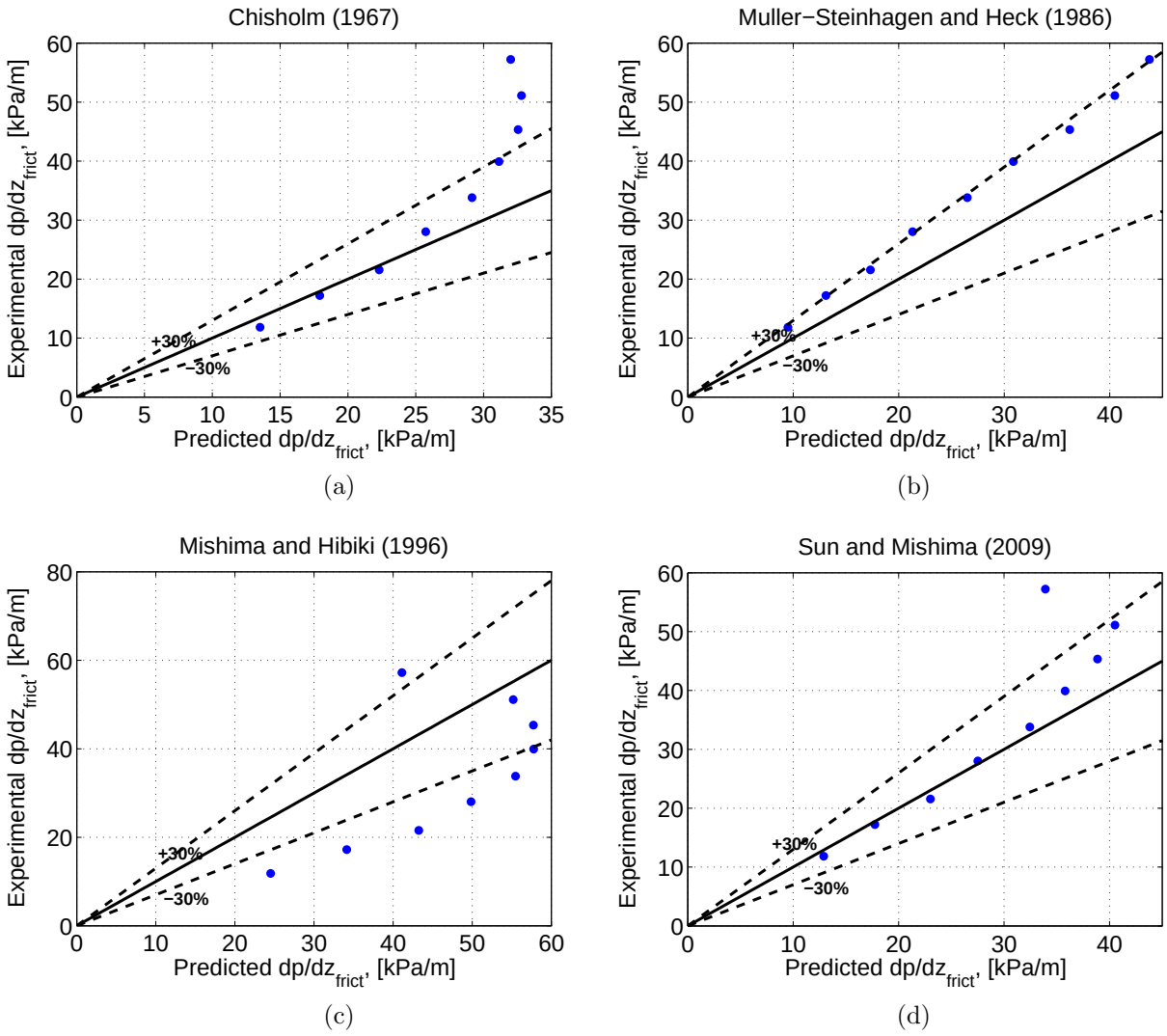

Figure B.7: Experimental versus predicted values of frictional pressure drop using (a) Chisholm (1967), (b) Muller-Steinhagen and Heck (1986), (c) Mishima and Hibiki (1996), and (c) Sun and Mishima frictional pressure drop correlations in a D_h = 2.64 mm 4-port minichannel tube at a mass flux of $G = 1000\ kg/m^2s$ with R12 as the working fluid [61].

Appendix C

ADDITIONAL HEAT TRANSFER COEFFICIENT VALIDATION ANALYSIS

Two additional cases are analyzed comparing predicted two-phase heat transfer coefficients with experimental values obtained from Park and Hrnjak [74] and Kaew-On and Wongwises [79]. Kandlikar (1990) [65], Shah (1982) [63], Liu and Wintertoon (1981) [75], Odeh et al. (1998) [2] and Kaew-On and Wongwises (2009) [79] correlations are applied to predict the heat transfer coefficients.

Figure C.1 shows predicted versus experimental two-phase heat transfer coefficient values in a circular copper tube of diameter $D = 6.1\ mm$ with R410a at a saturation temperature of -15 $^{\circ}C$ as the working fluid extracted from Park and Hrnjak [74]. The working fluid is flowing at a mass flux of $G = 200\ kg/m^2s$ at various inlet vapor qualities, and a constant heat flux of $q = 2000\ W/m^2$ is uniformly applied to the circular tube. Since the tube configuration is circular, Kaew-On and Wongwises heat transfer coefficient correlation is not applicable in this case. It can be seen from Figure C.1 that all the data are within ±30% except one prediction from Shah correlation. The mean absolute error is reported in Table 4.6 from Chapter 4. The mean absolute errors for Kandlikar, Shah, Liu and Winterton, and Odeh et al. for this case are, respectively, 9.2%, 16.0%, 5.3%, and 8.8%.

Figure C.2 shows predicted heat transfer coefficient values from the five correlations in comparison to experimental data extracted from Kaew-On and Wongwises [79]. In this case, R410a as the working fluid is flowing in a 3-port aluminum minichannel tube with a hydraulic diameter of $D_h = 3.48\ mm$ and saturation temperature of 10 $^{\circ}C$. The working fluid flows with a mass flux of $G = 300\ kg/m^2s$ and inlet vapor quality is $x = 0.1$. The minichannel tube is applied with a range of heat fluxes from approximately 1.5 to 12 kW/m^2. From Figure C.2, Kandlikar, Shah, Liu and Winterton, and Odeh et al. tends to over-predict, whereas, Kaew-On and Wongwises correlation under-predicts the heat transfer coefficients. The mean absolute error calculated are given as, respectively, 31.2%, 46.6%, 32.2%, 25.4%, and 50.4%.

Examining the two cases in addition to those presented in Chapter 4, an observations can be made. It is possible that due to the minichannel tube configuration, heat transfer coefficient predictions are not as good as those predicted in circular tubes. While studying two-phase flow and heat transfer, it is noticed that

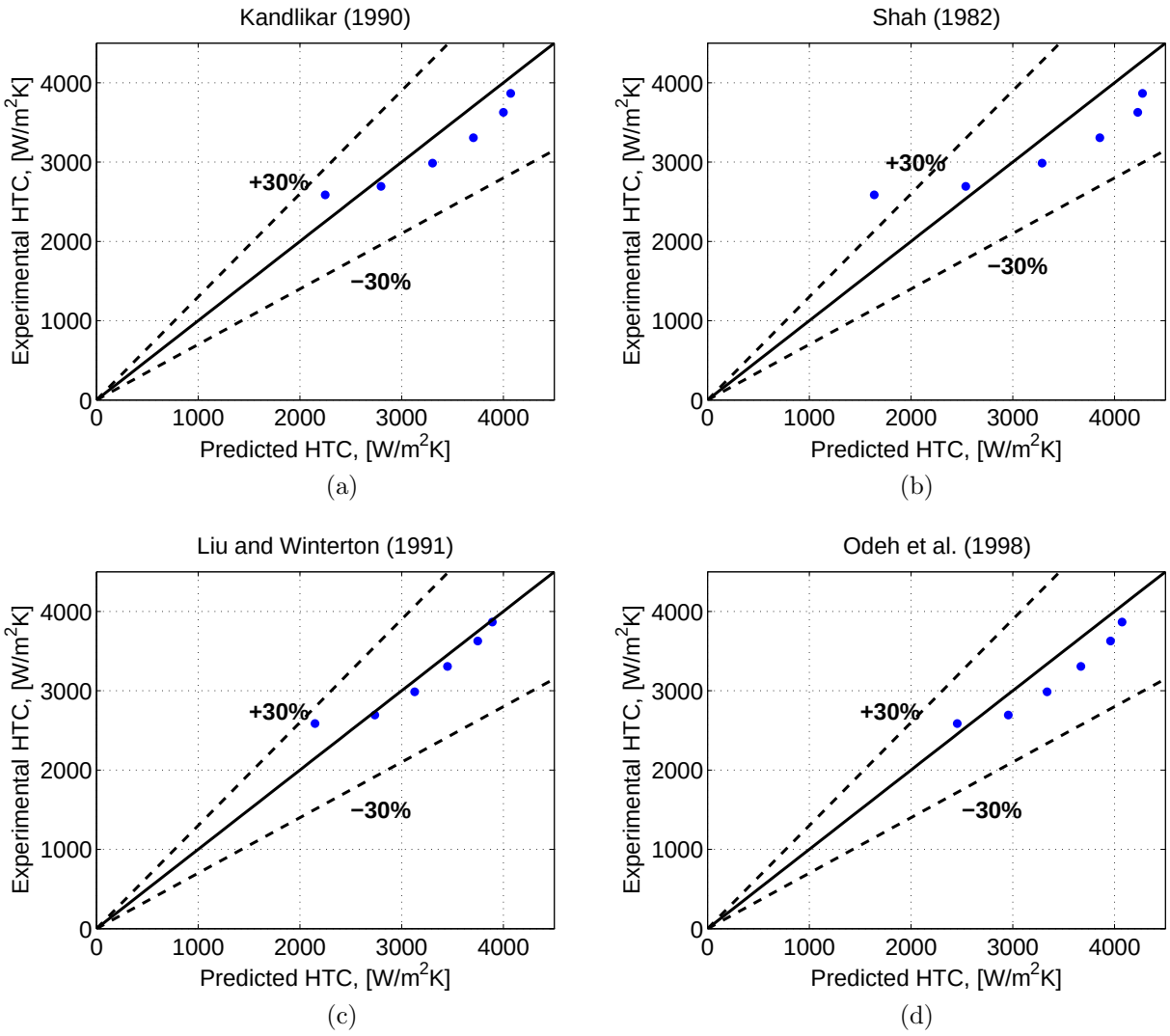

Figure C.1: Predicted versus experimental two-phase heat transfer coefficient in copper circular tube of $D = 6.1\ mm$, R410a refrigeration working fluid, saturation temperature of -15 $°C$, constant heat flux of $q = 2000\ W/m^2$, and at a mass flux $G = 200\ kg/m^2s$ [74]. Correlations used: (a) Kandlikar (1990), (b) Shah (1982), (c) Liu and Winterton (1991), and (d) Odeh et al. (1998).

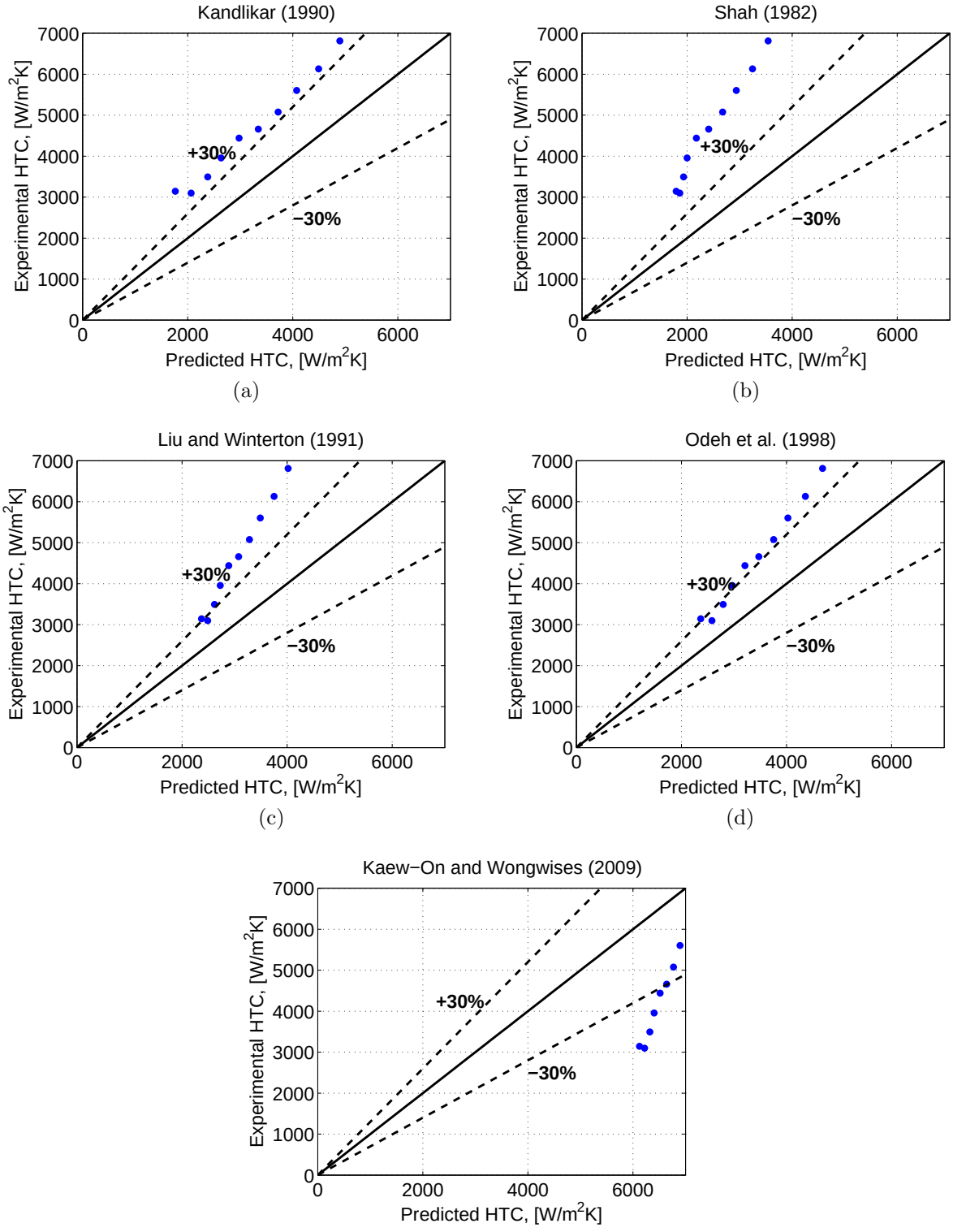

Figure C.2: Predicted versus experimental two-phase heat transfer coefficient in an aluminum minichannel tube of $D_h = 3.48\ mm$, R410a refrigeration working fluid, saturation temperature of 10 $°C$, and at a mass flux $G = 300\ kg/m^2s$ [79]. Correlations used: (a) Kandlikar (1990), (b) Shah (1982), (c) Liu and Winterton (1991), (d) Odeh et al. (1998), and (e) Kaew-On and Wongwises (2009).

there is a lack of studies of two-phase flow and heat transfer coefficient predictions in minichannel tubes. More research is required in order to develop a correlation that makes good agreement with heat transfer coefficient predictions in minichannel tubes, as well as, a correlation that is universal to any tube configuration and working fluid type. However, for the time being and from the validation analyses, the heat transfer coefficient by Odeh et al. provides the best predictions out of the other correlations, and therefore, Odeh and al. correlation is used to predict the heat transfer coefficient in the minichannel solar collector during steam generation.